Macrosegregation in Solidification of A356

by

Hatef Khadivinassab

M.Eng., University of Birmingham, 2012

A THESIS SUBMITTED IN PARTIAL FULFILLMENT
OF THE REQUIREMENTS FOR THE DEGREE OF

Doctor of Philosophy

in

THE FACULTY OF GRADUATE AND POSTDOCTORAL STUDIES

(Materials Engineering)

The University Of British Columbia
(Vancouver)

April 2018

Abstract

A combined experimental / numerical approach has been applied to investigate the bulk transfer of solute due to liquid metal feeding during shape casting of aluminum alloy A356 (Al-7Si-0.3Mg). A series of dumbbell-shaped experimental casting geometries have been developed, which promote solute redistribution due to liquid metal feeding. Three of the castings were produced in small moulds with natural cooling, forced cooling and insulated conditions and one casting was made in a large mould with natural cooling. The redistribution of solute in the castings has been evaluated using a novel image processing technique based on the area fraction of silicon. The results show that the casting with the forced cooling configuration exhibited a larger degree of macrosegregation.

In the numerical model, silicon segregation during solidification is calculated assuming the Scheil approximation, and is coupled with a macro-scale transport model that considers resistance in the mushy zone and feeding flow. The model has been implemented within the commercial CFD software, FLUENT, which simultaneously solves the thermal, fluid flow fields and species segregation on the macro-scale. The results from the simulation agree with the experimental results, except for the cases where significant liquid encapsulation occurs. The model predicts high levels of enrichment when liquid encapsulation is present in the joint section of the dumbbell-shaped castings.

Finally, a constitutive behaviour relationship was developed based on the Ludwik-Hollomon equation to predict the flow stress of Al-Si-Mg alloys with varying silicon composition and Dendrite Arm Spacing (DAS) in the as-cast (AC) or T6 condition with high accuracy. This model was then used with the results of the segregation model to predict yield strength distribution in the aforementioned dumbbell-shaped casting. The results show that silicon segregation has a more significant effect on the

yield strength than DAS.

Lay Summary

One of the on-going challenges in the automotive industry is to control defects so as to improve product quality and reduce production cost. Macrosegregation related defects can lead to casting rejection in the automotive industry because they are detrimental to mechanical performance, due to the variation of mechanical properties throughout the casting. The particular emphasis of this research is to develop a methodology to quantitatively describe macrosegregation during solidification of shape castings of A356 aluminum alloy and to characterize the effects of macrosegregation on mechanical properties. Ultimately, through this research, the ability to predict macrosegragation and its effect on mechanical properties results in an improved ability to predict final performance of a casting.

Preface

The following journal submissions have been extracted from the body of work presented in this dissertation. My supervisor, Prof. Daan Maijer provided experimental insight, results interpretation and editorial support covering all aspects of my research. Aside from my supervisor, and key secondary contributors, I am the primary contributor to these works:

1) *Khadivinassab H.*, Maijer D. M., Cockcroft S. L., "Constitutive Behviour of Macrosegregated A356", (2017) – under revision

2) *Khadivinassab H.*, Maijer D. M., Cockcroft S. L.,"Characterization of Macrosegregation in Eutectic Alloys", Materials Charcterization, (2017)

3) *Khadivinassab H.*, Fan P., Reilly C., Yao L., Maijer D. M., Cockcroft S. L., Phillion A. B.,"Study of the macro-scale solute redistribution due to liquid metal feeding during the solidification of A356", Light Metals Production, Processing and Applications Symposium, The 53rd Annual Conference of Metallurgists, (2014)

Prof. Steve Cockcroft provided experimental insight, editorial support and in interpretation of results for items 1, 2 and 3. Dr. Phillion provided editorial support and in interpretation of the results for item 3.

Chapter 2 contains material from item 1. Chapter 3 is based on the material drawn from item 2. Chapter 4 contains material presented in items 2 and 3. Chapter 5 contains material from item 3. These chapters contain footnotes mirroring the above information.

Table of Contents

List of Tables

List of Figures

Nomenclature

Roman Symbols *(page introduced)*		**Units**
ΔH	Incremental enthalpy per unit mass *(page 92)*	J/kg
$\mathbf{g}$	Gravitational acceleration *(page 92)*	m/s^2
$\mathbf{K}$	Permeability tensor *(page 93)*	m^2
$\mathbf{u}$	Superficial velocity *(page 91)*	m/s
C	Concentration of solute *(page 94)*	%wt
C_0	Initial composition *(page 46)*	%wt or %at
C_e	Eutectic composition *(page 46)*	%wt or %at
C_p	Specific heat *(page 101)*	$J/kg \cdot K$
D	Diffusion coefficient *(page 94)*	m^2/s
H	Phase enthalpy per unit mass *(page 92)*	J/kg
h	Sensible Enthalpy per unit mass *(page 91)*	J/kg
k	Thermal conductivity *(page 91)*	$W/m \cdot K$
L_f	Latent heat fusion *(page 101)*	J/kg
M_i	Atomic mass *(page 46)*	u
P	Pressure *(page 92)*	Pa
Pr	Prandtl number *(page 98)*	
Ra	Rayleigh number *(page 98)*	
Re	Reynolds number *(page 99)*	
T	Temperature *(page 91)*	K
T6	Binary T6 condition *(page 34)*	

Greek Symbols *(page introduced)*	**Units**

β	Liquid fraction *(page 93)*	
ϵ	True strain *(page 21)*	
κ	Partition coefficient *(page 94)*	
μ	Viscosity *(page 92)*	$Pa \cdot s$
ρ	Density *(page 91)*	kg/m^3
σ	Stefan-Boltzmann constant *(page 99)*	$W/(m^2 \cdot K^4)$
σ_H	Ludwik-Hollomon predicted flow stress *(page 21)*	MPa
σ_y	Yield strength *(page 19)*	MPa
ε	emissivity *(page 99)*	–
φ	Area fraction *(page 47)*	
φ_e	Eutectic area fraction *(page 46)*	

Glossary

AAS	Atomic Absorption Spectroscopy
AC	as-cast
AMD	Average Maximum Difference
CAFE	Cellular Automata-Finite Element
CFD	Computational Fluid Dynamics
CLAHE	Contrast Limited Adaptive Histogram Equalization
DAS	Dendrite Arm Spacing
DAQ	Data Acquisition system
EDM	Electro-Discharge Machining
EDX	Energy-Dispersive X-ray Spectroscopy
GMM	Gaussian Mixture Models
HTC	Heat Transfer Coefficient
IHTC	Interfacial Heat Transfer Coefficient
SEM	Scanning Electron Microscopy
XMT	X-ray Micro-Tomography
XRF	X-ray Fluorescence

Acknowledgments

First, I would like to thank my supervisor Prof. Daan Maijer for his support and guidance throughout the course of this work. I would like to thank Jacob Kabel for his valuable help on imaging and sample preparation. I would also like to thank Prof. Steve Cockcroft for his valuable comments and fruitful discussions. A big thank you to Dr. Carl Reilly for his assistance on experimental work and data acquisition. Especial thanks to all colleagues and officemates for providing a friendly environment that I was always pleased to work in. Finally, a big thank you to my friends, family and partner, who have put up with me throughout this.

“Should I kill myself, or have a cup of coffee?"
—Albert Camus.

Dedicated to the dearest reader.

Chapter 1

Introduction

Applications for light metal usage in the automotive and transportation sectors continue to expand to enable improved fuel efficiency and performance. Cast aluminium components, such as cylinder heads, engine blocks and wheels, have shown good market penetration by replacing iron based products due to weight saving and improved aesthetics. Despite the advantages of using light metal alloys such as A356 in the automotive industry, continuous improvement is needed in the manufacturing processes to meet increasing product quality standards and to reduce manufacturing rejection rates [1]. The main cause for rejecting these types of components is casting defects. Throughout the years, numerous remedial actions have been developed to minimize the formation of these defects utilizing trial and error methods [2]. However, often these actions lack the necessary understanding of how and why defects form and only target the elimination of such flaws.

There are six types of casting related defects observed in light metal castings: shrinkage defects, gas-related defects, filling-related defects, undesired phases, distortion and metal/die interaction defects [3]. Controlling and fully eliminating casting defects is not an easy task as each of the aforementioned categories might have overlaps. For instance, in industry, macroporosity, which is mainly a feeding related defect, is typically controlled by adjusting the heat transfer to ensure directional solidification. However, this may result in macrosegregation defects, which has recently been reported in automotive wheel castings [4]. This suggests that there is a link between the parameters producing such defects and understanding how each defect

is formed is a necessity to be able to control/reduce the defects overall.

Shrinkage induced defects can be divided into three main types; macrosegregation, macroporosity and surface depressions. These defects are related to feeding, where feeding refers to the flow of liquid metal within the developing structure of a casting. The extent of solidification, thermo-physical properties of the metal, and pressure and temperature history in the casting are factors that influence the formation of these defects. Similar to other defects, these defects have adverse effects on the mechanical performance of the cast parts [5]. The characteristics of these shrinkage-related defects are as follows:

- **Macroporosity** (Figure 1.1a) defects form when there is inadequate feeding of the liquid metal to compensate for the volumetric shrinkage that occurs during solidification [6]. The pores form when gas (dissolved or metal vapour) is evolved at locations within the casting in regions where liquid metal becomes isolated or encapsulated. To be considered a macro-pore, the voids that form should be greater than 0.3mm in diameter [4]. Macroporosity can negatively impact casting quality in various ways such as reduced fatigue life and poor aesthetics if the pore is exposed through machining.

- **Surface depressions** (Figure 1.1b) are caused by the deformation of the solid shell of a casting due to the internal pressure drop caused by solidification shrinkage [7]. The extent to which depressions develop is dependent on the formation of liquid encapsulation and the thickness of the solid shell.

- **Macrosegregation** (Figure 1.1c) occurs when the solute elements in the alloy are transported over length scales larger than the grain size [8, 9]. This causes depletion or enrichment in solute levels within the casting [10]. These changes in composition lead to variation in microstructure and mechanical properties within the casting [11].

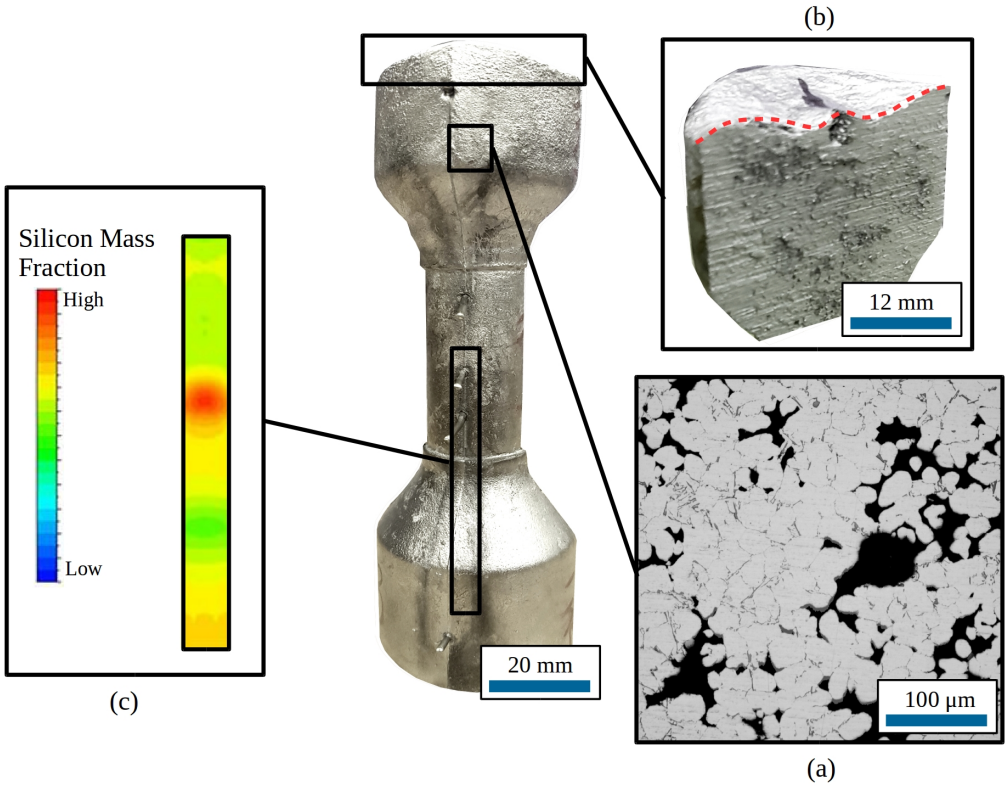

Figure 1.1: A sample casting depicting various shrinkage induced defects; (a) macroporosity in the top section of the casting, (b) a surface depression due to feeding phenomenon and (c) macrosegregation along the centerline of the casting.

In the next section, macrosegregation will be discussed in detail followed by a review of previous experimental and modelling studies. This will be followed by a brief description of the microstructure and solidification of A356. This information is essential to understand how macrosegregation occurs. Finally, the mechanical properties of A356 will be presented to appreciate the potential effects of macrosegregation on the alloy.

1.1 Macrosegregation

Macrosegregation refers to the variation of composition within a casting over length scales ranging from a few millimetres to several meters in large ingots [12]. Macroseg-

regation is considered to be a defect for several reasons. First, in the case of eutectic alloys, the increased amount of eutectic caused by variation of composition and increased number of hydrogen pores associated with higher amount of eutectic can severely reduce the fatigue life and performance of the cast components [11, 13]. Second, the compositional variations generated due to this phenomenon cannot be corrected practically using heat treatment, due to the low solid state diffusion rates of the solute and the large length scales. Third, macrosegregation results in the variation of mechanical properties within the casting due to the spatial variation of composition. Moreover, it can affect the final cost of the material in the case of expensive alloys. For instance, in the case of gold alloys, there should be a minimum of 58 wt% gold everywhere in a 14 carat gold alloy. However, macrosegregation can cause variations in the composition which result in an increase or decrease of the value in different sections [11].

To understand macrosegregation, it is first important to consider microsegregation and how interdendritic liquid is enriched. Referring to the growing dendrite shown in Figure 1.2, several isothermal control-volumes have been drawn from the tip to the base of the dendrite. The temperature in each control volume decreases with distance from the tip, while the fraction solid increases. Referring to the Scheil approximation, solute will be rejected into the liquid as solidification proceeds for hypoeutectic alloys resulting in enrichment of the solute element in the liquid as solidification progresses. In the case of near-eutectic alloys, enrichment continues until the liquid reaches the eutectic composition. The local enrichment of solute is a form of microsegregation.

If the locally enriched liquid is moved over longer distances within the casting, segregation occurs on the macro-scale. There are three main causes of macrosegregation associated with movement of enriched liquid [11]:

- Macro-scale transport of fluid due to solidification shrinkage (Figure 1.2b);
- Fluid motion due to convection (Figure 1.2c); and

- Fluid motion due to deformation of the semi-solid (Figure 1.2d).

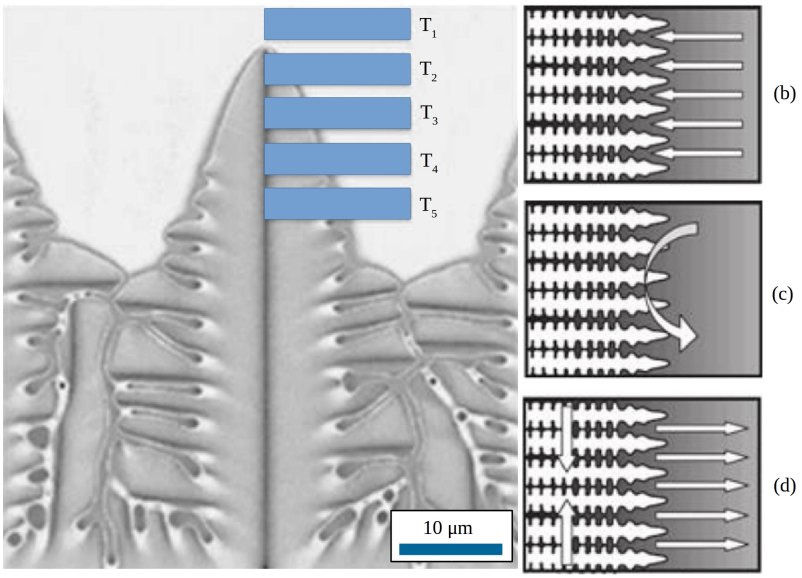

Figure 1.2: (a) Depiction of a dendrite. Moving down from the tip to the base of the dendrite, the local liquid is enriched in solute. Mechanisms of movement of the locally enriched liquid via (b) compensatory flows, (c) convection and (d) deformation of solid [11].

1.1.1 Experimental investigations

There have been many experiments reported that were aimed at understanding different types and aspects of macrosegregation. One of the first experiments was performed by Mehrabian [14]. In this research, the sole driving force for macrosegregation was assumed to be the flow due to solidification shrinkage and experiments were designed in a way that this flow was the only driving force operating. The casting used in these experiments had a rectangular geometry. Macrosegregation occurred in the length of the casting spanning to 25cm. This study concluded that a variety of apparently different types of macrosegregation in binary alloys were due to mass flow of interdendritic liquid to feed solidification and thermal contraction. In further studies, this group focused on macrosegregation of ternary alloys and macrosegregation due

to convective flow [15, 16]. It was concluded from these studies that gravity induced flows, generated due to changes in density in the liquid metal, play an important role in the resulting macrosegregation of large ingots where directional solidification is present [15].

Streat *et al.* studied macrosegregation in a directionally solidified lead-tin alloy using a radioactive tracer technique in 14cm long cylindrical moulds with 1.27cm diameter. It was shown that macrosegregation in this case resulted from the upward flow of less dense tin-rich interdentritic liquid during solidification [17]. Boettinger *et al.* investigated the effects of the solute gradient on macrosegregation during casting of a Pb-Sn alloy [18]. The macrosegregation in this study was characterized along the length of the solidified samples using two methods: X-ray Fluorescence (XRF) and a titration method. It was found that the convection caused by the solute gradient caused extensive macrosegregation.

In a study by Wang *et al.*, two sets of small cylindrical samples (5cm x 19mm) were prepared from a directionally solidified cylinder of length 5cm and diameter 9cm with compositions of Pb-15 wt% Sn and Pb-85 wt% Sn. Using detailed chemical composition measurements, segregation in the Pb-rich samples was observed with Sn content being higher at the top section. Macrosegregation in these alloys was found to increase with increasing thermal gradients and slower cooling rates. No significant segregation was observed in the Sn-rich samples since neither the temperature nor the composition gradients were favourable for convection [19].

Prescott carried out a series of experiments to investigate the effects of magnetic fields on macrosegregation using a lead-rich Pb-Sn alloy. In this research, a magnetic field was used to augment or oppose the thermal and solutal buoyancy forces. A simple hollowed-out cylindrical mould with length of 15cm, internal radius of 16 mm and outer radius of 63.5mm was used to conduct the experiments. When large enough ($\sim$ 5mT) upward magnetic forces were induced the circulation of the melt

was reversed and the solidification began at the top of the sample, which was a result of the magnetic field. The magnetic forces also enhanced solutal buoyancy, which was a significant source of macrosegregation in the alloy considered in this study. In another variant of the experiment downward magnetic forces were also applied, which aided thermal buoyancy and caused the initial solidification to occur at the bottom of the casting. In this case, the magnetic forces opposed solutal buoyancy and caused reduced macrosegregation [20].

Krane investigated the formation of macrosegregation in binary (Pb-Sn) and ternary (Pb-Sn-Sb) alloys in a rectangular mould of dimensions 254mm x 127mm x 89mm. In this study, the dominant cause of the macrosegregation was found to be buoyancy induced convective flows. He also found that the strength of shrinkage induced flow increased with solidification rate, but even for the highest solidification rates, macrosegregation effects were confined to small regions near the chilled wall. Krane employed rectangular-shaped castings and vertically sectioned them. He then removed specimens, dissolved them using nitric and hydrochloric acid and analyzed the composition using Atomic Absorption Spectroscopy (AAS) [21].

In an interesting study, Leon-Torres and co-workers investigated the effects of increasing gravity on solidification and macrosegregation of Al-Cu alloys. The experiments under increased gravity were conducted during parabolic flights where gravity was increased from 2 to 10g. A cylindrical mould was used in the experiments. In all cases positive segregation was observed next to the chilled wall, and similar to earlier studies, this was attributed to shrinkage induced flow [22].

Macrosegregation in higher melting point, ternary Al-Cu-Si alloys was studied by Ferreira *et al.* In this research samples with a cylindrical cross-section with length of 90mm and diameter of 20mm were directionally solidified. The results showed inverse segregation of copper and no segregation of silicon except for a short length of negative segregation at the bottom of the casting. These results were attributed

to the short mushy zone length [23].

In another study, Ojha and Tewari investigated the effects of mushy zone characteristics on macrosegregation using a quartz tube with length 30cm and diameter 6.5mm as a mould. They directionally solidified a Pb-Sn alloy with growth rates varying from 1 to $10\mu m/s$ in a positive temperature gradient. Large amounts of macrosegregation were observed in the castings. It was shown that macrosegregation increased with decreasing growth rates. They concluded that segregation in the mushy zone is a result of the combined effects of diffusion and convection. However, for low permeability conditions at higher distances from liquid solid interface, convection can be neglected [24].

Recently, the number of the detailed experimental investigations of macrosegregation being published per year has slowed. As modelling of this phenomenon has attracted more attention, experimental findings were generally concentrated on validating the results from these numerical simulations. Furthermore, to date, there has not been a systematic study reported on shrinkage-induced segregation as it applies to shape castings of commercial alloys. As discussed in previous paragraphs, majority of the conducted experiments were based on simple rectangular or cylindrical moulds.

1.1.2 Numerical studies

Fundamentally, the main task to predict the occurrence of macrosegregation is to model the composition distribution at the macro-scale in the presence of heat transfer and fluid flow phenomena. For a casting process, the heat transfer analysis involves predicting the temperature distribution and phase change throughout the casting at each time-step. As fluid flow and diffusion are the major causes of macrosegregation, these phenomena have to be modelled in parallel to predict solute distribution on the macro-scale. Depending on the focus, models of casting processes solve the relevant mass, momentum, heat and species transport equations.

Flemings *et al.* were one of the earliest contributors to the numerical analysis of macrosegregation [25]. They suggested that the main cause of macrosegregation in their experiments was due to interdendritic fluid flow caused by compensatory flow rather than by convection resulting from buoyancy. Thus, buoyancy effects were neglected in their study. They developed a model of macrosegregation for a 2D rectangular geometry considering only the flow of interdendritic fluid through a fixed dendritic network. This model was then validated with a number of carefully designed experiments. Mehrabian *et al.* extended Flemings's model to account for convective flow in the mushy zone [15]. The numerical results showed good agreement with the experimental results.

Ridder *et al.* coupled phenomena observed in the mushy zone to the bulk liquid in a rectangular 2D axisymmetric domain with 120mm in length and 80mm in diameter [26]. In this study, the bulk melt was coupled with the mushy zone using a multi-domain approach in which separate equations were solved for the bulk liquid and mushy zone regions. This method involved matching the pressure and velocity of both the mushy zone and bulk liquid regions at their interface. Although there was good agreement between the experiments and numerical simulation presented in this study (refer to Figure 1.3), this model was unable to predict the phenomena occurring in the casting such as remelting and double-diffusive convection, where two different density gradients (thermal and solutal) with different diffusion rates drive convective flow.

In a novel study, Bennon and co-workers proposed a method to implicitly couple the mushy zone (coexisting solid and liquid) regions for binary alloys by a set of momentum, energy and species equations [27,28]. In this so called continuum model, the mushy zone was treated as a solid - liquid mixture and individual phase conservation equations were integrated into a set of mixture conservation equations. This method partially solved issues occurring in multi-domain models, such as the need to calculate

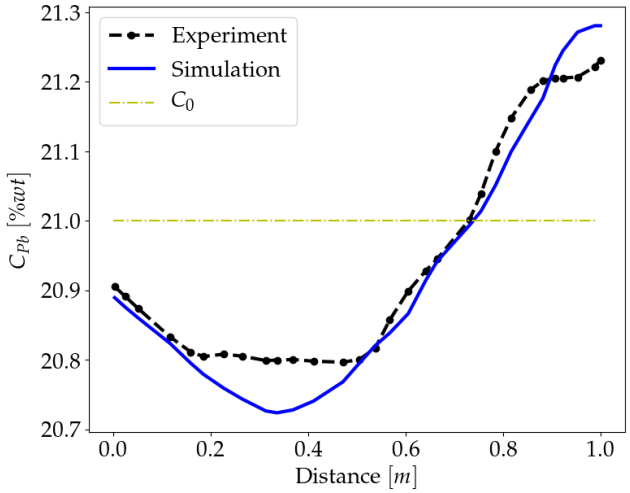

Figure 1.3: Comparison of experimental and theoretical segergation profiles in Sn-21wt% Pb ingot from Ridder *et al.* [26].

the liquid/solid interface shape and double-diffusive convection in the liquid resulting from thermal and solutal buoyancies. Nevertheless, comparing the numerical results to experimental data, the agreement was only fair. Voller *et al.* reported a similar method for binary alloys, however, their model incorporated a better approximation of solute redistribution at the micro scale [29]. Voller *et al.* used a simple square geometry to apply this model on solidification of Ammonium Chloride (refer to Figure 1.4). It was concluded that the model developed by Flemings and co-workers can be used to analyze solidification under equiaxed solidification conditions, but a continuum model is necessary for columnar dendritic regions. A hybrid of the two modelling approaches has been proposed as a best practice for robust macrosegregation analysis. As the previous models mainly concentrated on 2D problems, Chakraborty and Dutta extended the hybrid model to consider macrosegregation in 3D [9]. The main focus of this study was to model the three-dimensional double-diffusive convection in a cubic enclosure. It was shown that three-dimensional convective flows cause a substantial solute redistribution in the transverse section of the casting, which could not be described with a two-dimensional model.

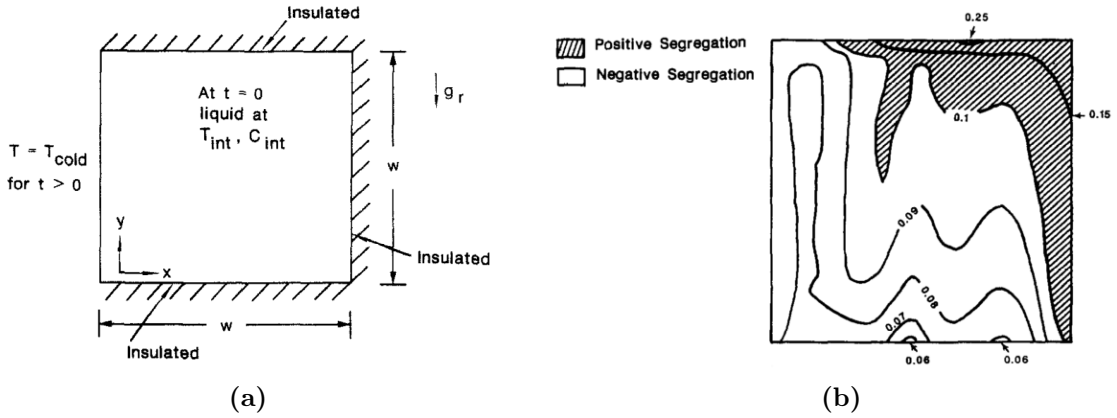

(a) **(b)**

Figure 1.4: Geometry (a) and the macrosegregation profile (b) from Voller *et al.* [29].

Ni and Beckermann presented a different method for modelling solidification. In this model, the solidifying melt is considered to have two distinct phases, in which each phase is treated separately and interactions between the two phases are considered explicitly [30]. The two-phase model allows for relaxed assumptions regarding thermal equilibrium and species diffusion in the solid phase. However, the drawback of this method compared to continuum models is that twice as many partial differential equations must be solved, which can be time-consuming especially in the case of large problems.

Ni and Incropera proposed additional modifications to the equations of the continuum and two-phase models, to consider more sophisticated phenomena such as solutal undercooling, nucleation and solid movement in the form of floating or settling crystals [31, 32]. By coupling the continuum model with the two-phase model, several assumptions in the original continuum model were relaxed to consider the aforementioned phenomena. The main focus of this work was to describe solute transport through the motion of floating crystals. In similar work, Vreeman *et al.* studied the evolution of macrosegregation caused by the redistribution of alloying elements through the movement of free floating dendrites in direct chill casting of aluminum alloys [33, 34]. They also modified and coupled the transport equations from the con-

tinuum model and the two-phase model. However, in this research, the two-phase region was characterized as a slurry of free-floating dendrites and a rigid permeable dendritic matrix saturated with interdendritic liquid. For each of these phases, distinct and separate momentum equations were solved. Vreeman *et al.* applied this method on an axisymmetric casting with height of 350mm and diameter of 400mm on Al-4.5wt%Cu. The results are shown in Figure 1.5

Krane and Incropera investigated the solidification of ternary alloys [35, 36]. In this study, they modified the binary continuum mixture equations for the transport of mass, momentum, heat and species to account for a third component. Numerical simulations were performed to observe the convective flows and macrosegregation patterns in the Pb-Sn-Sb system. The results from numerical analysis was compared the experimental results and fair agreement was observed.

Rappaz and Gandin presented a new method to model grain structure formation during solidification [37]. The foundation of this model was based upon the use of a cellular automata technique to model nucleation and grain growth. They then coupled this method to an enthalpy based finite element heat flow calculation. The so-called Cellular Automata-Finite Element (CAFE) analysis interpolates the temperature at a cell location from the macro-scale finite element predictions to calculate the nucleation and growth of grains [38]. This method was further developed by Lee and co-workers to model both grain growth and pore formation during solidification [39]. They reported good correlation with experimental results. Guillemot *et al.* further developed the original CAFE model to account for transport and sedimentation of equiaxed grains [40]. They also verified the results, however, it was concluded that refined experimental data were required to further validate segregation profiles. Zhang and colleagues coupled cellular automata with the finite volume method instead of finite element method to investigate the macrosegregation occurring in a 2D domain [41]. A 10mm x 10mm square geometry was used to model

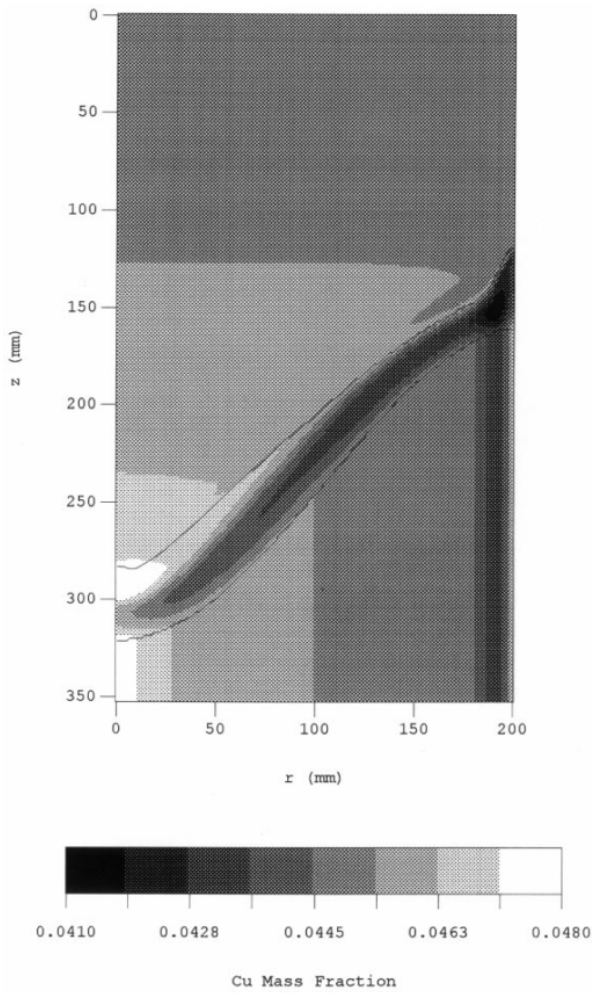

(a)

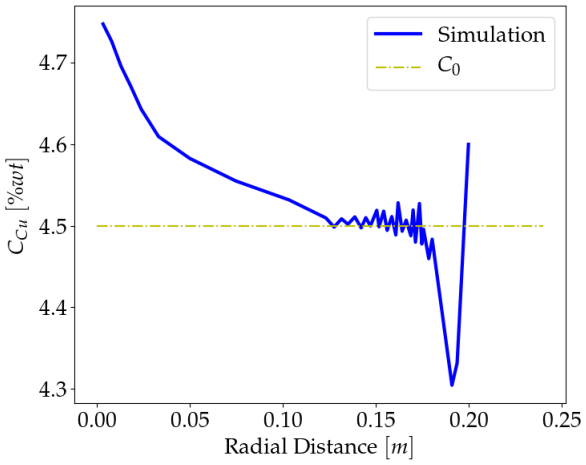

(b)

Figure 1.5: Copper segregation field (a) and copper composition variation on z=150mm from Vreeman *et al.* [34].

the solidification of Al-7wt%Si, results of which are shown in Figure 1.6. The model was verified by using previous experimental solidification studies. The incorporation of a cellular automata model requires finer mesh (e.g. 50 micron elements), as it is employed to predict phenomena at the micro scale. Therefore, it is significantly time and comutationally intensive [38].

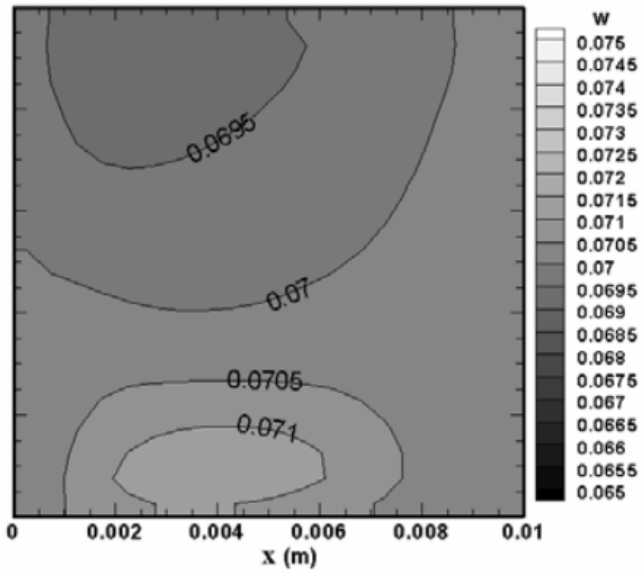

Figure 1.6: Concentration contour for solidification of Al-7wt%Si from Zhang *et al.* [41].

To sum up, there has been extensive research done on modelling solidification and macrosegregation. The hybrid model, among the modeling approaches proposed, has proven to be time efficient and accurate due to the number of differential equations solved. Other more accurate methods such as the two-phase model and especially the CAFE model require more time to simulate the solidification and macrosegregation. Therefore, many commercial software packages, such as CFX and FLUENT, utilize the hybrid model to simulate solidification.

1.2 Image processing for defect quantification

The quantification of defects observed in castings is a challenging task. Most of the reported quantification techniques for pore detection and classification, and macrosegregation quantification (e.g. X-ray Micro-Tomography (XMT), Energy-Dispersive X-ray Spectroscopy (EDX) and XRF) are confined to small sections, which may not be representative of the overall casting. Some studies report results from larger sections, however, these results lack accuracy since discrete points were used to generate defect maps of sections. [42].

Image analysis is an effective method to classify defects. One of the first studies to quantitatively characterize defects in castings was reported by Tewari *et al.* where they utilized a digital image analysis-based experimental technique to characterize the spatial arrangement of microporosity [43]. In this research, several overlapping optical micrographs were taken from a 3mm x 4mm area and stitched into a high-resolution montage for use in analyzing the pores. In a similar study, Prakash and colleagues used computational microstructure analysis to characterize and quantify porosity in a high pressure die-cast magnesium alloy over a 2mm x 19mm sample [44, 45]. The size and distance distribution and clustering tendency was quantified by this image processing technique. The method was reported to be quick and efficient to detect and distinguish between gas and shrinkage porosity.

Quantification of macrosegregation in steel was investigated by Straffelini *et al.* using image analysis. Continuously cast steel was vertically sectioned and then several images were taken from the transverse section. Two parameters were defined, based on the dimension of segregated areas and distance between two nearest segregated areas. The microstructure was observed to be more homogeneous as these two parameters decreased [46]. In a different context, Roy designed an apparatus to take discrete micro images from predefined positions of a large aluminum sample, shown in Figure 1.7a [47]. He then determined the eutectic area fraction in every micrograph and

linearly interpolated between two consecutive points to construct an overall eutectic map for the sample, shown in Figure 1.7b.

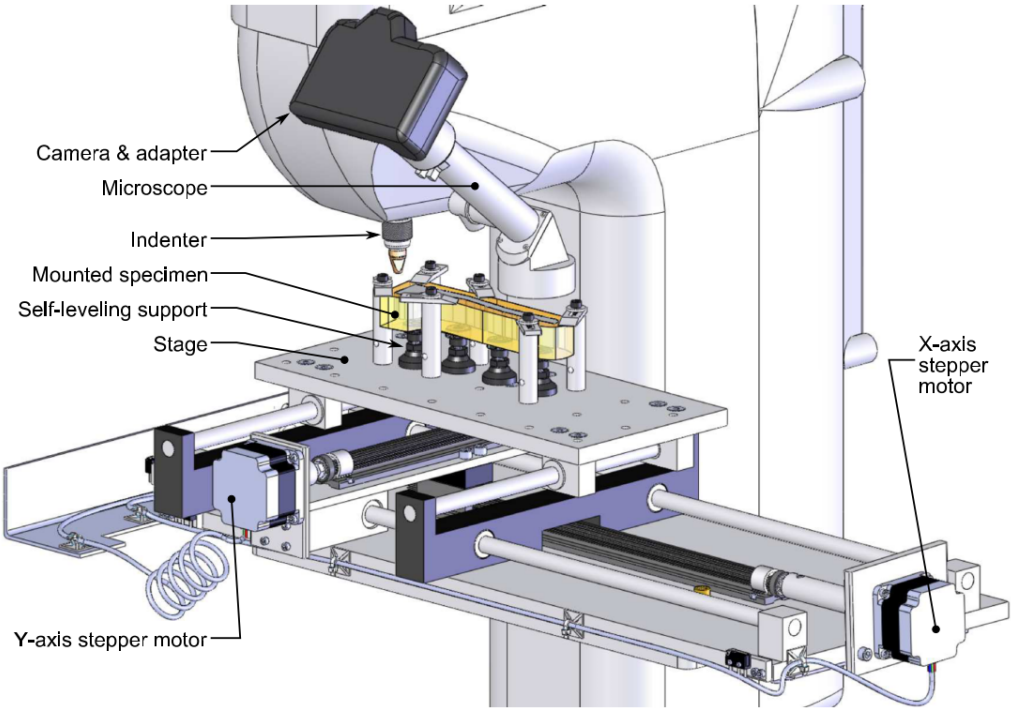

(a)

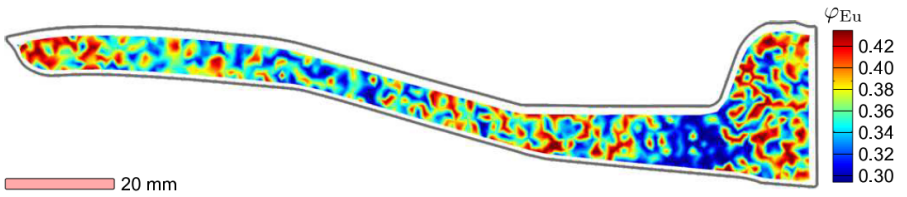

(b)

Figure 1.7: Profiling apparatus consisting of a CNC stage and digital-SLR camera installed (a) and resulting eutectic area fraction profile on a wheel sample (b), from the work of Matthew Roy [47].

1.3 Solidification of A356

Aluminum alloy A356 is a hypoeutectic Al-Si-Mg alloy widely used in the automotive and transportation sectors. The characteristic composition of this material is given in Table 1.1.

Table 1.1: Composition (wt%) of unmodified A356, balance Al

Si	Mg	Fe	Ti	Na	Ni	Cu	Zn	Ca	Zr
6.50-7.50	0.20-0.45	<0.13	<0.12	<0.01	<0.01	<0.01	<0.01	<0.01	<0.01

The as-cast (AC) microstructure consists of primary aluminum dendrites (α-Al), surrounded by an Al-Si eutectic (Figure 1.8). Other tertiary phases, such as α-intermetallics or β-intermetallics (β-Al_5FeSi and π-$Al_8FeMg_3Si_6$), may be present due to melt impurities. The solidification sequence of this alloy starts with the nucleation and growth of primary dendritic α-Al. This is followed by the β-Al-Si eutectic and β-intermetallics. The remaining liquid, enriched in Si, Mg and Fe, forms Mg_2Si precipitates and engages in complicated ternary and quaternary reactions, producing π-intermetallics [10, 11].

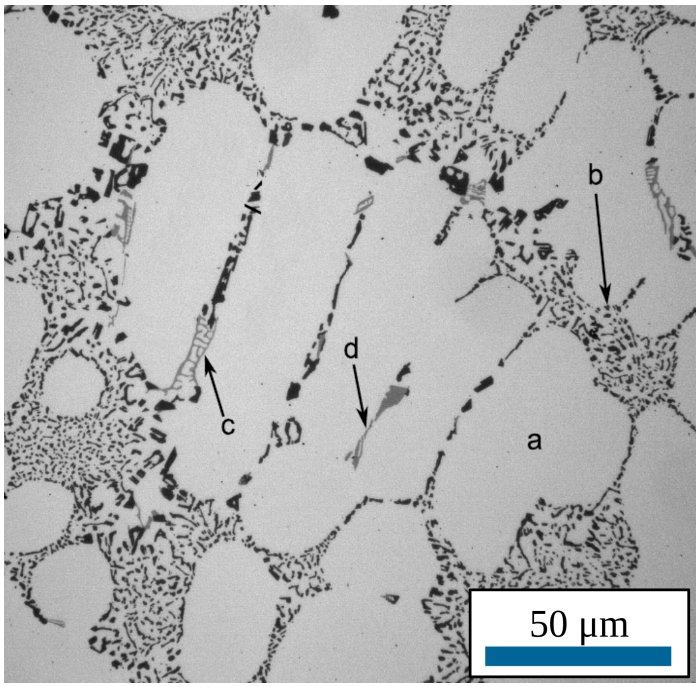

Figure 1.8: Example of A356 microstructure in the AC condition, displaying (a) α-Al, (b) Al-Si eutectic and (c) intermetallic and (d) a secondary Mg-Si rich region [47].

The solidification of A356 is often modelled using the binary Al-Si system (Figure

1.9) [1, 48]. Starting from the fully liquid phase, as the temperature falls below the liquidus temperature, α-Al begins to form with low silicon composition. As the temperature decreases, the volume fraction of α-Al increases, while the surrounding liquid becomes enriched in silicon until it reaches the eutectic temperature. At this temperature, α-Al has the highest silicon content (1.65 wt%Si) and the liquid is at the eutectic composition (12.6 wt%Si). Further decrease in temperature will cause the enriched liquid to undergo eutectic transformation, where it solidifies into lamellae of aluminum and silicon [10, 11].

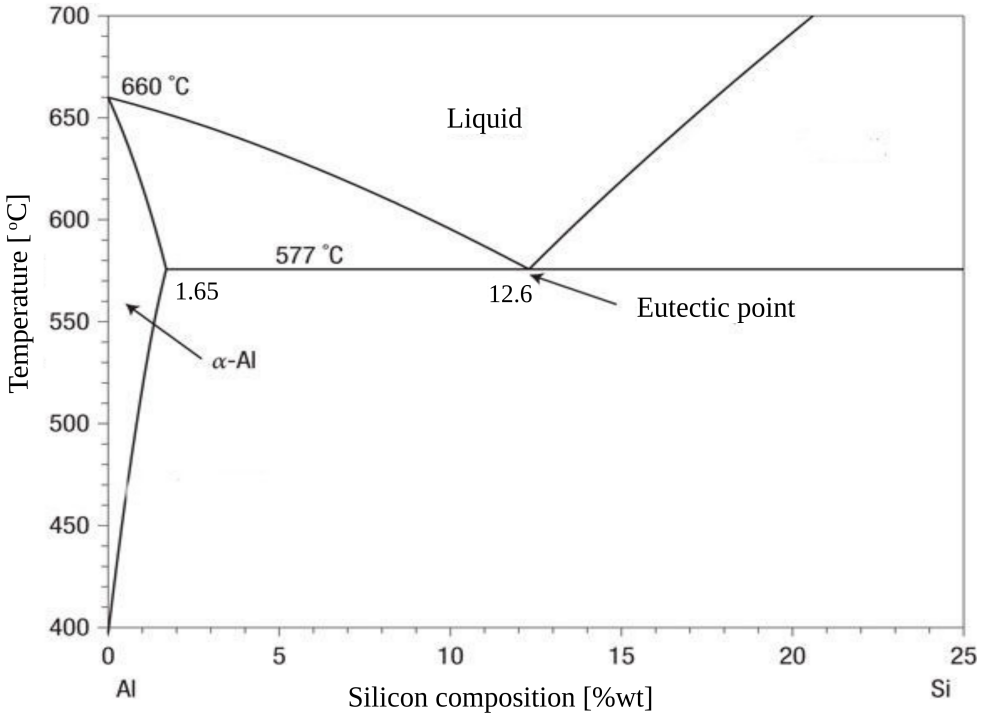

Figure 1.9: Al-Si phase diagram.

A356 is rarely employed in the AC condition owing to a lack of homogeneity and the detrimental effects on the mechanical properties of coarse plates of Si present in the eutectic. Several heat treatment schedules are commercially employed, with the most prominent being T6. Most of these schedules consist of solutionizing, water quenching and then a combination of natural and artificial aging. Both the duration and temperature at which these treatments are carried out decide the final mechanical

properties. The T6 schedule used in this research is as follows:

- Solution treat at 540°C for three hours.
- Quench in water at 60°C
- Artificially age at 170°C for 6 hours with no natural aging.

The solution treatment is applied to induce three phenomena to occur: dissolution of Mg_2Si particles, chemical homogenization and eutectic-Si structure modification. The Mg_2Si precipitate that forms during the last stages of solidification is readily soluble in α-Al at the typical solutionizing temperatures and will dissolve given enough time. In the AC state, solute elements are typically highly segregated due to dendrite formation. Solution treatment serves to chemically homogenize the casting, thereby improving solid solution strengthening [47].

The changes to the eutectic-Si structure imparted by solution treatment also play an important role in determining the final mechanical properties. While modified Al-Si-Mg alloys contain fairly refined fibrous eutectic-Si, this is further refined during solution treatment by the processes of fragmentation and spheroidization. The AC fibres break into particles at elevated temperature and gradually spheroidize in order to minimize surface energy of the Al-Si interface. With longer treatment times, coarsening occurs. Larger Si particles develop facets and coalesce with other nearby particles to minimize surface area in regions of high Si concentration [47].

For the quench operation, the water temperature is selected to maximize cooling rate while concurrently limiting thermal stress development. A high cooling rate is necessary to suppress precipitation when cooling from the solution treatment temperature to room temperature. This produces a high degree of solute supersaturation as well as retaining a larger number of matrix vacancies. If the cooling rate is too slow, non-uniform precipitation will occur, localized at grain boundaries or sites of high dislocation density [47].

Artificial aging is a precipitation heat treatment process. It consists of taking

previously solution treated components and holding at a static temperature for a period of time. The process is necessary to precipitate small particles coherent with the surrounding matrix which are finely dispersed particles to resist dislocation glide. In Al-Si-Mg alloys, the supersaturated solid solution resulting from the solutionizing process transforms to a stable phase plus a metastable precipitate phase, β. The rate of precipitation, as well as the precipitate morphology, is dependent on temperature, time degree of supersaturation and diffusivity. At high temperatures, diffusion occurs rapidly even when supersaturation is low. The inverse is true for low temperatures [47].

1.4 Mechanical properties of A356

In previous sections, the microstructure and solidification path of A356 were discussed. This section will discuss the impact of microstructure on mechanical properties of A356. This will be done by looking at the results from several studies where the effects of Dendrite Arm Spacing (DAS) and composition were investigated on mechanical properties.

Microstructure refinement, which results in a corresponding strength increase, can be achieved by decreasing the solidification time during casting. By decreasing solidification time, the cooling rate during solidification is increased which results in decreased primary and secondary DAS. A number of studies have investigated the effects of DAS variation on the yield strength in aluminum alloys [49–53]. Figure 1.10 shows the yield strength versus DAS from five separate studies. These studies consider A356 alloys in the AC and T6 heat treated state with a range of DAS. As shown in Figure 1.10, the yield strength decreases as the microstructure becomes coarser. This effect is often expressed in terms of the Hall-Petch equation [54]:

$$\sigma_y = a + b \cdot d^{-1/2} \tag{1.1}$$

where a and b are constants and d is spacing. The definition of spacing, however, changes from grain size for pure aluminum to dendrite cell size (the width of individual dendrite cells) in aluminum alloys with 1.6 - 2.5wt%Si to nearest-neighbour distance between Si particles in alloys with 5.3 - 25wt%Si [55]. The majority of the published studies on this topic use the inverse square root of the DAS to construct a relationship between microstructure and yield strength [56–58]. An expression in the form of Equation 1.2 has been fit to the data presented for A356.

$$\sigma_y = a + b \cdot DAS^{-1/2} \tag{1.2}$$

As depicted in Figure 1.10, the expression exhibits a reasonable correlation (R^2 equal to 0.62 and 0.81) to both the AC and T6 heat treated data.

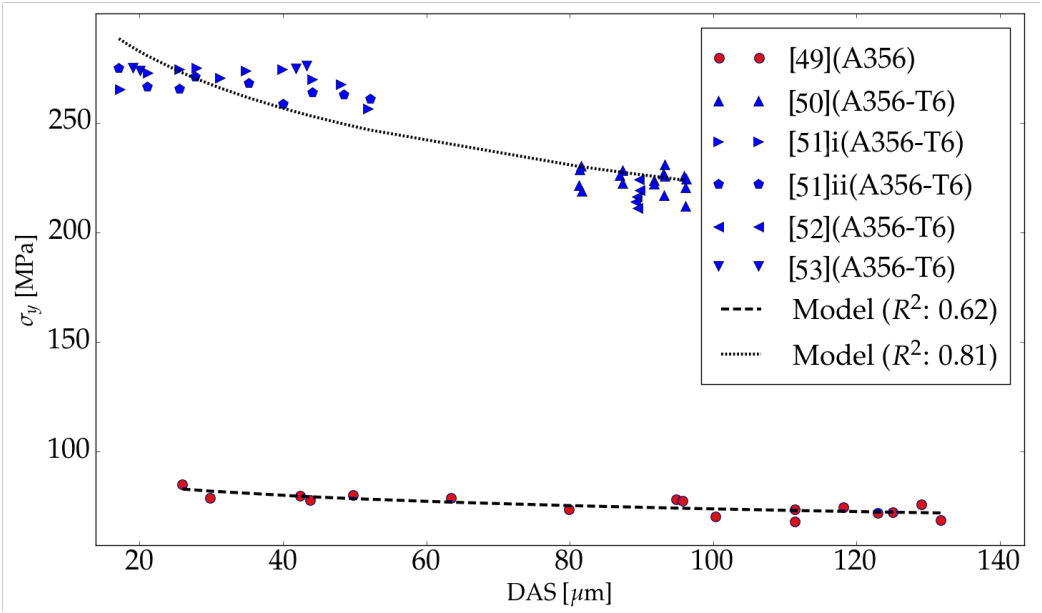

Figure 1.10: σ_y versus DAS for AC and heat treated A356 alloys with fitted expressions.

Elzanaty [59] and Kalhapure *et al.* [60] studied the effect of variation in silicon content on yield strength in aluminum alloys in the as-cast condition. In both studies, yield strength and silicon content were shown to exhibit a linear correlation over the hypoeutectic region. A 50-100% increase in the yield strength was observed for silicon

contents ranging from 4 to 11wt%. It should be noted that the hypoeutectic region has been studied extensively since most of the commercial Al-Si-Mg casting alloys, such as A356, are from this family. Barresi *et al.* [61] and Moller *et al.* [62] investigated the effect of magnesium content on yield strength. These studies showed that a ∼0.2% increase in the yield strength occurs over the range of 0.2 to 0.4wt%Mg. Since the effects of silicon content and DAS on yield strength are more dramatic, the effect of magnesium content can be neglected for compositions between 0.2 and 0.4wt%.

Roy *et al.* conducted a comprehensive study to characterize the constitutive behaviour of AC A356 over a range of temperatures and strain rates [63]. In this study several phenomenological and physically-based constitutive expressions were fit to the experimental data. It was found that the modified Hollomon expression (Equation 1.3) was the most versatile expression for fitting the results over the range of conditions tested [63, 64].

$$\sigma_H = K(\epsilon_0 + \epsilon)^n \tag{1.3}$$

where K and n are constants corresponding to strength and strain-hardening, respectively. ϵ_0 is a constant indicating the yield strain, which is essential for correctly predicting the flow stress [64].

In a more recent study, Haghdadi *et al.* used artificial neural networks to predict the hot deformation behaviour of an A356 alloy. They used a series of compression tests in various temperature ranges and strain rates to train the artificial neural network. The predicted results were then compared with a strain-compensated type constitutive equation. They concluded that the artificial neural network model is statistically accurate and is a robust tool to predict high temperature flow behaviour of A356 aluminum alloy [65].

1.5 Scope and objectives

As discussed in the previous sections, there has been little attention given to macrosegregation resulting from the movement of enriched liquid caused by compensatory flow, especially for the case of industrially-relevant shape castings such as wheels and engine blocks. The objective of this research is to study the macrosegregation in shape castings of aluminum alloy A356 and assess its effect on the localized constitutive behvaiour. To accomplish this objective, four main tasks have been identified:

- To develop an experimental casting set-up that will produce macrosegregation;
- To develop and verify a method to quantify solute redistribution that has occurred on the scale of the casting;
- To develop and validate a mathematical model capable of predicting the formation of macrosegregation; and
- To develop and apply correlations between silicon mass fraction, microstructure and constitutive behaviour.

The first step in this research is to design an experimental apparatus to isolate and exaggerate macrosegregation. A dumbbell shaped casting with adjustable cooling rates is used to this end. Designing the casting apparatus is critical to the success of the research. The concept for this casting is based on two cylindrical volumes linked by a joint pipe. The mould is fabricated from thin walled copper tube stock which has a low thermal mass relative to the casting. This limits the initial heat removal / solidification and also allows rapid heat extraction when augmented with additional cooling where required. Each casting is instrumented with thermocouples at various locations to support validation of the thermal-fluid flow model framework described below. The rationale behind this design is that by controlling the cooling rates on the different sections of the casting one can partially solidify the mid-section,

so that there is enriched liquid available for transport. As solidification occurs in the bottom of the casting the enriched liquid in the middle section will compensate the shrinkage. This will cause a variation in composition as the middle part will become solute deplete and the bottom section will be solute enriched.

The second task in this project is to develop a method to provide a detailed map of segregation throughout the casting. Previous methods of segregation mapping, such as EDX, are not suitable for this task because the size of the samples used to conduct this type of analysis are fairly small, and usually in order to map a large section, several small samples are cut from the section and analyzed. Therefore, an image processing technique is adopted to quantify solute redistribution. The intended method uses pixel-based analysis to calculate the silicon area fraction throughout the casting. To evaluate the accuracy of this analysis technique, the initial analysis is performed using idealized artificial microstructures. Following this initial development, this technique is used to assess real microstructure.

A numerical simulation is developed to further understand the formation of macrosegregation caused by movement of enriched liquid. An incremental approach to model development is taken where physical phenomena and boundary conditions are added to the base model step by step, validating the model on each stage with simple cases from literature. The numerical analysis is formulated using ANSYS FLUENT, a commercial CFD software capable of solving the relevant governing equations to predict the fluid flow/heat transfer occurring during solidification.

Finally, a correlation between silicon area fraction, microstructure and constitutive behaviour is developed by performing careful tensile tests on samples from a series of castings with different silicon content. Specialized plate castings are particularly useful in this experiment as the microstructure varies steadily with distance from the walls. These correlations can be very useful to predict the tensile strength as a function of location in industrial components.

Chapter 2

Constitutive Behaviour of hypoeutectic Al-Si-Mg Alloys[1]

As the overall objective of this thesis is to study macrosegregation and its effect on the local constitutive behaviour in A356 alloy shape castings, this chapter examines the effects of silicon content and microstructural variation on the mechanical properties of hypoeutectic Al-Si-Mg alloys (off-spec A356 alloys) in the AC and heat-treated conditions. A series of plate castings were produced from Al-Si-Mg alloys where the Si content was varied and the constitutive behaviour was characterized. The results were then used to establish an empirical expression correlating DAS, silicon content and the heat-treated state with flow stress based on a modified Hollomon equation. This expression, combined with a numerical model predicting macrosegregation and solidified microstructure, provides an essential tool to predict the mechanical properties throughout a geometrically complex component.

[1]Portions of this chapter have been published in:

- *Khadivinassab H.*, Maijer D. M., Cockcroft S. L., "Constitutive Behviour of Macrosegregated A356", Material Science and Engineering A, (2017) – under revision

2.1 Experimental methodology

2.1.1 Material

Starting from unmodified A356 alloy, six alloys were made by either adding pure aluminum[2] or Al-Si master alloy with 50wt% silicon. The resulting alloys, summarized in Table 2.1, have a range of silicon contents.. It should be noted that the additions of Al and Al-Si master alloy to A356 alloy meant that the nominal Mg content varied in the range of 0.2wt% - 0.35wt% for each alloy which is within the ASTM specification (i.e. 0.20 to 0.45wt% Mg)[3]. It should also be noted that the presented compositions in Table 2.1 are the predicted compositions. A standard deviation of 5% has been assessed as feasible in these alloys because the Si composition in the base alloy was reported with a standard deviation of 5% according to Table 1.1.

Table 2.1: Composition of fabricated alloys used in constitutive behaviour experiments.

Alloy name	wt% Al	wt% Si	wt% Mg
TAL01	95.80	4.00±0.20	0.20±0.01
TAL02	94.75	5.00±0.25	0.25±0.01
TAL03	93.70	6.00±0.30	0.30±0.01
TAL04 (A356)	92.65	7.00±0.35	0.35±0.02
TAL05	91.66	8.00±0.40	0.34±0.02
TAL06	90.67	9.00±0.45	0.33±0.02
TAL07	89.67	10.00±0.5	0.33±0.02

2.1.2 Experimental setup

Castings in the form of plates were produced using the casting setup shown in Figure 2.1. The casting setup consists of an insulated, steel pour basin and runner system connected to a steel mould (via the bottom) to generate the plate castings. The charge for each casting was produced by cutting small pieces of melt stock, weighed

[2]Aluminum 1060
[3]ASTM B26/B26M - 09

on a small scale, depending on the recipe which were combined in a Silicon Carbide crucible. The crucible was then placed in a resistance furnace, set to 750°C, to melt the charge. Prior to each casting, the melt was degassed to reduce the hydrogen content by bubbling Ar gas through the melt for 20 minutes. Meanwhile the mould was preheated to 300°C. The crucible was removed from the furnace and allowed to cool while monitoring the temperature with a handheld thermocouple. The metal was poured into the pour basin once it reached a temperature of 700°C using an automated pouring device, shown in Figure 2.2, to ensure reproducibility during the pouring stage. The main design criterion for the plate casting was to produce different cooling rates at the mid-plane, horizontally across the plate. The variation in cooling rates results in a variation in DAS within the plate. It is expected that each plate produces samples with finer DAS closer to the sides and coarser DAS in the middle.

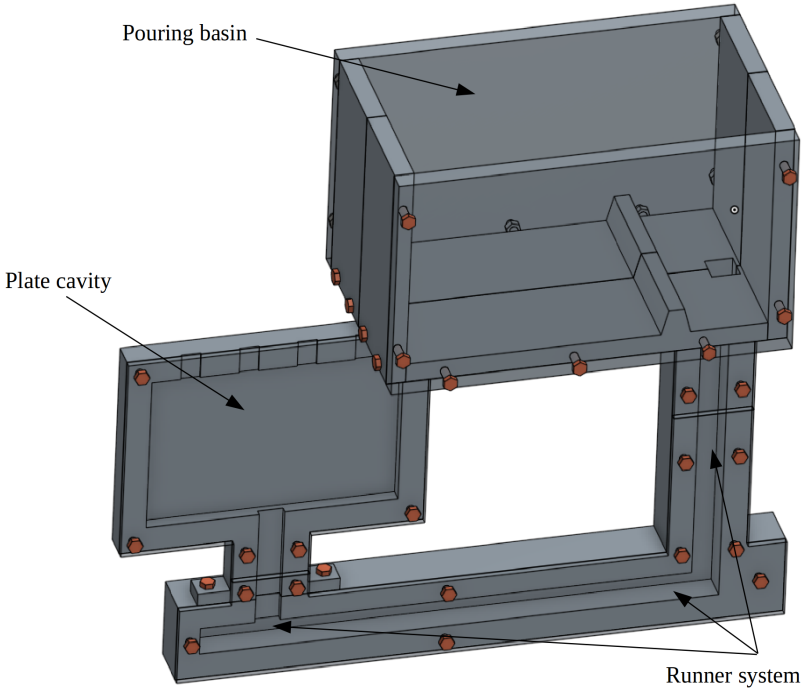

Figure 2.1: Illustration of the plate casting mould.

Overall, ten plates were cast using this method. The composition of the cast alloys are summarized in Table 2.1. Seven plates, fabricated using alloys TAL01 - 07,

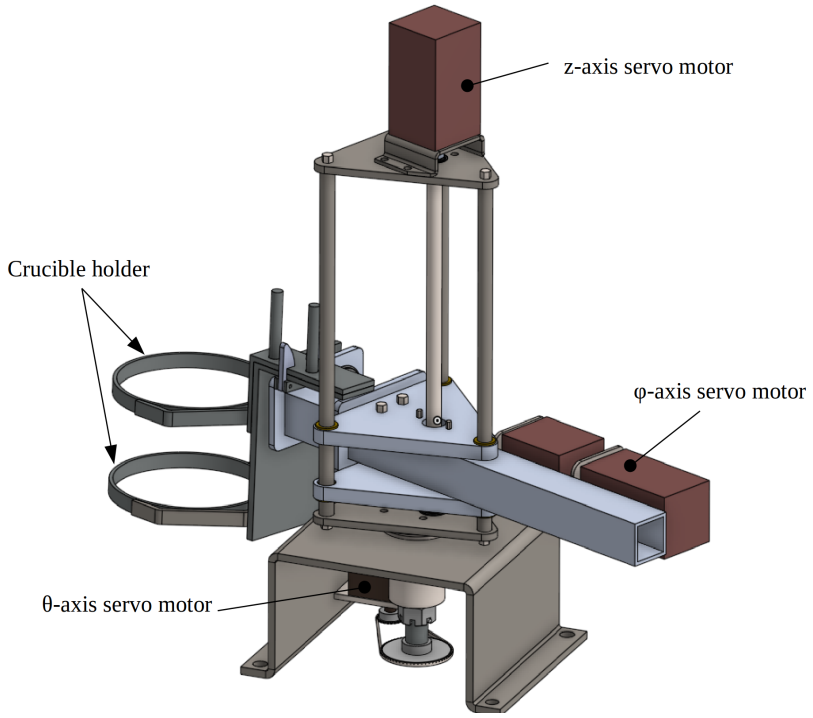

Figure 2.2: Illustration of the automatic pouring device.

were used in the AC condition. The three other castings, cast from TAL01, A356 and TAL07, were heat-treated to a T6 condition. The T6 schedule used in this research is as follows:

- Solution treat at 540°C for three hours.
- Quench in water at 60°C
- Artificially age at 170°C for 6 hours with no natural aging.

2.1.3 Characterization

Tensile test samples were extracted from each plate using a water jet cutter. Figure 2.3 shows the number, location and size of the samples cut from each plate. A total of eleven samples were obtained from each plate. Tensile tests were performed on an Instron 8872 machine equipped with a 100 kN load cell. The tests were conducted at a fixed displacement rate of 2 mm/min until failure. A 1-inch extensometer was attached to each sample in order to measure the gauge length displacement during the

tests. The conversion of the raw force-displacement data, outputted by the device, to true stress-true strain data was based on Dieter [66] and the yield strength was calculated based on 0.2% offset method [66]. It should be noted that these methods are in accordance with the ASTM standard [4].

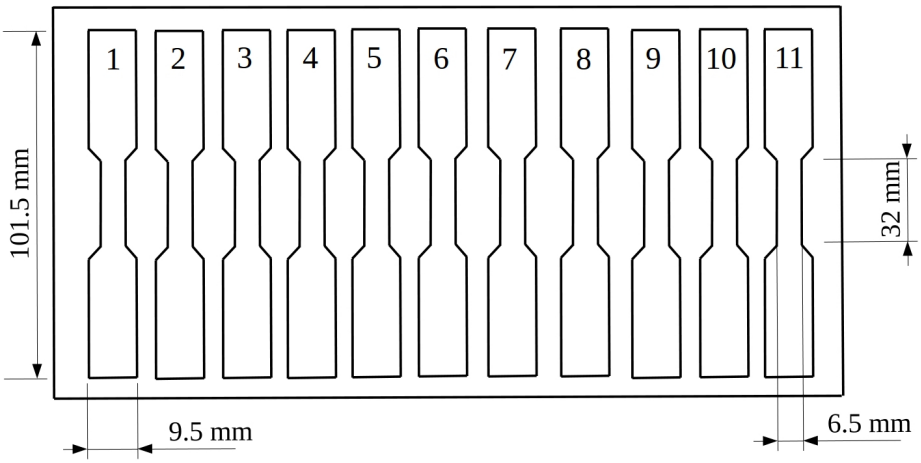

Figure 2.3: Drawings of the location and naming of each tensile sample cut from the plates and dimensions of the samples. Note that all the samples have a thickness of *12.5mm*.

Metallographic samples were extracted from each tensile sample location in the plate using different combinations of handsaw, Electro-Discharge Machining (EDM) and bandsaw. Specimen size permitting, samples were polished using an automatic polishing machine[5] with 240, 320, 400, 600 and 1800 grit Si-C paper. This was followed by two secondary polishing steps with 6 and 1 μm diamond paste. A Nikon Eclipse MA200 inverted microscope and Nikon DS Fi1 digital camera, with NIS-Elements software were used to take images of the microstructure for follow-on analysis. Examples of the microstructural images from each of the alloys cast for this study are shown in Figure 2.4. The eutectic area fraction increases from TAL01 to TAL07 consistent with the increase in Si content.

[4]ASTM E646 - 16
[5]Buehler Phoenix BETA Grinder Polisher with Vector Power Head

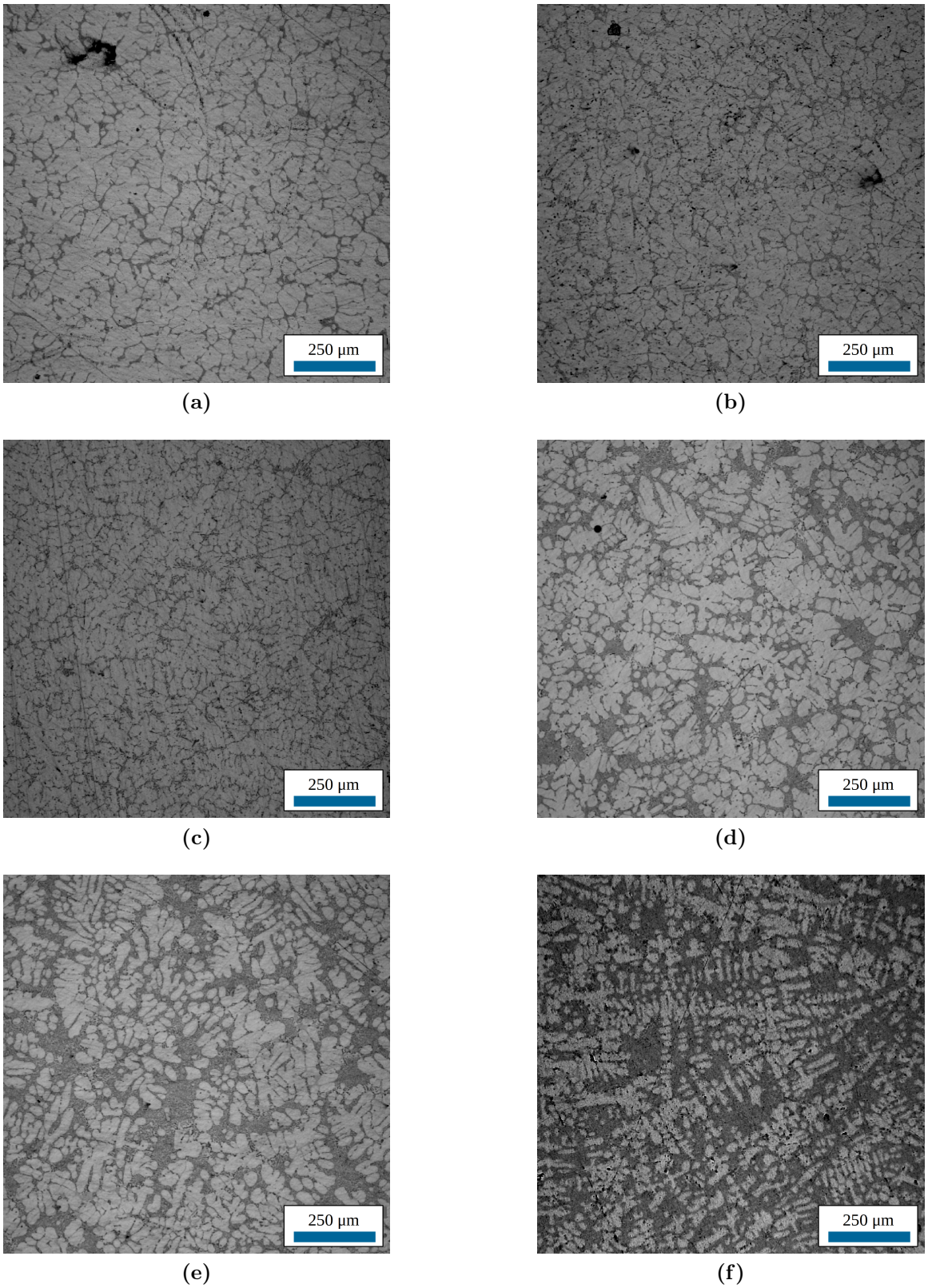

Figure 2.4: Sample microstructure of created alloys, TAL01 (a), TAL02 (b), TAL03 (c), TAL05 (d), TAL06 (e) and TAL07 (f) taken from position 2.

DAS measurements were performed manually using ImageJ [67]. The procedure applied to measure the DAS is shown schematically in Figure 2.5. After loading a micrograph into the software, a line is manually drawn across secondary dendrite arms, intersecting at least 5 dendrite arms. The length of the line is then divided by the number of inter-dendrite arm spaces and scaled accordingly. This procedure was carried out three times for each image and the values were then averaged. It should be noted that this method is in accordance with GM standards [6]

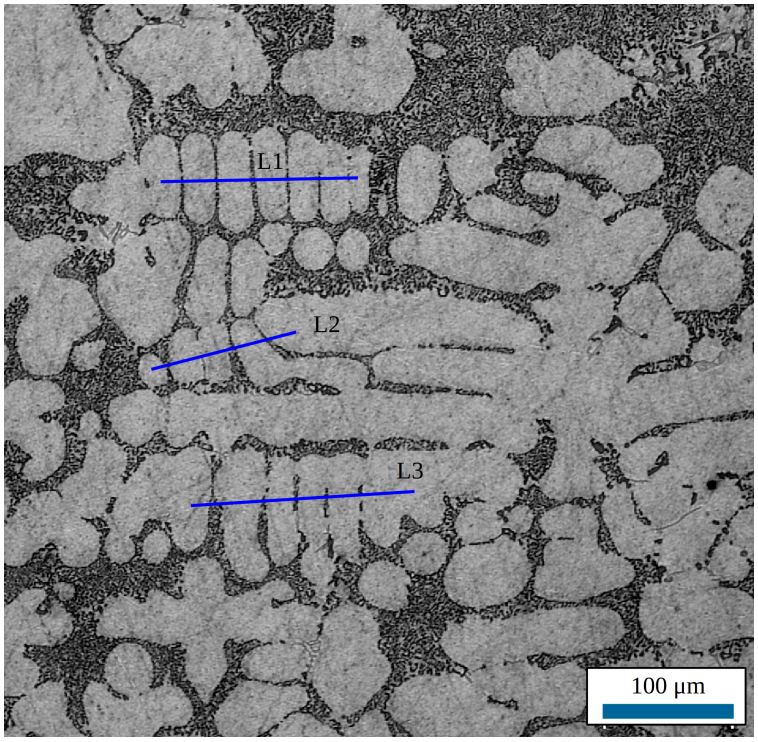

Figure 2.5: Example of DAS measurement technique, showing three different measurements.

Porosity and silicon area fraction measurements were all conducted by image analysis using a Python code developed for this purpose. First, the images were segmented by grey-scale into three parts; pores, primary and secondary. In order to determine the porosity area fraction, the area of the image segment representing pores was divided by the overall area of the image. To determine the silicon area fraction, the

[6]GMW16436

area of the image segment representing silicon was divided by the total non-porous area.

2.2 Experimental results

Five curves from samples with a range of silicon compositions and different heat-treated states have been selected to represent the 110 stress-strain curves generated during the testing and are shown in Figure 2.6. These representative curves will be used in this section to discuss the fitting procedure and to assess the goodness of fit of the proposed phenomenological expression. The results shown in Figure 2.6 are for samples cut from the same location in each plate (i.e. position 2 in Figure 2.3). Qualitatively, Figure 2.6 indicates that the tensile strength increases with increasing silicon content. Furthermore, as expected, the T6 heat-treatment results in a significant increase in tensile strength of the material. It can also be seen that the slope of the curves in the elastic region exhibits more or less the same value. This value was calculated to be 72.4GPa with 1.3% error across all the samples, which is consistent with the elastic modulus of the material [68]. Since the elastic modulus is an intrinsic property of the material and the measured value here exhibits a low error across all the samples, it was considered a constant and treated as being independent of Si content in follow-on analysis.

The yield strength for each tensile sample was determined using the 0.2% offset method. The average yield strength for each plate and the standard deviation are summarized in Table 2.2. Looking at the quantitative data, the average yield strength increases with increasing silicon content.

Figure 2.7 shows the average DAS calculated from all the samples measured at each location in the plates. As discussed previously, the casting process used in this study generates plates with varying DAS; coarser in the middle and finer on the sides. Because of the symmetry in the shape of the plate about the centerline of the inlet,

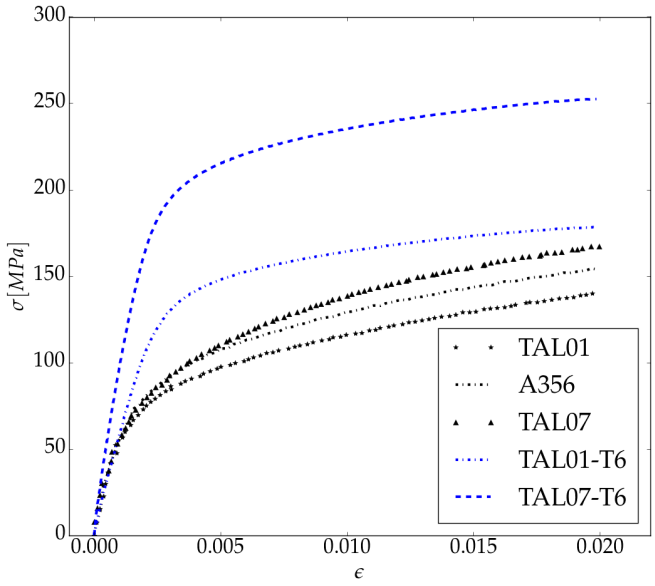

Figure 2.6: Stress-strain curves for five selected samples.

Table 2.2: Average yield strength and standard deviation determined for each alloy.

Alloy name	TAL01	TAL02	TAL03	A356	TAL05	TAL06	TAL07
σ_y	85.01	86.24	90.27	96.68	94.72	97.71	99.66
SD [MPa]	5.81	8.19	8.92	2.70	6.91	4.06	2.01

Alloy name	TAL01-T6	A356-T6	TAL07-T6
σ_y	152.36	197.24	237.08
SD [MPa]	11.37	7.07	8.05

symmetric DAS data was expected from the castings. The dashed line drawn on Figure 2.7 is the average DAS calculated at each position from the centerline and can be used to assess this symmetry. Overall, the DAS is observed to be higher than the average on one side and lower on the other. This may be due to asymmetry in the cooling process due to the structure of the mould. A small decrease in the DAS was observed in the mid-plate location. The dip in DAS was present in every plate and may be the result of refinement caused by solidified particles being transported to the middle of the casting by convection.

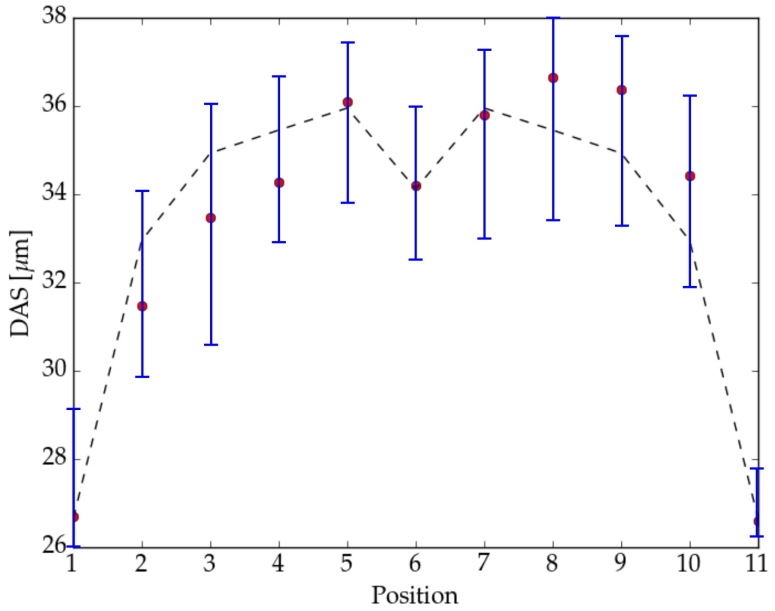

Figure 2.7: DAS values at each location in the plates, where the red circles represent the average DAS, blue bars indicate the variability and dashed line shows the symmetric average values of DAS in each location.

Figure 2.8 illustrates the porosity volume fraction averaged across all samples at each location in the plates. Due to degassing, the porosity values observed were very small and were not expected to affect the strength of the material [69]. Thus, the effects of porosity were not considered in this study.

2.3 Constitutive equation development

In order to develop a constitutive equation relating the flow stress to the silicon content and DAS, the stress-strain data was randomly divided into two groups. A training set consisting of 80% of the data and a cross validation set consisting of the rest. In order to develop an expression for the flow stress, first Equation 1.3 was fit to each of the training data sets. Then an equation was developed for n, K, and ϵ_0 as a function of Si wt%, DAS and T6 state. Afterwards, the overall fit was assessed using the cross-validation data set.

After calculating the yield stress for each sample using 0.2% offset method, a

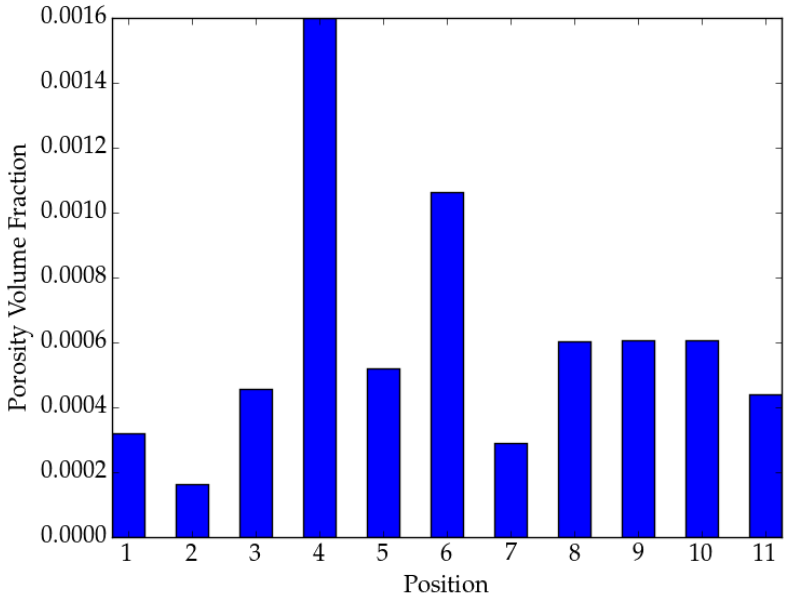

Figure 2.8: Average porosity over all the plates.

linearized form of Equation 1.3 was fit to each data set separately. Values for the work hardening, n, and strength, K, constants were found from the slope and y-intercept of ln σ-ln ϵ curves. The value of ϵ_0 was extracted directly from the yield stress data. Figure 2.9 shows the representative experimental data and the calculated flow stress based on the fits to Equation 1.3. The average R^2 obtained for the fit to each of the training data sets individually was 99.2%

In the second stage of fitting the data, each of the parameters, n, K and ϵ_0, were fit to Equation 2.1. This equation is a combined form of the modified Hall-Petch equation [54] and a linearly varying silicon content correlation. A binary **T6** parameter has been incorporated and multiplied through the equation, to consider whether the **T6** heat treatment has been applied. **T6** is one if a T6 heat-treatment has been applied or 0 if the metal is in the AC condition.

$$f = a + b \times \mathbf{T6} + (\mathbf{T6} + 1)(c \times C_{Si} + d \times \mathrm{DAS}^{-1/2} + e \times C_{Si} \times \mathrm{DAS}^{-1/2}) \qquad (2.1)$$

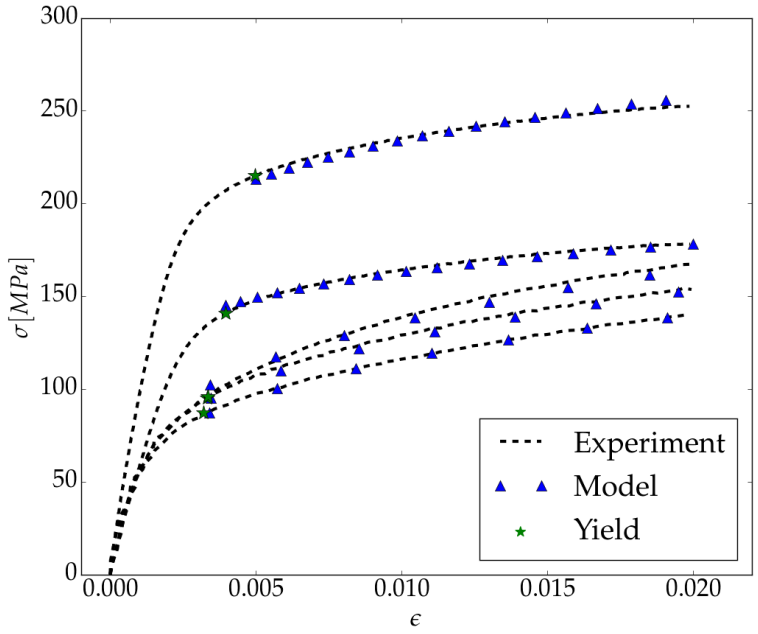

Figure 2.9: Stress-strain curves with fitted models.

Table 2.3: Values of fitted coefficients in equation 2.1 for n, K and ϵ_0.

Parameter	a	b	c	d	e	R^2
n	0.185	-0.226	0.013	0.456	-0.069	92.7%
K	-240.454	-746.425	87.187	3318.584	-414.728	56.8%
ϵ_0	1.973e-3	-6.437e-5	1.43e-4	4.46e-3	-3.968e-4	93.5%

where C_{Si} is the silicon weight percent, and the parameters a, b, c, d and e are constants. It should be noted that constants c, d and e control the influence of silicon content, DAS and combined effect of these parameters, respectively.

Table 2.3 shows the calculated constants and the R^2 of the fit for each parameter. The fit for both n and ϵ_0 exhibit high R^2 values, but the fit for K is poor. To resolve this issue, the modified Hollomon equation was fit to each curve again. However, in this step, only the K value was adjusted and the values of n were based on Equation 2.1. The revised coefficients for K are shown in table 2.3 along with the new R^2

Table 2.4: Values of fitted coefficients in equation 2.1 for K.

Parameter	a	b	c	d	e	R^2
K	-89.096	-598.938	56.984	2440.074	-243.955	83.8%

for the fit to this parameter. The R^2 value for K increased significantly by carrying out the second step. The average R^2 for the multi-step fit to the training dataset is 96.5%.

Figure 2.10 compares the experimental data from the representative tests with the calculated flow stress curves based on the DAS, silicon content and heat treatment state. Figure 2.11 illustrates the measured versus predicted values for all the data points in the cross-validation data set. The R^2 for the final model evaluated with all available data is 95.1%. It is noticeable that the R^2 for the training dataset is higher than that of cross-validation dataset. The reason for this difference is that the fit was tailored for the training dataset, therefore, it is expected that this fit would exhibit a higher R^2.

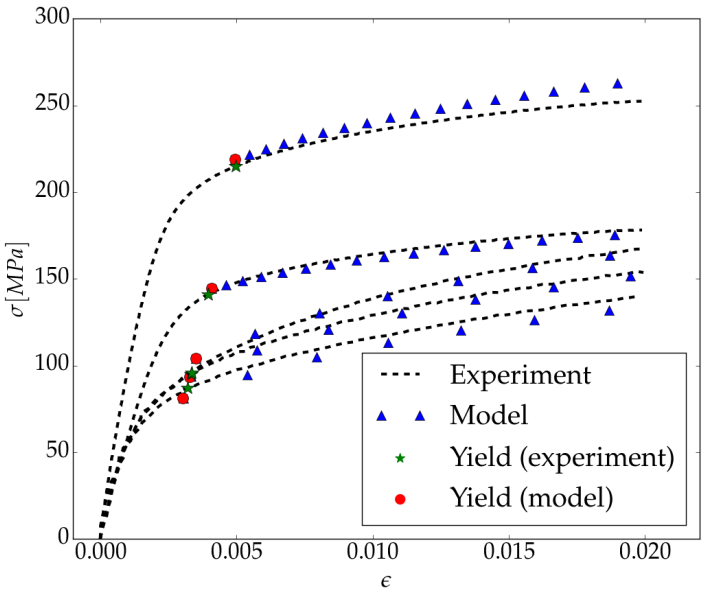

Figure 2.10: Representative experimental stress-strain curves with a fitted model.

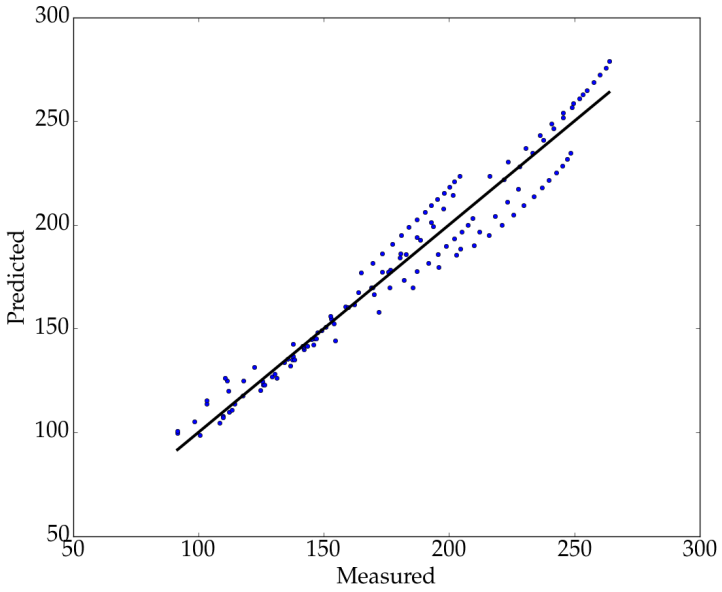

Figure 2.11: Predicted vs. measured flow stress for cross-validation data-set.

2.4 Sensitivity analysis

A sensitivity analysis has been conducted to assess the significance of each term in equation 2.1. The details of this analysis is presented in Appendix 6.2. The sensitivity results show that the parameters are more sensitive to changes in Si content rather than DAS. This suggests a similar behaviour for the flow stress. Furthermore, applying the T6 heat treatment to the alloy seems to have a small effect on the contributions of the terms dependent on Si content. This is expected since applying a T6 heat treatment does not change the silicon content and its contribution to the flow stress. Overall, the contribution of all the parameters are significant in the equation.

The sensitivity of parameters n, K and ϵ_0 based on changes in DAS and Si content are shown in Figures 2.12-2.14. The sensitivity is defined as percent change from the base value. For this study, the base values for DAS and C_{Si} are $35\mu m$ and $7wt\%$, respectively. The data shows that there is a high variability in parameter ϵ_0. Parameters n and K, on the other hand, show lower sensitivity to changes in DAS and

Si content. it should also be noted that for low DAS values, parameters n and K are less sensitive to changes in Si content. Conversely, these parameters show high sensitivity for changes in Si content when DAS is high. ϵ_0, on the other hand, shows high sensitivity to Si content over the whole analyzed DAS range. Considering the relative importance of these parameters, since n is an exponentiation factor even small changes in this parameter are magnified in the overall flow stress results. On the other hand, small changes in ϵ_0 would not have significant effect on the final stress result as it is a summation factor.

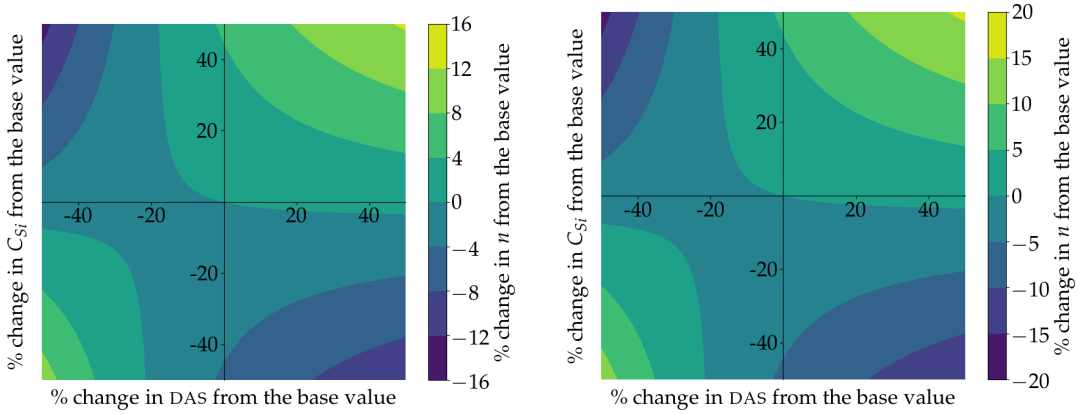

Figure 2.12: Sensitivity analysis of parameter n for (a) AC and (b) T6 condition.

Figure 2.15 shows the sensitivity of the calculated yield strength based on the aforementioned DAS and Si content conditions. As can be seen, in both AC and T6 conditions with low DAS, yield strength exhibits low sensitivity to changes in Si content and vice versa.

2.5 Discussion

Parameter n can be viewed as a indicator of the work-hardening and formability of a material, where increasing n increases the formability [70]. The results from Figure 2.12 suggest that although applying a T6 heat treatment increases strength,

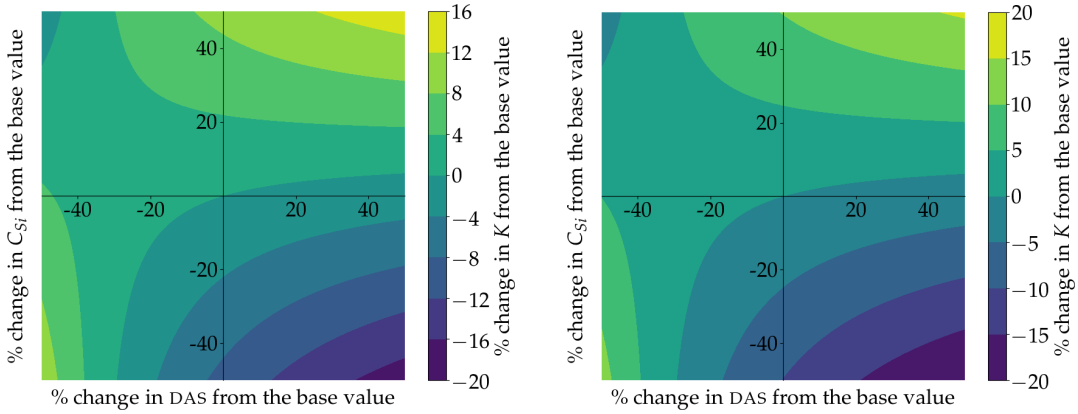

Figure 2.13: Sensitivity analysis of parameter K for (a) AC and (b) T6 condition.

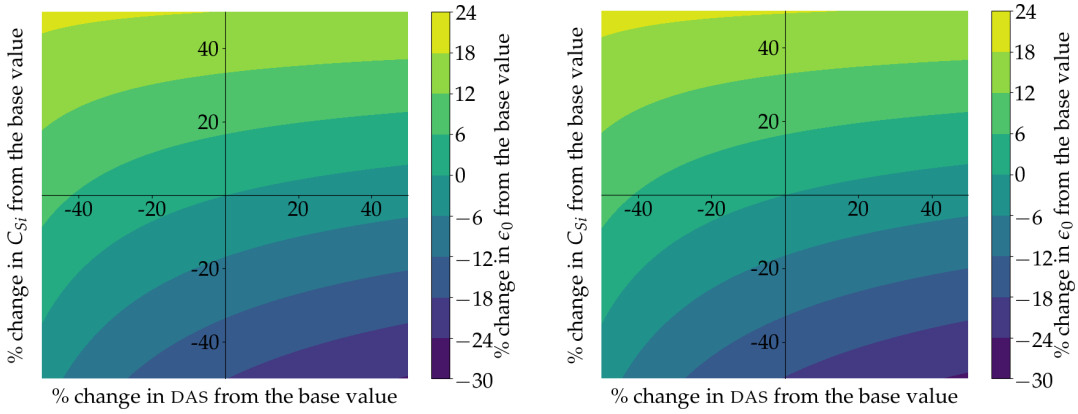

Figure 2.14: Sensitivity analysis of parameter ϵ_0 for (a) AC and (b) T6 condition.

it reduces the formability of the material. Additionally, the effects of DAS and C_{Si} are intertwined. High DAS-high C_{Si} and low DAS-low C_{Si} conditions yield better formability than high DAS-low C_{Si} and low DAS-high C_{Si} conditions in both the as-cast and T6 conditions.

Parameter ϵ_0 can be considered to be the amount of strain-hardening that the material received prior to the tensile test [66]. The results from Figure 2.14 suggest that initial strain-hardening is highly dependent on the variation of Si content in both T6 and as-cast conditions; the higher the silicon content, the higher the initial

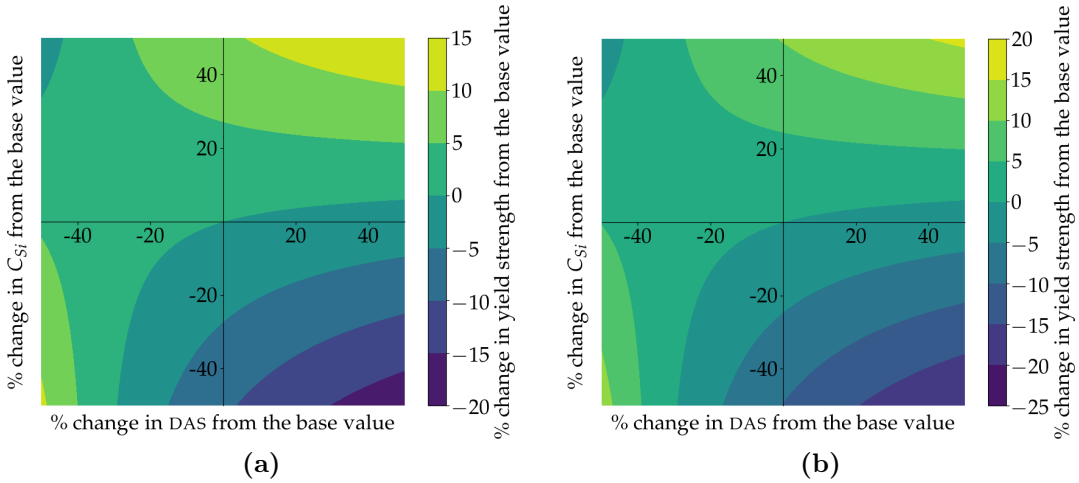

Figure 2.15: Sensitivity analysis of yield point for (a) AC and (b) T6 condition.

strain-hardening. This shows that initial strain-hardening is an intrinsic property of the alloy, mostly depending on the composition of the alloy rather than the cooling condition.

Experimental results as well as the developed model suggest that yield strength variation is higher for the T6 case compared to the AC case. Looking at table 2.3 the maximum yield strength variation for the AC case is 14.65 MPa where, this value is is 84.72 MPa for the T6 case. This means that by applying T6 heat-treatment to a part where there is macrosegregation would result in a much higher variation in yield strength.

The developed and verified constitutive equation can be utilized in solidification simulations to predict the mechanical behaviour of an Al-Si-Mg alloy. This could be especially useful where casting manufacturers are interested in incorporating this technique in their simulations to show that their parts can satisfy the designer's strength requirements throughout the geometry. Furthermore, the proposed model could fit into a through-process modeling methodology where the complete manufacturing process is simulated to provide a detailed prediction of the state of the part which can then be used as an input to a model of in-service performance.

2.6 Summary

The constitutive behaviour of hypoeutectic Al-Si-Mg alloys in both the as-cast and T6 heat treated conditions has been experimentally characterized through an extensive set of tensile tests. The data was used to fit a modified Ludwig-Holloman expression with parameters n, K and ϵ_0 as a function of DAS, Si content and T6 state. The final equation exhibits a fit with R^2 of 95.1% over the test dataset. Analyzing the results the following can be concluded:

- Apart from DAS, silicon variation in A356 castings, especially castings where macrosegregation is present, plays a crucial role in the strength of the material.
- The maximum yield strength occurs when DAS is low and Si content is high and the minimum yield strength occurs when DAS is high and Si content is low.
- High DAS-high Si content and low DAS-low Si content results in better formability in both AC and T6 conditions.
- Application of a T6 heat treatment results in reduced formability of the material.
- The Initial strain-hardening (ϵ_0) is mostly dependent on Si content.
- T6 heat treatment results in a higher yield strength variation in a cast part where macrosegregation has occurred.

With the development of this expression, the local flow stress behaviour in an A356 casting where macrosegregation is present can now be characterized. This equation can also be used in conjunction with solidification simulation as a predictive tool to estimate the flow stress distribution after solidification.

Chapter 3

Characterization of Macrosegregation in Eutectic Alloys[1]

As explained in the literature review, results from other methods, such as EDX, are not practical for assessing the variation of composition over a large cross-sectional area. This chapter presents an image processing method that has been developed to characterize the macrosegregation occurring on cross-sections of the castings produced for this study. The method utilizes a combination of image segmentation, pixel-to-pixel analysis and tessellation techniques to construct a quantitative map of the solute distribution on large samples. Compared with methods reported previously in the literature, the current method is robust and can be applied to samples with large irregular cross-sections. The accuracy and validity of the method has been assessed through a series of artificially designed micrographs.

3.1 Methodology

3.1.1 Analysis overview

The initial step to analyze the spatial variation of segregation in a sample is to construct an image montage of the microstructure over the entire area that is to be analyzed. This can be done through different techniques, the most common one being

[1]Portions of this chapter have been published in:

- *Khadivinassab H.*, Maijer D. M., Cockcroft S. L.,"Characterization of Macrosegregation in Eutectic Alloys", Materials Charcterization, (2017)

optical microscopy. In order to make a montage, the cross-section is first prepared (i.e. a suitable section identified, extracted and polished). Then, a sequence of images of the microstructure covering the entire surface of the sample cross-section is acquired. These images are then segmented into the desired phases. Several methods can be utilized to segment the images, such as the Gaussian Mixture Model and K-means [71]. Although these methods are quite accurate, when it comes to a large set of images, they are not time-efficient [71]. The recommended method in this case is to use Otsu thresholding, then implement appropriate morphologies to eliminate the "salt and pepper" noise in images [71].

In order to visualize the variation of segregation, a tessellation map is overlaid on the montage and the area fraction of the alloying element is then calculated in each mesh element. The area fraction is then converted to mass fraction based on a method that have been developed. The spatial variation of segregation in the contour map is strongly dependent upon the number of elements used in the mesh. For small numbers of elements, the generated contour map represents the area average of the mass fraction and is therefore quite coarse. An increase in the number of elements reduces the size of each element, potentially to the point where each element may contain only one microstructural phase. In this case, the measured area fraction becomes a binary representation because it is either completely filled with one phase or not. The optimal mesh size for the tessellations in this study were determined by calculating a quantity referred to as the Average Maximum Difference (AMD) using a simple algorithm.

After the optimization stage, the image is divided into small triangular sections based on the determined mesh size. Subsequently, the mass fraction of the desired phase is determined in each triangular section. The data then gets written into an input file for the Tecplot360 visualization software [2], which can be used to visualize

[2]Tecplot360 website: http://www.tecplot.com/products/tecplot-360/

and further analyze the segregation map.

The following sections will describe the analysis procedures in a greater detail.

3.1.2 Image segmentation

Image segmentation is one of the more challenging steps in conducting macrosegregation characterization analysis. Previous studies on this particular problem utilized image histograms to segment the microstructure [45, 47]. This method, however, has its shortcomings as different phases might have large overlaps, which then results in an inaccurate segmentation map.

To overcome this issue, a method based on Otsu thresholding has been used in this study. Otsu thresholding is a histogram based thresholding method. Assuming a bi-modal histogram, this algorithm searches for a threshold that minimizes intra-class variance [72].

In the approach applied in this work, the dark pixels representing pores were first identified manually and extracted from the data, leaving only the lighter pixels belonging to microstructural phases. Otsu thresholding was then applied to cluster the pixels representing primary and secondary phases. Nonetheless, the histogram for the remainder of the data points might not be of bi-modal form. In these cases, Otsu will identify only one cluster instead of two. In order to resolve this issue, the histogram was equalized using the Contrast Limited Adaptive Histogram Equalization (CLAHE) method before the application of the Otsu method. After successful thresholding, a combination of morphological operations were applied to the segmented image to fine-tune the clusters.

3.1.3 Meshing

After segmenting each of the individual micrographs and stitching them together, the high resolution montage was divided into smaller sections. This can be done through different algorithms depending on the accuracy and efficiency needed. A truss-based

meshing algorithm has been used in this work. Truss-based meshing, developed based on Persson's work [73], is a method that utilizes an iterative technique to refine a mesh defined using a physical analogy of a truss structure, where points in the mesh are nodes of the truss structure. Considering a force-displacement function for the members that makeup the truss, the code solves for equilibrium at each step. At every iteration, the nodes are moved by the calculated force and Delaunay triangulation is used to adjust the edge topology [73]. After calculating the displacements, the nodes outside the bounds of the shape are pushed back to the boundary. This process is carried out until the overall force in the truss system is within an acceptance criteria, i.e. a pseudo-equilibrium state.

One of the challenges in this technique is to properly define the geometry. Persson used a signed distance function to define simple geometries and combined them to represent more complex geometries [73]. This, however, lacks the ability to represent real-life geometries in detail. Therefore, a new geometry representation technique was defined based on the negative mask of the image. Figure 3.1 shows a sample image and its automatically generated negative mask which is suitable for meshing.

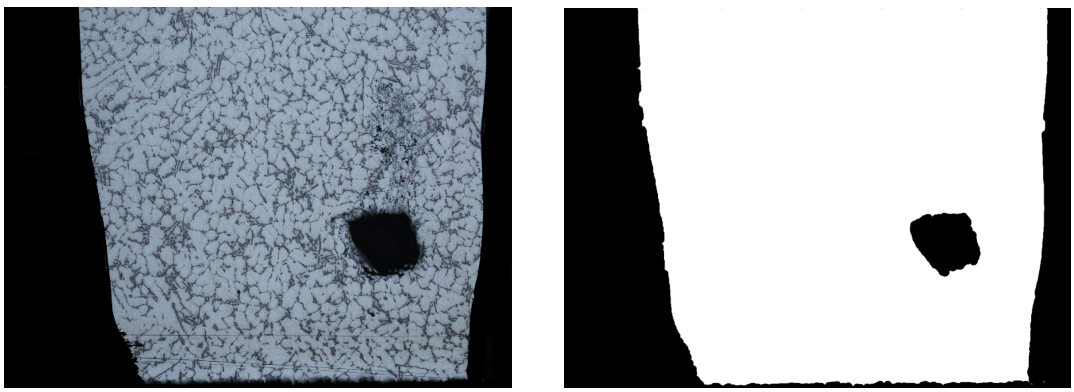

(a) **(b)**

Figure 3.1: Sample image (a) and its negative mask (b).

3.1.4 Area fraction to mass fraction conversion

The first step to convert the phase area faction, calculated from the segregated phase assessment, to mass fraction is to know its relation to volume fraction. From a stereological point of view, there are only a few bulk microstructural parameters that can be assessed by analyzing a 2D surface, where volume fraction is one of them [74]. According to Kaplan [74], the volume fraction is equal to the area fraction if the cross-sectional plane is randomly positioned.

The next step in determining the mass fraction is to convert volume fraction. This operation is highly dependent on the magnification and resolution of the micrograph. For low magnification images, constituents of the eutectic phase can be difficult to distinguish. Thus, the approach proposed here is to determine the eutectic area fraction first and calculate the mass fraction of the alloying element. For high magnification images where the constituents of eutectic phase can be distinguished, the area fraction of the alloying element can be calculated directly and converted to mass fraction. It should be noted that, this method assumes the alloying element is present as a pure phase. For the case of A356 and similar Al-Si-Mg alloys, since the initial composition of Magnesium is small relative to the composition of Silicon, percentage of contribution of Mg_2Si precipitates can be neglected and Silicon can be regarded as a pure phase.

The conversion of eutectic area fraction to mass fraction of the alloy element in the case of low resolution images can be accomplished by using the Scheil equation [11]. After manipulating the Scheil equation, the initial composition can be extracted as (Equation 3.1):

$$C_0 = \frac{C_e}{\varphi_e^{(C_s/C_e)-1}} \tag{3.1}$$

where C_s is the maximum solubility of the alloying element at the eutectic temperature

and φ_e denoted eutectic area fraction. It should be noted that C_0, C_e and C_s are all in atomic percentages. Equation 3.2 is then used to convert C_0 to a commonly used weight percentage.

$$wt\%B = 1/(1 + \frac{100 - at\%B}{at\%B}\frac{M_A}{M_B}) \tag{3.2}$$

where M_A and M_B are the atomic masses of components A and B in a binary alloy, respectively.

To convert the area fraction of an alloying element to mass fraction in the case of high resolution images, the lever rule may be applied based on a eutectic phase diagram (shown in Figure 3.2). The volume fraction of secondary phase (i.e. β) can be calculated at room temperature by the lever rule shown in Equation 3.3. Note that compositions are in atomic percentages rather than weight percentages. The local composition can then be determined by modifying Equation 3.3 to Equation 3.4.

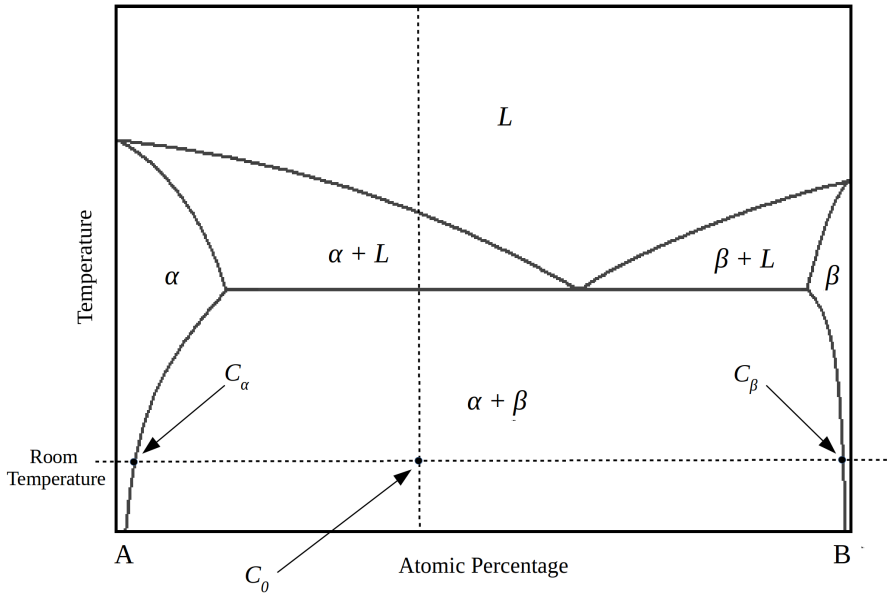

Figure 3.2: Eutectic phase diagram.

$$V_f = (C_0 - C_\alpha)/(C_\beta - C_\alpha) \tag{3.3}$$

$$C_0 = \varphi \times (C_\beta - C_\alpha) + C_\alpha \tag{3.4}$$

where C_α and C_β are maximum solubility of component B in phase α and component B in phase β at room temperature, respectively.

Lastly, the calculated atomic percentage needs to be converted into weight percentage. This conversion is carried out using Equation 3.2.

3.1.5 AMD

One of the issues with dividing the segregation map into smaller areas (i.e. meshing) is that the final segregation map is sensitive to the mesh size. To combat this in the current study, the optimal mesh size has been determined by calculating a quantity referred to as the AMD using a simple algorithm. In this algorithm, the difference between the area fraction of the phase of interest in an element with its nearby elements is first calculated using a specified kernel. The kernel in this case is a square matrix centering around an element. The area fraction in each element is calculated by counting the number of pixels of the desired phase and then dividing by the total number of non-black pixels (Eq 3.5).

$$f_i^e = \frac{n_i^e}{n_{tot}^e - n_{bk}^e} \tag{3.5}$$

where f_i^e is the area fraction of the desired phase i in an element e, n^e is the number of pixels in an element e, where subscripts i, bk and tot indicate the pixels of the desired phase, black pixels and the total number of pixels, respectively.

The maximum difference of each element with its neighbours is then determined by calculating the difference of the area fraction of each element with its adjacent

elements (Eq 3.6) and selecting the maximum value (Eq 3.7).

$$D_i^e = |f_i^e - Ar_{f_i}^{ker_e}| \tag{3.6}$$

$$MD_i^e = max(D_i^e) \tag{3.7}$$

where D_i^e is an array of the difference values for an element e, $Ar_{f_i}^{ker_e}$ is an array containing the area fractions for all the elements in the kernel centering around an element e, and MD_i^e is the maximum difference of an element e.

Figure 3.3 shows an element and its adjacent elements with three different kernels superimposed on them. A kernel with a width smaller than the mesh size will only capture the element itself. On the other hand a kernel with a width larger or equal to the mesh size will capture three or more elements. In this research, a kernel with a width of 1.2 times the mesh size has been chosen. This is the smallest kernel that captures all the adjacent elements, while ensuring that only the adjacent elements are picked. Applying this process to the entire image, the maximum differences of each element and its neighbours are calculated. These maximum differences represent how sharply the area fraction is changing with respect to the neighbouring cells. By calculating the average of these values over the whole image, a single value, called the AMD, representing the overall change in the gradient can be calculated (Eq 3.8). This process can be repeated for different tessellations. The optimal mesh size to evaluate the spatial gradient of a sample is achieved when the calculated AMD is a minimum (Eq 3.9).

$$AMD_i^h = \sum_{e=1}^{N_h} MD_i^e / N_h \tag{3.8}$$

$$h_{opt} = x \ni (AMD_i^x = min(AMD_i^h)|_{h=h_l}^{h_f}) \tag{3.9}$$

where N_h is the number of elements in the mesh with spacing h, and AMD_i^h is the

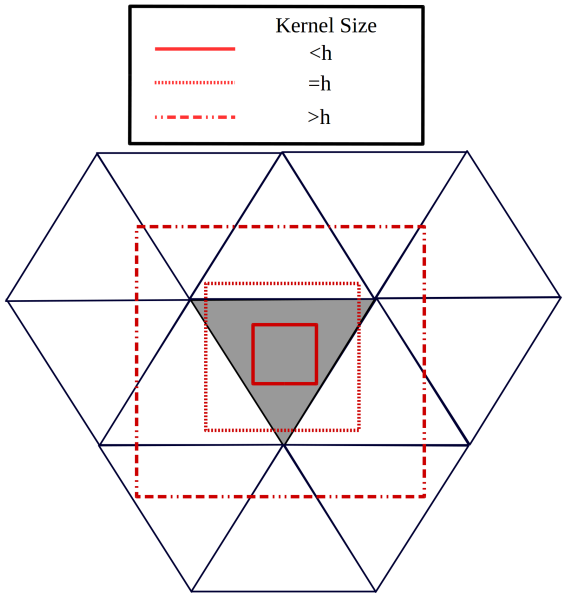

Figure 3.3: An element with its neighbouring elements. Red boxes indicate the kernels overlaid on the mesh with three different sizes, where h indicates the mesh size.

Average Maximum Difference of mesh with spacing h. The subscripts opt, l and f for h, indicate the optimal mesh size, the lower bound for mesh size and the higher bound mesh size for AMD analysis.

3.2 Methodology verification

Before applying the segregation characterization methodology to microstructural samples, a series of verification operations were performed to test and verify the individual steps of the methodology.

3.2.1 Image segmentation verification

Prior to selecting the Otsu thresholding method (explained in section 3.1.2) for segmentation, it was compared to two other techniques in an effort to determine the applicability and efficacy of these techniques. The factors considered in the comparison were accuracy and execution time. The two other segmentation methods considered in this evaluation were:

- **K-means:** a simple unsupervised learning algorithm that can be applied to solve the clustering problem. Given a number of clusters k known a priori, the algorithm defines k centroids, one for each cluster. In the next step, each point in the data set is associated to the nearest centroid. At this point, the centroids are recalculated as the centers of the clusters resulting from the previous step. These steps are then iterated until the sum of distances of each point from their centroids is minimized [75].

  In the case of segmentation of the microstructure, three clusters were defined; pores, primary phase and secondary phase. K-means was then applied to cluster different pixel grey-scale values into these segments.

- **Gaussian Mixture Models (GMM):** data is clustered by assigning the data points to a number of normal distributions. This method assumes that the data consists of several normally distributed components and strives to identify these groupings [76].

  Similar to previous case, three clusters were defined in order to segment the images into pores, primary and secondary phases.

Khajeh in his work on permeability, fabricated a series of Al-Cu alloys with varying Cu contents [77]. In order to characterize the microstructure, Khajeh performed high resolution XMT scans of his samples. In the current research, this data was reconstructed and utilized to calibrate the image segmentation stage. This data was chosen first, due to the similarity of Al-Cu and Al-Si microstructure and second, due to the fact that the composition of the analyzed alloys were known.

The compositions of the alloys are summarized in Table 3.1 and sample XMT section images are shown in Figure 3.4.

Figure 3.5 shows a sample XMT microstructure segmented using the three different clustering methods. As can be seen, the visual quality of the segmentation for

Table 3.1: The details of the alloys used in Khajeh's research [77]

Alloy name	wt% Al	wt% Cu
E01	93.7	6.3
E02	92.8	7.2
E03	91.5	8.5
E04	86.5	13.5

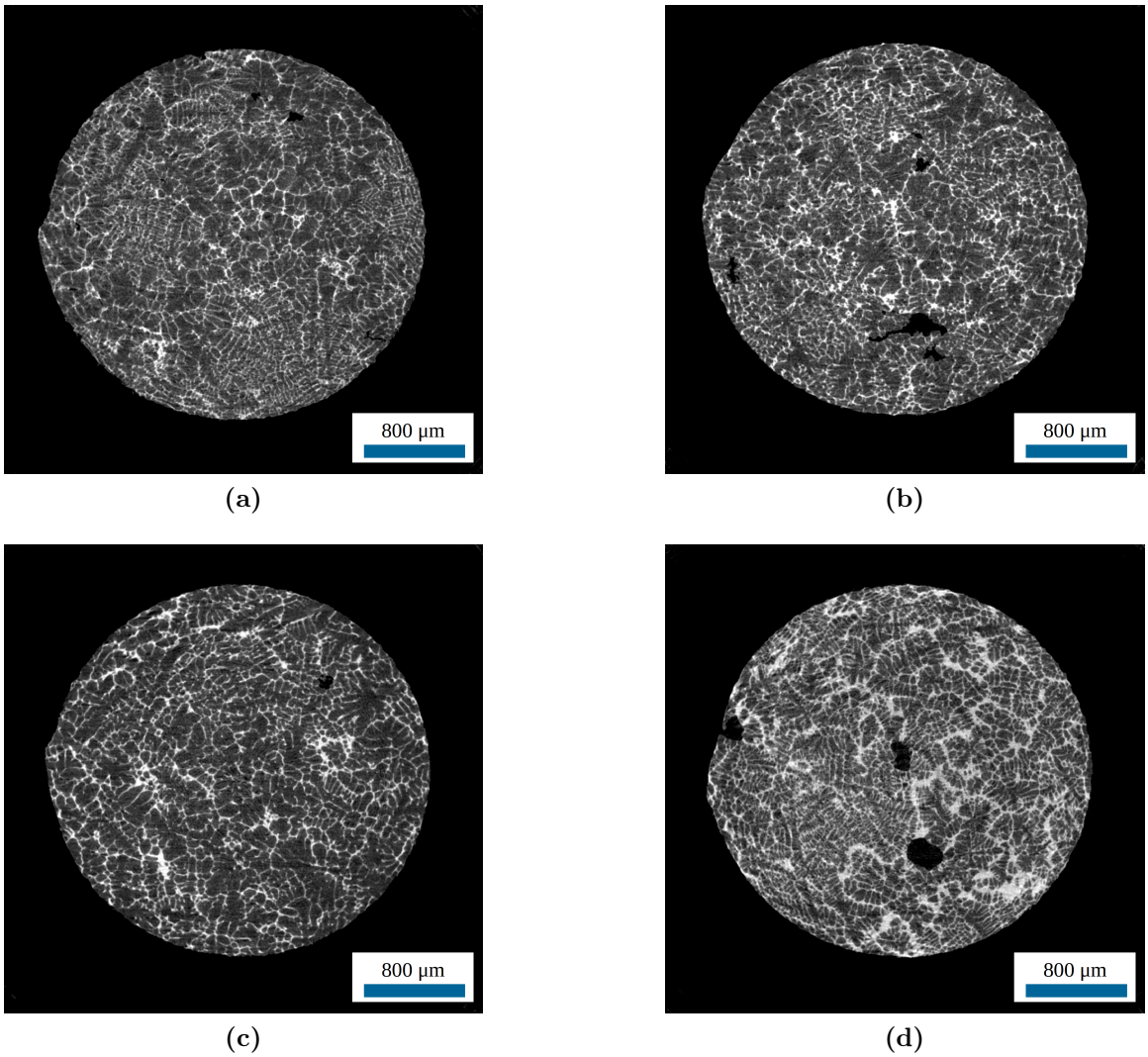

(a) **(b)** **(c)** **(d)**

Figure 3.4: Sample XMT section images of alloys fabricated by Khajeh, E01 (a), E02 (b), E03 (c) and E04 (d) [77].

all three cases is comparable to the original image. However, there are subtle differences between each segmentation. For this microstructure, Otsu thresholding slightly overestimates the size of the eutectic. The K-means result identifies pores that are slightly larger and generates some black noise (visible on the segmented image). From a visual point of view, GMM method seems to slightly underestimate the amount of the eutectic phase.

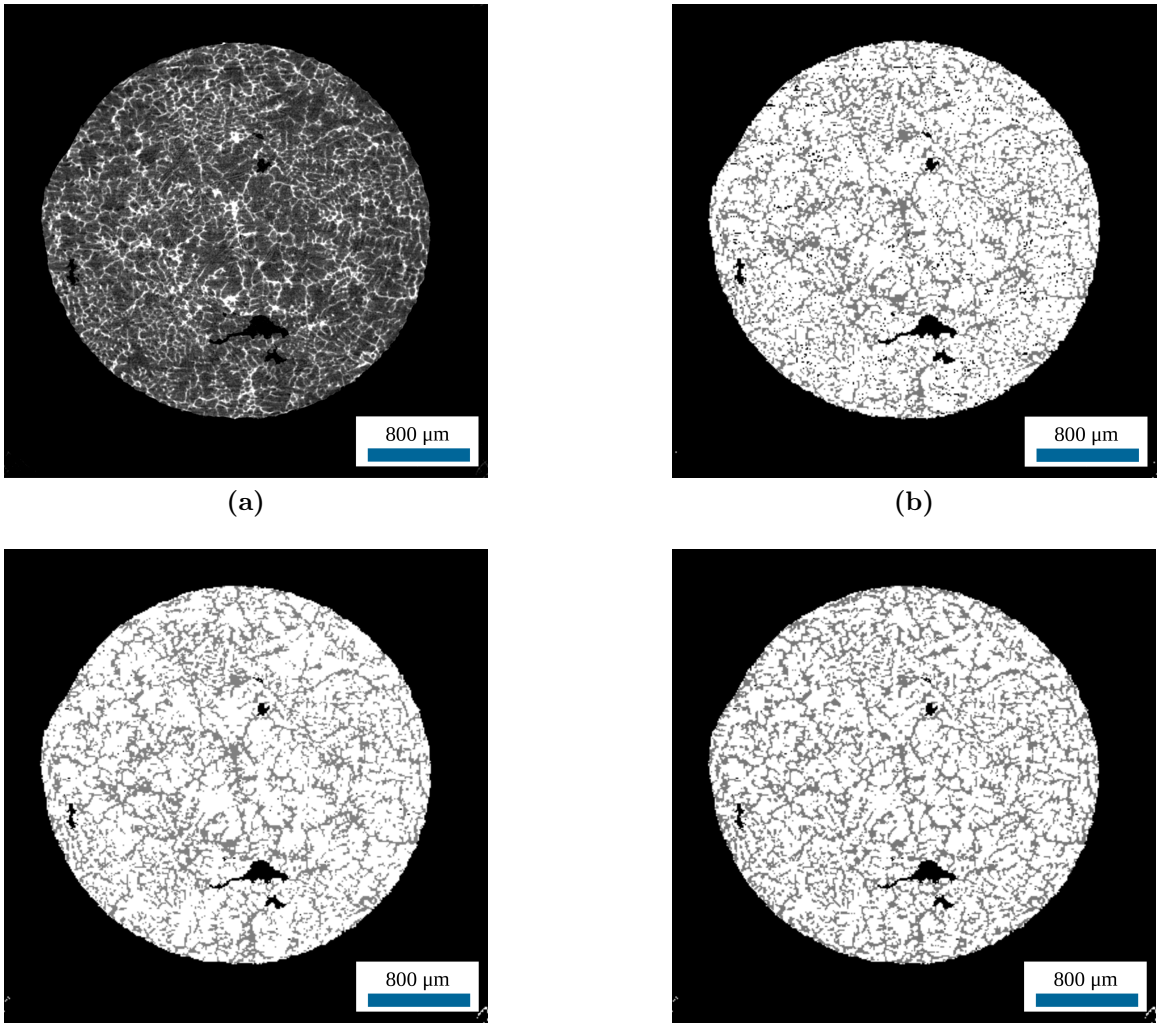

(a) **(b)** **(c)** **(d)**

Figure 3.5: A sample XMT image (a) and the respective segmented images using the (b) K-means, (c) GMM and (d) Otsu techniques.

These methods were applied to more than 8000 images available from the XMT

scans. The area fraction data, which is in the form of eutectic area fraction due to the image magnification, were then converted to Cu mass fraction using the technique described in section 3.1.4. Figure 3.6 shows the summarized results for these cases. As can be seen, overall, the measured values are reasonably close to the actual composition values.

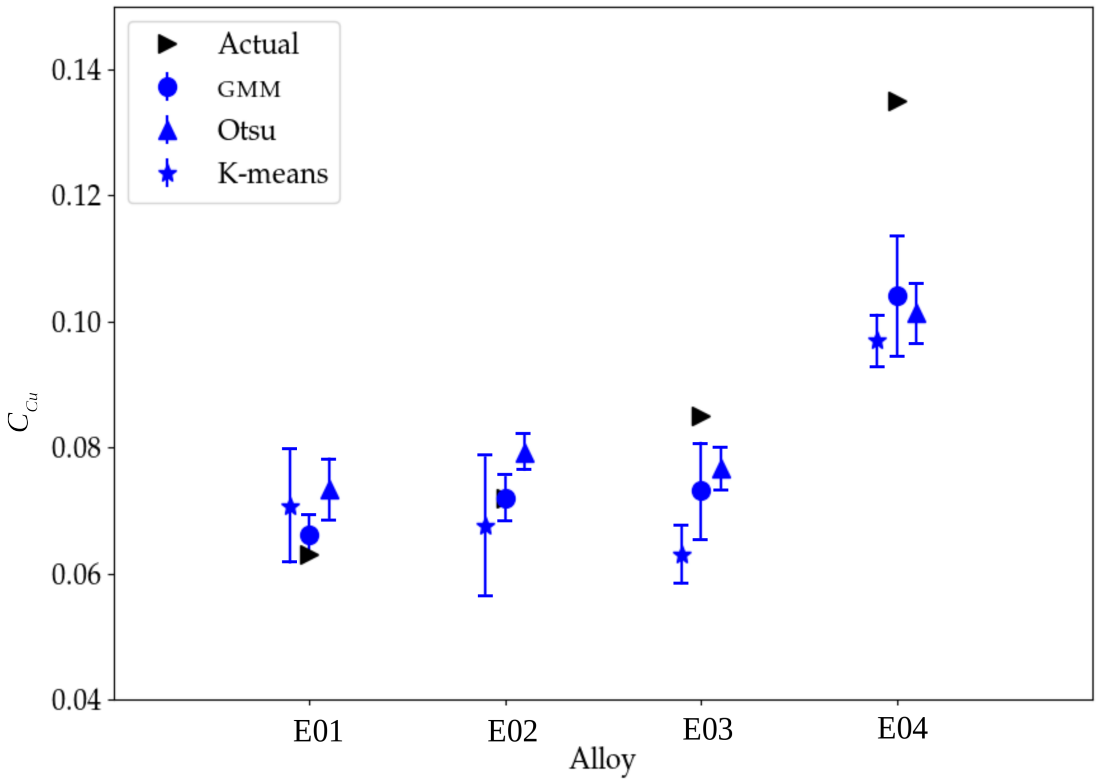

Figure 3.6: Measured vs. actual copper mass fraction values from K-means, GMM and Otsu thresholding for alloys E01-04.

The average absolute error for each method and the execution time per sample are summarized in Table 3.2. The data gives a quantitative comparison of the three methods. The average error for the GMM segmentation is below 10%, where K-means results are on average 18% different from the actual composition values. The execution time for K-means is the highest, followed by GMM. This is due to the fact that these methods utilize high-cost optimization algorithms to segment the images.

Table 3.2: Comparison of the three image segmentation methods based on accuracy and execution time (based on an i7 CPU with 16Gb of RAM).

Alloy name	Average error [%]	Execution time per sample [s]
K-means	18.56	4.12
GMM	9.63	2.88
Otsu thresholding	13.38	0.10

Otsu thresholding, on the other hand, uses a less costly optimization algorithm and results in an order of magnitude difference in execution time. This is especially useful in the case where a large dataset of several thousand images is being segmented. Due to reasonable accuracy and low execution time, Otsu thresholding was chosen for use in the remainder of this work to segment the images for macrosegregation analysis.

3.2.2 Meshing validation

Two meshing techniques were compared to truss based meshing (explained in section 3.1.3). The techniques were evaluated based on mesh accuracy. The following is a short description of the meshing techniques:

- **Simple triangulation:** was performed by first populating the shape with mesh points in a grid and then utilize Delaunay triangulation to generate the mesh. This method is easily applied for convex shapes, since Delaunay triangulation generates only convex geometries [73]. For the case of concave geometries, the triangles outside the geometry need to be identified and discarded. The removal of triangles outside the geometry results in topology errors.

- **Rectangular mesh:** is similar to simple triangulation, where the geometry is populated with mesh points. However, instead of utilizing Delaunay triangulation, the mesh is generated using rectangular patches. It should be noted that, convex and concave geometries are treated similar to the previous method.

A comparison analysis was carried out on two geometries, shown in Figure 3.7, using 10, 20 and 50 pixel (px) mesh sizes.

(a) **(b)**

Figure 3.7: Geometries for mesh comparison analysis.

Figure 3.8 shows the results of applying the three meshing techniques based on three mesh sizes for the image shown in Figure 3.7a. Table 3.3 shows the accuracy of the generated meshes. Accuracy in this case is defined as the error in calculated area shown in Eq. 3.10.

$$accuracy = (1 - \frac{area_{original} - area_{mesh}}{area_{original}}) \times 100 \tag{3.10}$$

Table 3.4 summarizes the execution time for each mesh shown in Figure 3.8. Despite having low execution times, the rectangular mesh approach fails to capture the boundary of the geometry even at small mesh sizes. This would result in inaccurate predictions in future steps. Triangular meshing, on the other hand, captures the boundaries more accurately. However, the elements adjacent to the boundary exhibit large aspect ratios. The Truss based method captures the boundary well, especially

for small mesh sizes. This method, however, due to its iterative nature takes much longer time to process.

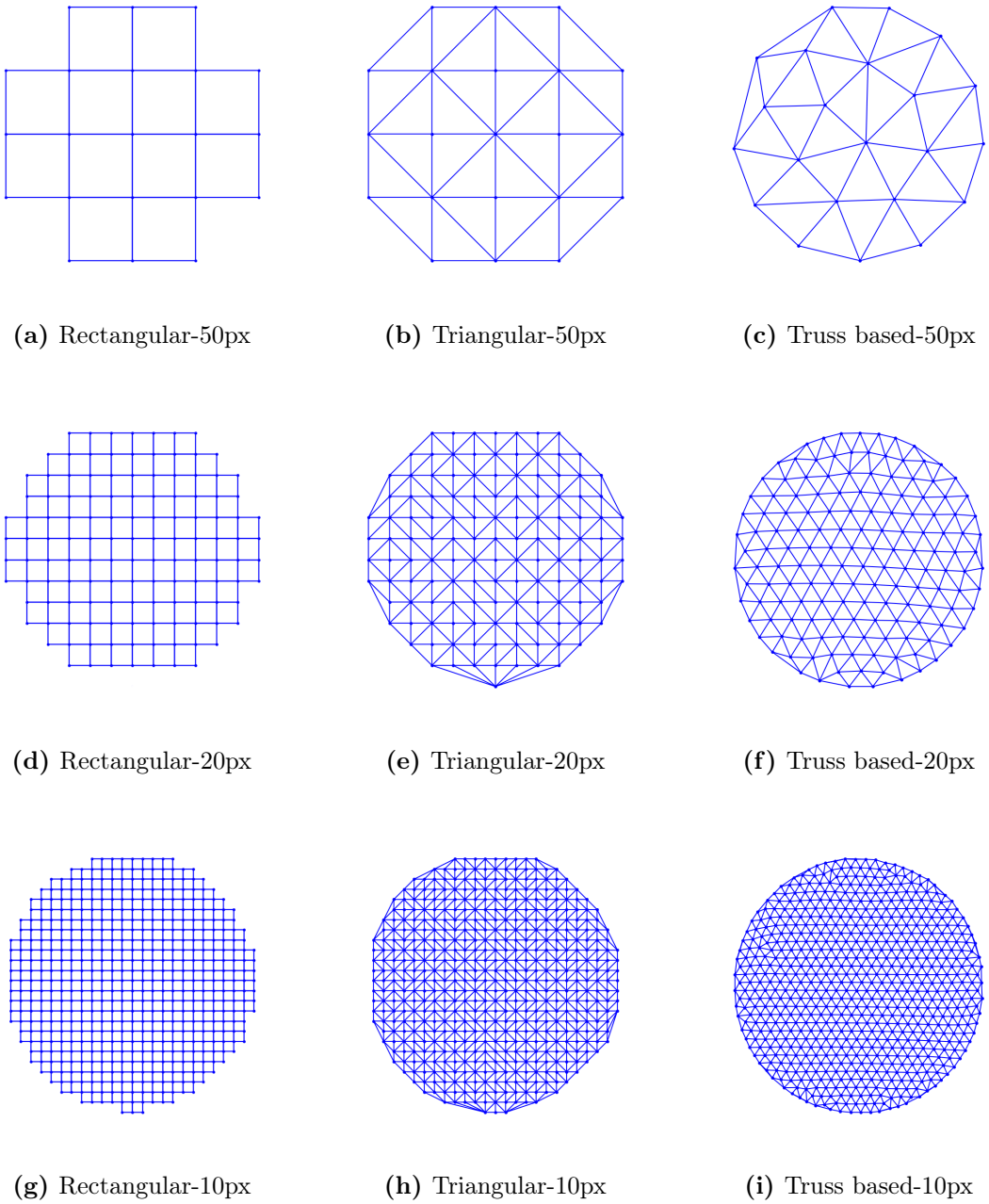

(a) Rectangular-50px **(b)** Triangular-50px **(c)** Truss based-50px

(d) Rectangular-20px **(e)** Triangular-20px **(f)** Truss based-20px

(g) Rectangular-10px **(h)** Triangular-10px **(i)** Truss based-10px

Figure 3.8: Mesh comparison for Figure 3.7a, with meshing technique and mesh size indicated under each image.

Figure 3.9 shows the results from the three meshing techniques based on three

Table 3.3: Accuracy of meshes presented in Figure 3.8.

Mesh size	Rectangular	Triangular	Truss based
50px	58.39%	68.28%	94.69%
20px	80.98%	89.54%	99.03%
10px	90.13%	94.61%	99.73%

Table 3.4: Execution time (based on an i7 CPU with 16Gb of RAM) for meshes presented in Figure 3.8.

Mesh size	Rectangular	Triangular	Truss based
50px	0.114 s	0.113 s	0.433 s
20px	0.433 s	0.122 s	4.442 s
10px	0.998 s	0.130 s	12.610 s

mesh sizes applied to a more complex shape, shown in Figure 3.7b. Table 3.5 shows the accuracy of the generated meshes. Table 3.6 summarizes the execution time for generating respective meshes. Analyzing the results of these meshing techniques applied to a more complex shape further highlights the inefficiency of the rectangular mesh technique. The issues with this technique are readily apparent for larger mesh sizes, as the mesh is broken into two shapes. Although the triangular meshing technique was able to adequately capture the boundaries of the more complex region, the elements adjacent to the boundary are misshaped. The truss based method, despite its high execution time, captures the boundaries very well and exhibits a nearly uniform element structure. Due to the considerable differences in accuracy of the three meshing methods and the need to prioritize accuracy over execution time, the Truss based method has been applied in the follow-on analysis in this thesis to mesh the cross-sectional geometry for macrosegregation analysis.

3.2.3 AMD validation

In order to assess the AMD technique, a series of carefully designed, artificial microstructure images were generated and analyzed using the AMD method. To con-

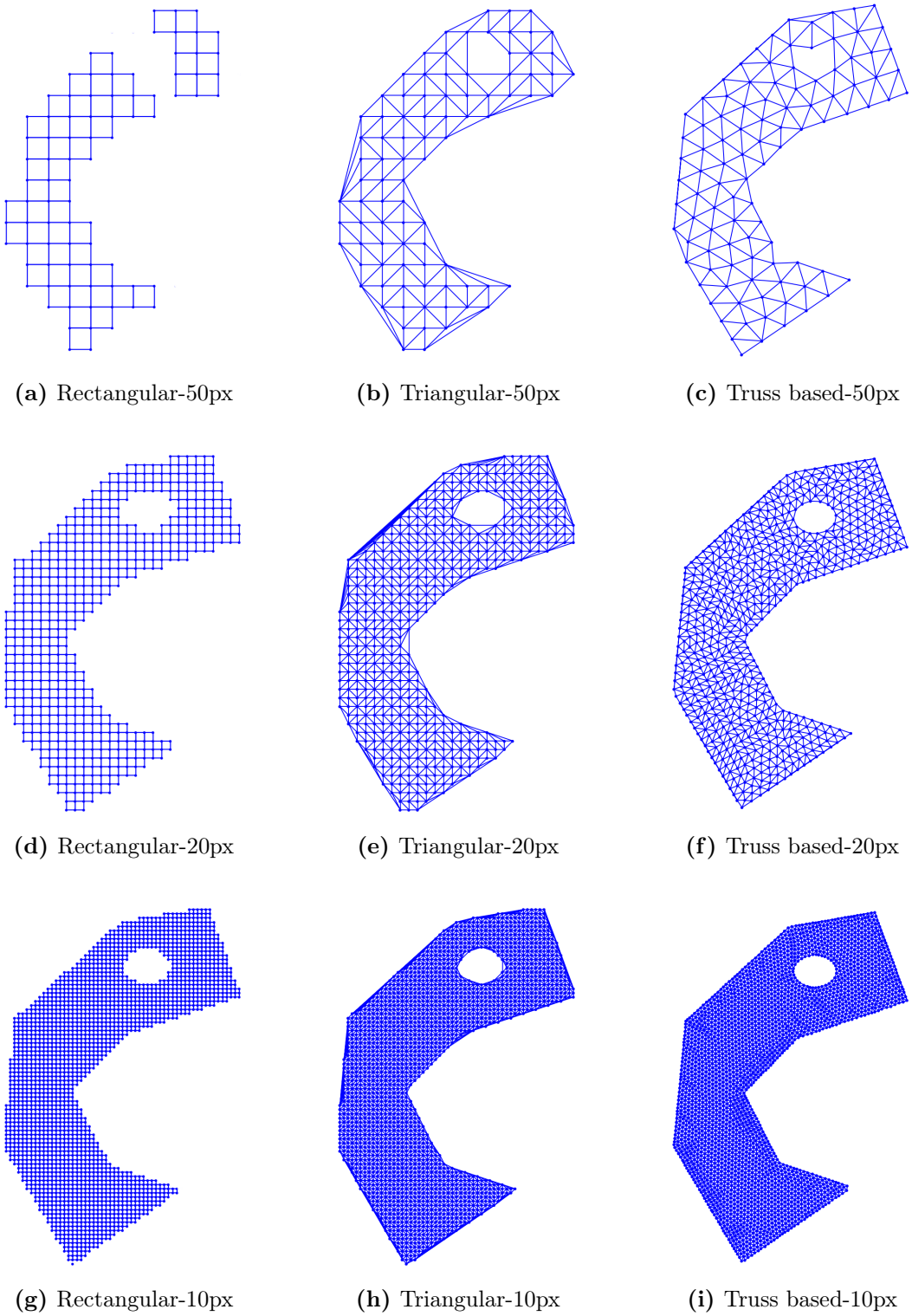

(a) Rectangular-50px **(b)** Triangular-50px **(c)** Truss based-50px

(d) Rectangular-20px **(e)** Triangular-20px **(f)** Truss based-20px

(g) Rectangular-10px **(h)** Triangular-10px **(i)** Truss based-10px

Figure 3.9: Mesh comparison for Figure 3.7b, with meshing technique and mesh size indicated under each image.

Table 3.5: Accuracy of meshes presented in Figure 3.9.

Mesh size	Rectangular	Triangular	Truss based
50px	57.06%	84.45%	98.72%
20px	81.64%	93.67%	99.83%
10px	90.93%	97.73%	99.89%

Table 3.6: Execution time (based on an i7 CPU with 16Gb of RAM) for meshes presented in Figure 3.9.

Mesh size	Rectangular	Triangular	Truss based
50px	0.230 s	0.163 s	1.958 s
20px	0.847 s	0.164 s	5.441 s
10px	2.227 s	0.174 s	57.908 s

struct images with the area fraction changing in 1D, a python code was used to generate a number of thin rectangular images with constant area fraction. This was done by first initializing the matrix of values representing the image section with zeros and then populating the matrix with ones at random positions until the ratio of the number of ones to the total number of pixels met the criteria of the desired area fraction. The rectangular regions were then joined together to create a square region with a known gradient in area fraction. The same method has been used to create images with 2D area fraction variations. However, instead of stacking rectangular matrices, a series of co-centric squares with different sizes, each having a constant area fraction were stacked on top of each other.

The generated images, shown in Figure 3.10, have a range of phase area fractions between 0.05 and 0.15. Figure 3.10a has a negative to positive 1D phase area fraction gradient, where the area fraction first decreases and then increases with distance from the top edge. Figure 3.10b has a constant positive 2D area fraction gradient, where the area fraction increases moving toward the center of the image. Figure 3.10c has a positive to negative 2D area fraction gradient, where the area fraction first increases

and then decreases moving towards the center. Figures 3.10d-3.10f show schematic images of the variation in area fraction in each image, where black represent the high area fraction and white represent the low area fraction.

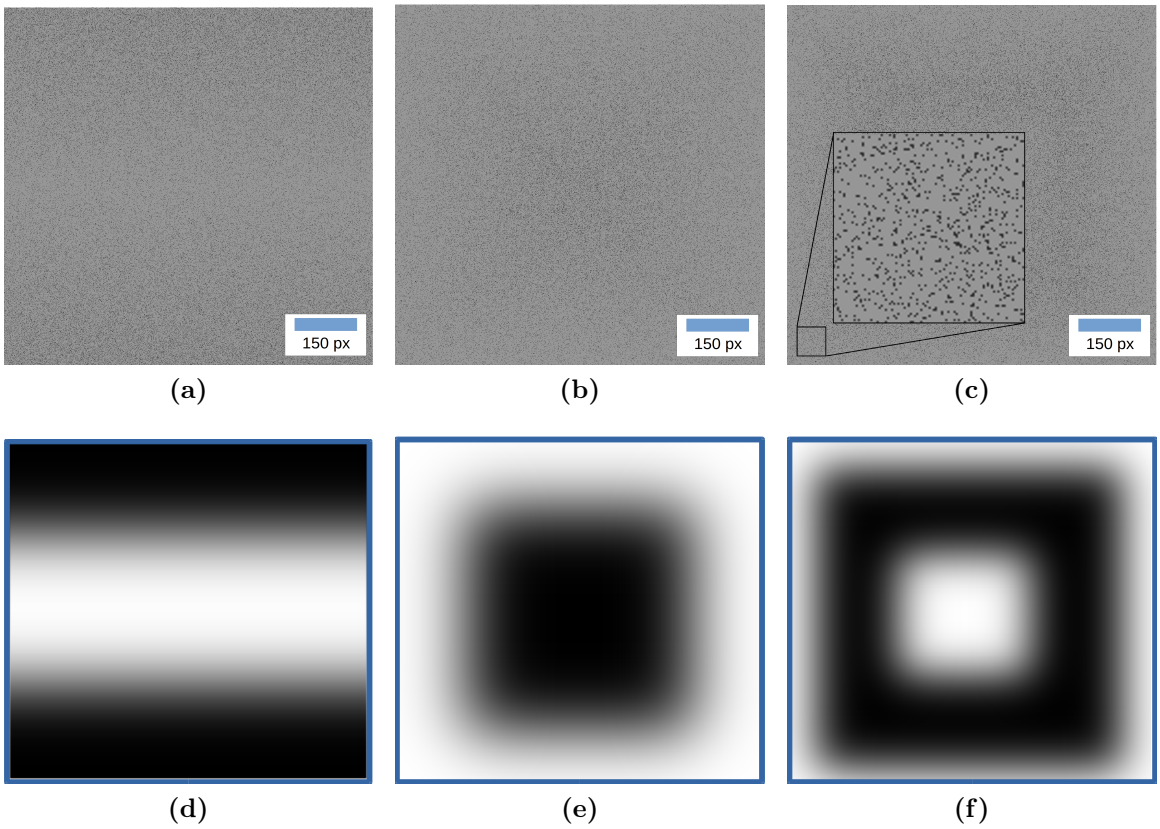

Figure 3.10: Artificial microstructure images generated for AMD analysis with (a) 1D decreasing-increasing area fraction, (b) 2D increasing area fraction and (c) 2D increasing-decreasing area fractions.(d)-(f) schematic representation of the intended gradient for (a)-(c), respectively. Where black represents high area fraction (0.15) and white represent low area fraction (0.05).

Figure 3.11 shows the variation of the AMD values calculated for the test images as a function of the mesh size, the contour images of the area fraction of the artificial phase, and the calculated phase area fraction as a function of the position along a vertical line bisecting the images. The mesh dependency of the AMD value exhibits an initial decrease with increasing mesh size before transitioning to increase with

increasing mesh size. However, a minimum is visible in each plot, which indicates an optimal mesh size for each microstructure. This is consistent with the discussion presented in the methodology, where it was suggested that the segregation gradient would be less accurately calculated when a non-optimal mesh size is used. The optimal mesh size was found to be 41, 41 and 32 pixels for the test images shown in Figure 3.10a to 3.10c, respectively.

In order to evaluate whether the mesh size reasonably represents the gradient, the phase area fraction values, extracted along a vertical line bisecting the contour image, have been compared with the actual area fraction values in the generated microstructures (refer to Figures 3.11g-3.11i). The calculated gradient using the optimal mesh size closely matches the intended gradient. It should be noted that the calculated gradient was observed to deviate from the actual value when non-optimal mesh sizes were used. Moreover, from the contour plots shown in Figures 3.11d-3.11f, the intended variations of 1D decreasing-increasing, 2D increasing and 2D increasing-decreasing are detectable. This assessment using artificial microstructures suggests that the proposed method and the AMD value are useful for determining the optimal mesh size for visualizing segregation.

3.3 Summary

Overall a method was developed to visualize segregation in eutectic alloys using an image montage. This method utilizes a tessellation technique to mesh the image, then calculates the mass fraction of the desired phase in each element. The current method uses a continuous map of micrographs to calculate segregation map which results in more accurate results, where previous methods used discrete number of samples in order to do so. The following conclusions can be drawn from this study:

- Three image segmentation methods were compared based on accuracy and execution time to segment eutectic micrographs. The Otsu method was found to

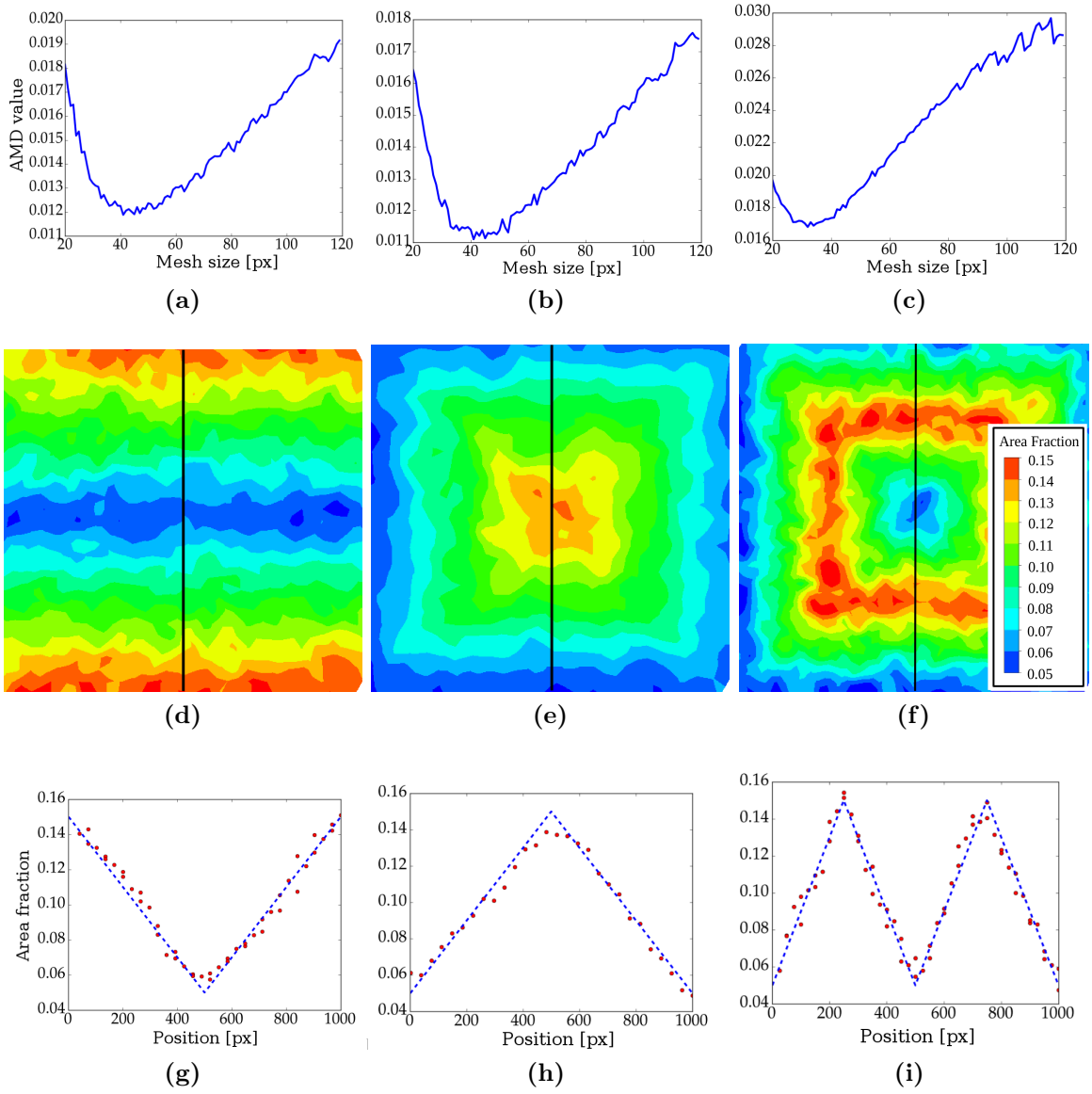

Figure 3.11: AMD curves (a) to (c), respective contour plots (d) to (f) and gradient comparison curves (g) to (i) for test images shown in Figure 3.10. Where dashed blue lines in figures (g) to (i) show the intended area fraction and red circles show the calculated area fraction.

be more efficient in segmenting these type of images.

- A method was developed to convert area fraction of the secondary/eutectic phase to mass fraction of the alloying element in eutectic alloys.

- Three meshing techniques were developed and compared based on accuracy and execution time. A Truss based method was found to be more suitable for this research as it exhibits much higher accuracy in comparison to the other techniques.

- A method called AMD has been developed to determine an optimal mesh size for calculating the segregation map. Results presented in this study illustrate the validity of this method for a set of artificial designed microstructures.

Chapter 4

Macrosegregation in Shape Castings[1]

A series of dumbbell shaped castings with different sizes and cooling conditions were produced with the intent of either exaggerating or limiting shrinkage-induced macrosegregation. This shape was selected to enable variable cooling rates on sections of the casting to cause bulk motion of enriched liquid via compensatory flow. The following sections are dedicated to explain in detail the experimental procedure and the respective results for macrosegregation in shape castings.

4.1 Experimental methodology

A dumbbell-shaped casting geometry was selected for this work because it was hypothesized that, by controlling the cooling condition on the neck of the casting, one can produce or eliminate macrosegregation caused by shrinkage induced flows. For example, if it were possible to pause solidification / cooling when the neck section is solidified halfway through, the remaining liquid in the neck would be enriched in solute. This is due to microsegregation which was explained in detail in section 1.1. If this liquid were then pulled into the bottom volume due to compensatory flow, after full solidification, the bottom volume of the casting would be enriched and the top

[1]Portions of this chapter have been published in:

- *Khadivinassab H.*, Maijer D. M., Cockcroft S. L.,"Characterization of Macrosegregation in Eutectic Alloys", Materials Charcterization, (2017)
- *Khadivinassab H.*, Fan P., Reilly C., Yao L., Maijer D. M., Cockcroft S. L., Phillion A. B.,"Study of the macro-scale solute redistribution due to liquid metal feeding during the solidification of A356", Light Metals Production, Processing and Applications Symposium, The 53rd Annual Conference of Metallurgists, (2014)

volume would be deplete of solute.

Four variants of the experimental setup were produced for this experiment; a dumbbell-shaped mould with natural cooling condition, a dumbbell-shaped mould with an insulated neck part, a dumbbell-shaped mould with forced cooling on the neck and a large dumbbell-shaped mould with natural cooling condition. The mould geometry and cooling configuration for each of the castings are as follows:

- **Dumbbell-shaped mould with natural cooling:** The mould configuration for the standard sized dumbbell-shaped casting is shown in Figure 4.1. The mould for this casting was manufactured from standard copper fittings (1.5mm wall thickness). An end cap with a 7mm wall thickness was fabricated for the bottom of the casting to promote directional solidification from the bottom to the top. The overall height of the mould is 163mm with outer diameters of 54, 32 and 54mm for the top, middle and bottom sections, respectively. Five type-K thermocouples were embedded in the casting at different axial locations to monitor the temperature.

- **Dumbbell-shaped mould with insulated joint:** The mould and insulation configuration are illustrated in Figure 4.2 for this casting. The mould used for the dumbbell-shaped mould with natural cooling was reused with insulation on the central joint. A piece of 15mm thick fibreglass blanket was wrapped around the central joint of the mould and held in place with steel sheet (1mm thick). Similar to the previous case, 5 type-K thermocouples were embedded in the casting at different axial locations to monitor the temperature.

- **Dumbbell-shaped mould with forced cooling on the neck:** The mould and cooling configuration for this casting are shown in Figure 4.3. The base mould for the dumbbell-shaped casting was reused with changes to the central joint cooling configuration. Forced air cooling was applied to the central joint

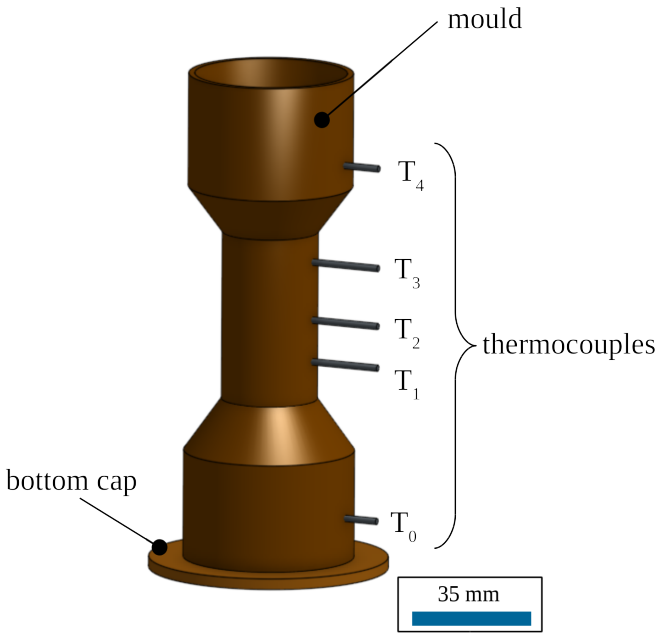

Figure 4.1: Geometry of dumbbell-shaped casting with natural cooling condition.

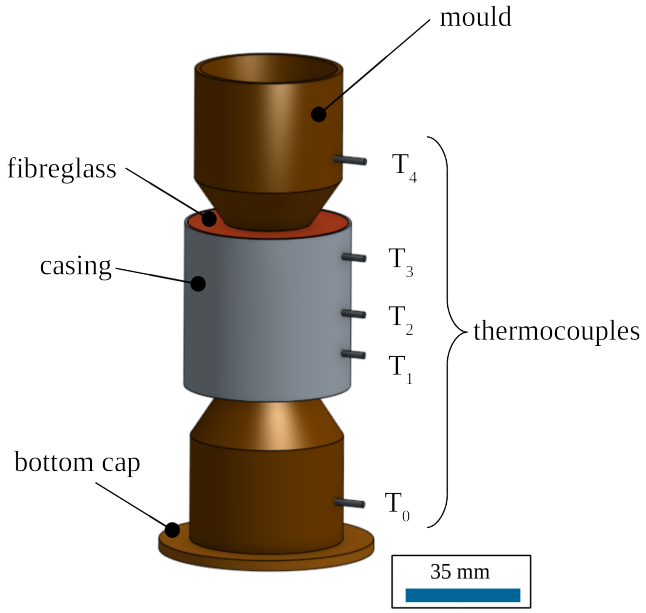

Figure 4.2: Geometry of dumbbell-shaped mould with insulated central joint.

using compressed air. To ensure that cooling was applied only to the central joint, a steel plate assembly was designed and manufactured to shield the top and bottom sections of the mould. Similar to the previous cases 5 type-K thermocouples were embedded in the casting at different axial locations to monitor the temperature. It should be noted that although the nozzle is directed towards one side of the mould, the cooling is still expected to be symmetrical. This is due to the high thermal conductivity of the thin copper mould allowing the heat to be extracted uniformly.

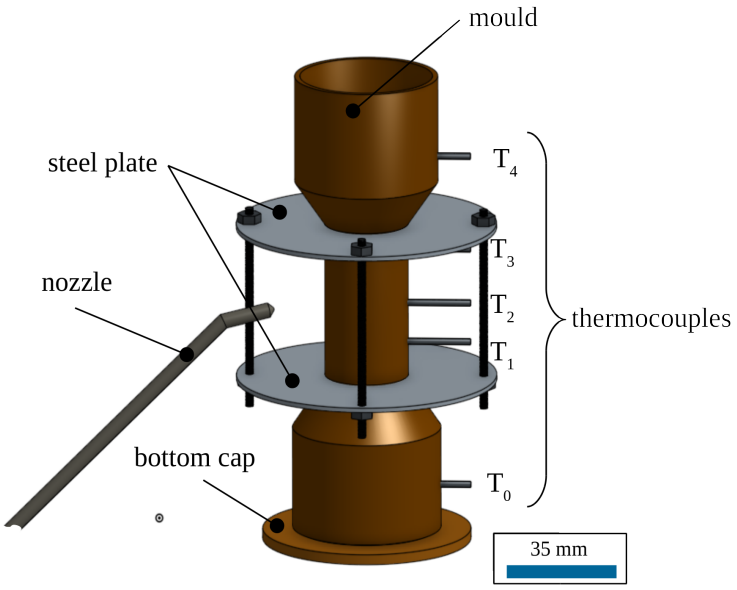

Figure 4.3: Geometry of dumbbell-shaped mould with forced cooling on the central joint.

Since the air flow is applied from one specific direction, the variation of the heat transfer coefficient around the periphery of the joint section and the resulting cross-sectional cooling conditions were assess to determine if axisymmetric conditions occurred. Figure 4.4 shows the distribution of local Nusselt number around a cylinder for forced air cooling conditions [85].

Considering an air flow rate of 30 m/s and a kinematic viscosity for air equal to 50×10^{-6} m^2/s, the Reynolds number of the air flow is 30000. According to

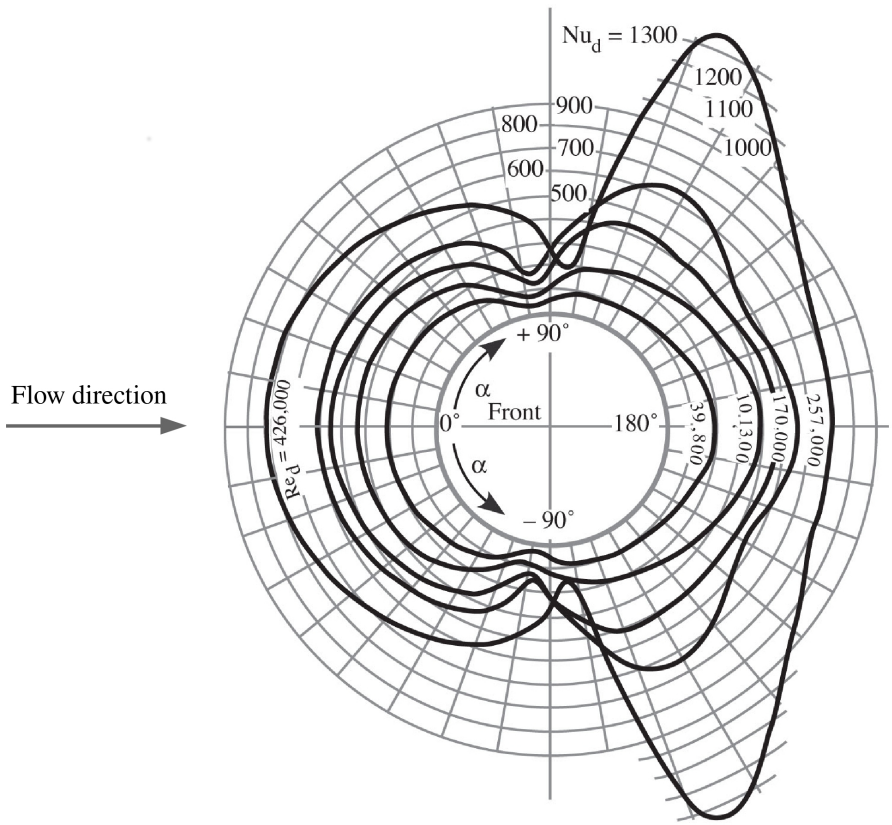

Figure 4.4: Distribution of local heat transfer coefficient around a circular cylinder for flow of air [85].

figure 4.4, this Reynolds number results in a maximum Nusselt number of 120. Equation 4.1 shows the relationship between the Nusselt number and the heat transfer coefficient.

$$\text{HTC} = \frac{Nu \times k}{L} \tag{4.1}$$

where Nu is Nusselt number, k is thermal conductivity and L is the characteristic length. Using a characteristic length of 0.05 m (the diameter of the joint section) and thermal conductivity of air at high temperatures (0.0515 W/mK) in equation 4.1, the maximum heat transfer coefficient is calculated to be 121.65 W/m^2K.

Biot number (shown in 4.2) gives a simple index of the ratio of the heat transfer

resistances inside of and at the surface of a body. This ratio determines whether or not the temperatures inside a body will vary significantly in space, while the body heats or cools over time, from a thermal gradient applied to its surface. For Biot numbers below 0.1 the heat conduction inside the body is much faster than the heat convection away from its surface, and temperature gradients are negligible inside of it.

$$Bi = \frac{L \times \text{HTC}}{k} \tag{4.2}$$

Using the diameter of the joint section as characteristic length, 121.65 W/m^2K as HTC and the thermal conductivity of liquid aluminum at liquidus temperature (75 W/mK), the Biot number is calculated to be 0.08. As this number is below 0.1, heat transfer variations around the periphery of the cylinder can be neglected.

- **Large dumbbell-shaped mould with natural cooling:** The mould for the large dumbbell-shaped casting is shown in Figure 4.5. This mould was manufactured from large copper fittings with thicker gauge thickness (2.5 mm wall thickness). An end cap with increased wall thickness (13mm) was fabricated for the bottom of the casting to promote directional solidification from the bottom to the top. The overall height of the mould is 260mm with outer diameters of 110, 74 and 110mm for the top, middle and bottom sections, respectively. Seven type-K thermocouples were embedded in the casting at different axial locations to monitor the temperature.

Prior to instrumentation and casting, the moulds were cut in half and reattached using several hose clamps in order to facilitate extraction of the castings after cooling. The castings were hand-poured using unmodified A356 (introduced in section 1.3) melted in a resistance furnace. Prior to pouring each casting, the melt was degassed to

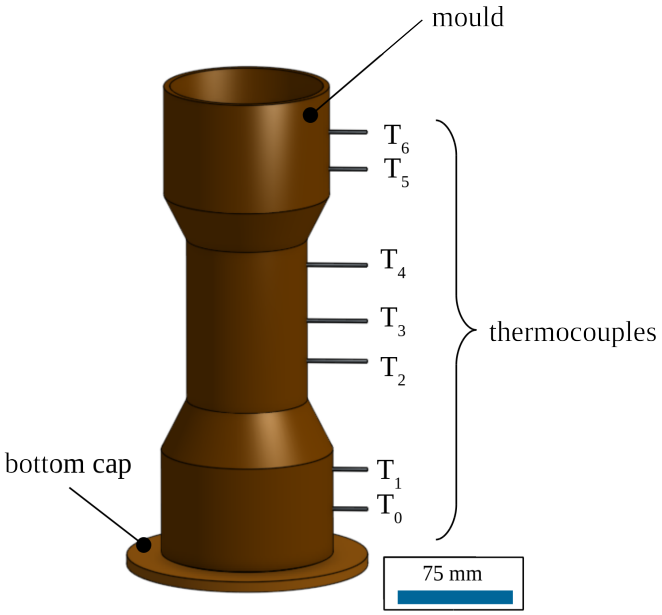

Figure 4.5: Geometry of large dumbbell-shaped mould with natural cooling condition.

reduce the hydrogen content by bubbling Ar gas through the melt for 20min. During the degas procedure and prior to pouring, the melt was allowed to cool in the crucible until the temperature reached $680°C$. The moulds were at room temperature ($24°C$) when the castings were poured. After pouring, the castings were allowed to cool until fully solidified. The temperatures were recorded at 2Hz using a Data Acquisition system (DAQ) connected to a computer running the LabVIEW software [2] .

After extracting the castings from the mould, they were cut into thinner sections (shown in Figure 4.6 to be polished and analyzed. The cross-section was assumed to be representative of the whole casting since the casting is axisymmetric. Each section was mounted in epoxy [3] to aid polishing. Samples were hand polished with 240, 320, 400, 600 and 1800 grit Si-C paper. This was followed by two secondary polishing steps with 6 and 1 μm diamond paste. The surface of each casting cross-section was then mapped using Scanning Electron Microscopy (SEM) imaging. SEM

[2]National Instruments LabVIEW
[3]System Three Cold Cure

analyses were conducted on a FEI Quanta 650 scanning electron microscope with a Burker XFlash 6|30 detector. A total of 3000 and 12000 images at 100X magnification were taken from the castings produced from the small mould and the large mould, respectively. It should be noted that, based on the assumption of axisymmetry, only half of the polished surface was imaged in this process. A python code was then used to automatically stitch the images together to create a high resolution map of half of the polished surface. This image was then mirrored to create a full section and analyzed using the method explained in chapter 3. Nevertheless, in order to assess the symmetry assumption, a full section of the casting with natural cooling was mapped and analyzed.

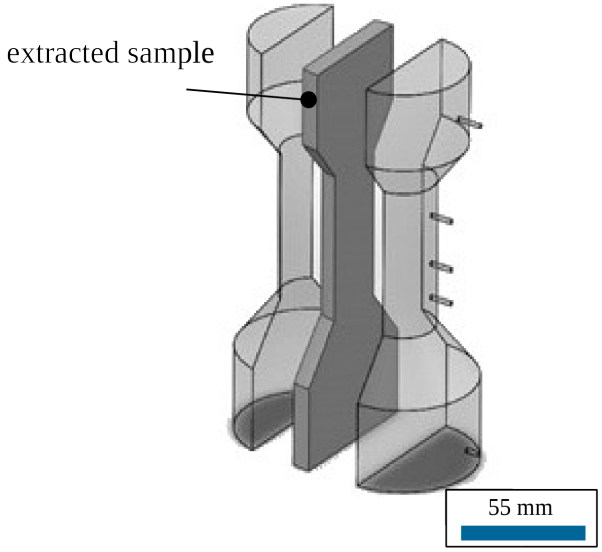

Figure 4.6: Sectioning of dumbbell-shaped castings for polishing and analysis.

4.2 Results

This section presents the results obtained from the casting and analysis of the outlined in section 4.1. For each casting, first the thermocouple results are shown, followed by a full resolution montage of the section of the casting. Results of the AMD analysis

(AMD curves) are then shown to acquire an optimum mesh size for final analysis. Finally, using the optimum mesh size the silicon segregation contour plot is shown.

4.2.1 Casting with natural cooling

The recorded thermocouple data for the dumbbell-shaped casting with natural cooling is presented in Figure 4.7. In the first 20 seconds, temperature drops rapidly because of the high heat transfer to the cold mould. As the mould heats up and primary solidification begins, the temperatures decrease with a slower rate until they reach the eutectic temperature. Depending on the cooling rate, the time at which each thermocouple reaches eutectic temperature is different. For instance, TC0, due to its proximity to the bottom plate, exhibits a larger cooling rate than the other thermocouples.

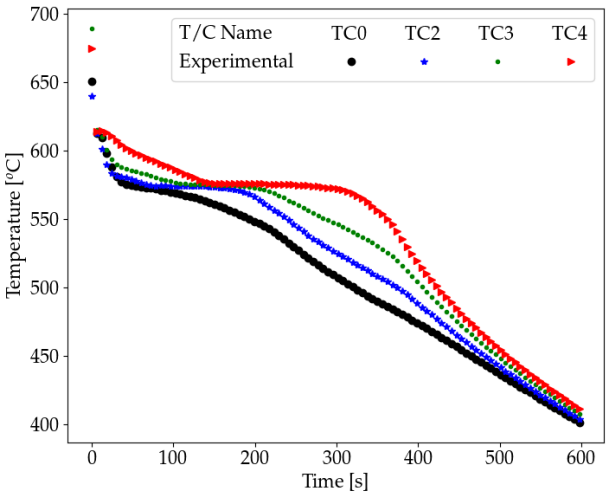

Figure 4.7: Temperature data recorded for the dumbbell-shaped casting with natural cooling.

During eutectic solidification, the rate of latent heat release increase which manifests as a plateau region in the thermocouple curves. Looking at the first 20 seconds of the solidification, TC2 cools faster than TC0 which indicates a non-directional solidification in this time interval. Afterwards the measured temperatures indicate

that solidification is directional from bottom to top. However, compositional analysis is needed to verify this finding. It should be noted that the TC1 data was discarded due to thermocouple failure.

The high resolution montage image of the microstructure in the dumbbell-shaped casting with natural cooling is presented in Figure 4.8. It should be noted that in this mapping 2cm from top and bottom of the original section was not imaged. This image has been segmented into three phases; silicon is shown in gray, α-aluminum is shown in white and pores are shown in black. Some large-scale shrinkage porosity is observed near the top of the casting (area circled in red in Figure 4.8).

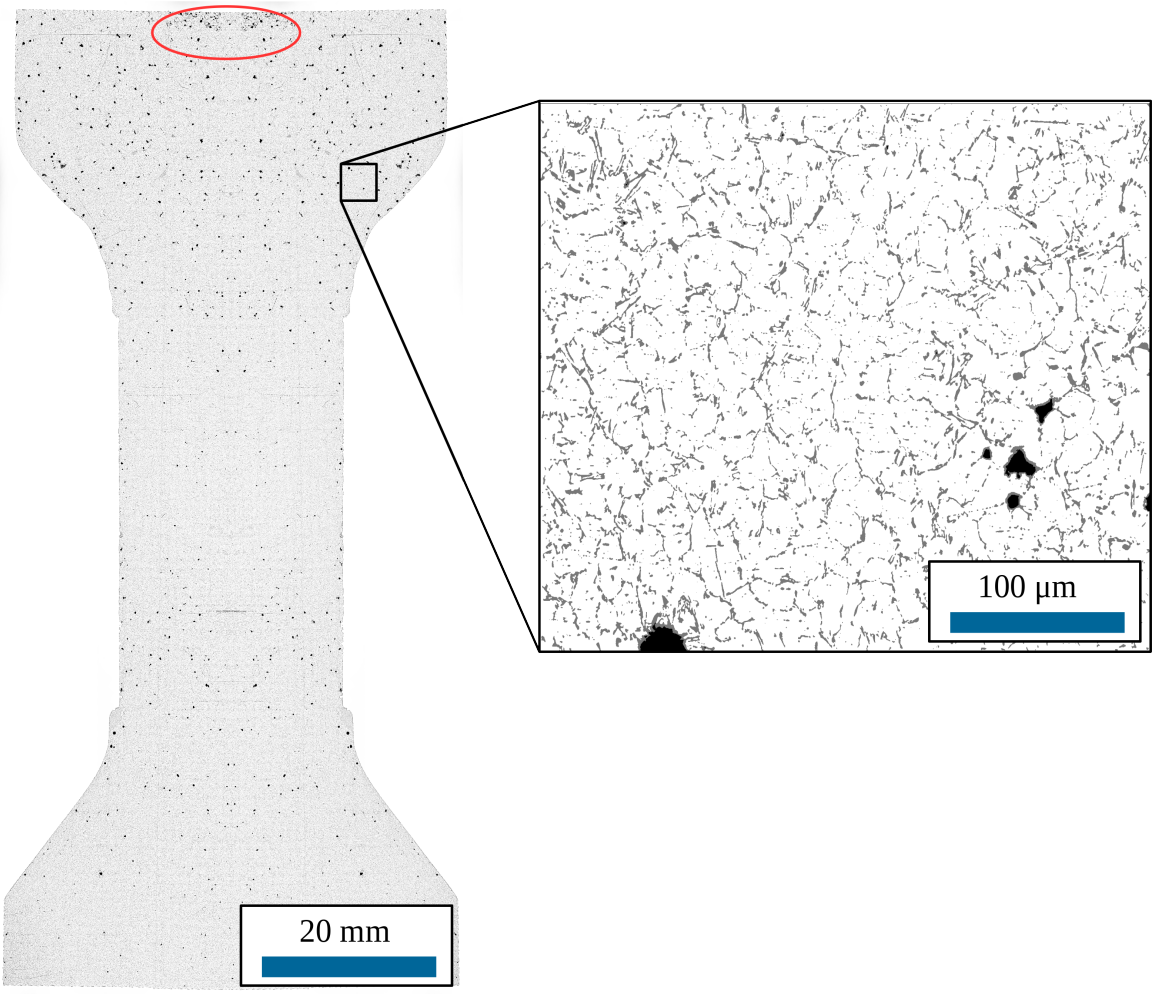

Figure 4.8: High resolution montage for the dumbbell-shaped casting with natural cooling. Red circle indices the shrinkage porosity.

Figure 4.9 shows the results of the segmentation process. As can be seen, the eutectic phase (circled in red) is segmented into its constituents. This was achieved due to the resolution of the images captured using the SEM. It should be noted that, the noise in the segmented image is due to micropores visible in the SEM image.

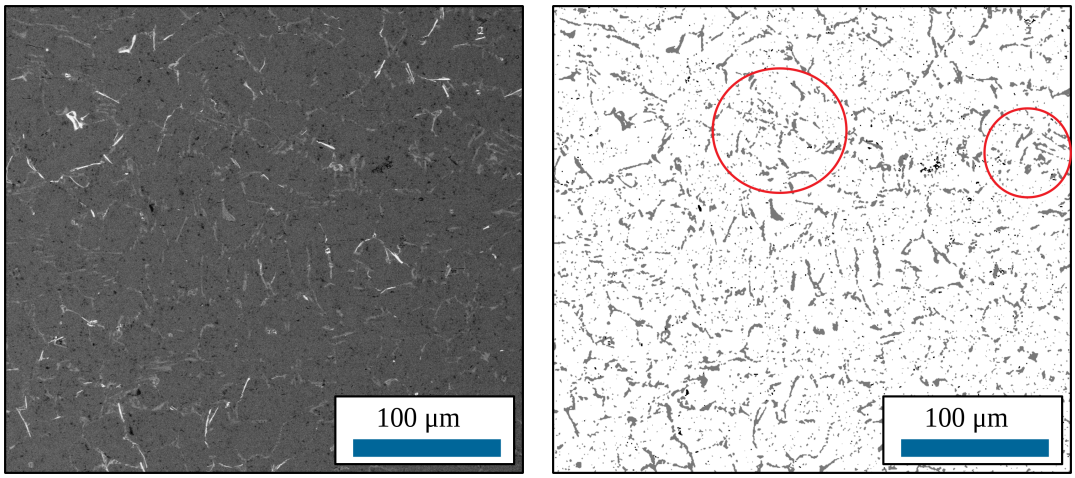

Figure 4.9: Image segmentation for microstructure images from natural cooling setup. (a) original image and (b) segmented image. Red circles indicate the eutectic phase.

The AMD analysis methodology, described in section 3.1.5, was applied to the image montage to calculate the optimal mesh size for visualization of macrosegregation. Figure 4.10 shows the AMD graph for this image. A global minimum of 1390 pixels (∼4mm) is visible from the graph. This mesh size was then used with the meshing algorithm to complete the macro-segregation visualization. Figure 4.11 shows the generated contour image of Si composition and a plot of the Si composition along the centerline of the casting. It should be noted that the nominal composition in this case is 7wt%Si because the alloy used has slightly less silicon compared to the other cases.

The contour plot shows a deplete region along the centerline of the joint section, and more enriched regions on the sides. Considering the Si composition along the centreline (refer to Figure 4.11b), the Si composition in the bottom section of the cast-

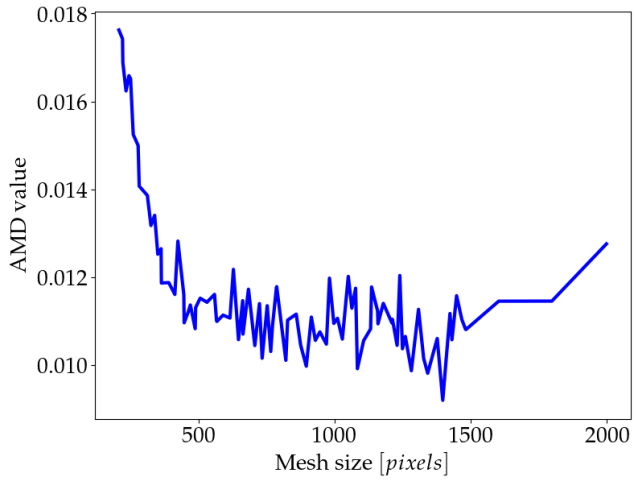

Figure 4.10: AMD curve for the dumbbell-shaped casting with natural cooling.

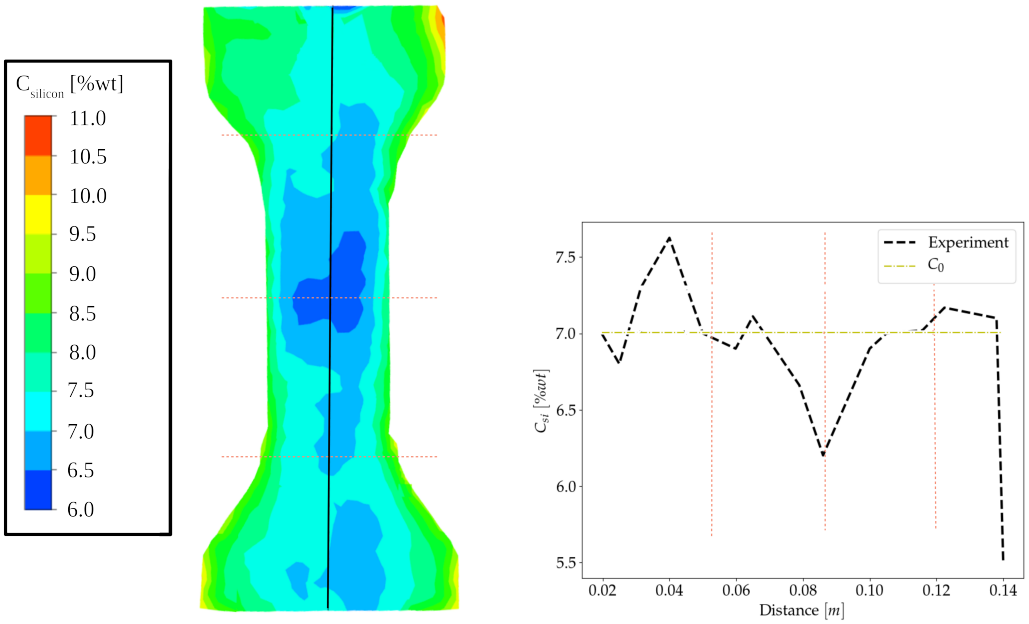

(a) **(b)**

Figure 4.11: a) Contour image of Si composition on cross-section and b) plot of Si composition along the centreline of the dumbbell-shaped casting with natural cooling.

ing decreases with distance from the bottom. In the joint section, the composition increases with distance from the bottom to slightly above the nominal composition before decreasing to below the nominal composition. Top section of the casting exhibits a highly deplete region. The enriched region at the bottom and the deplete region at the middle of the casting indicate that in fact the solidification was not directional.

The contour plot shows fairly symmetric results along the axis. Due to this symmetry, as discussed in the methodology section, only half of the cross-section will be segmented and analyzed for the next castings.

4.2.2 Casting with insulated joint

The temperature history for the dumbbell-shaped casting with the insulated joint section is shown in Figure 4.12. As can be seen, the temperature of the casting after 600s has decreased to $420°C$ compared to $405°C$ for natural cooling. Also temperature at location TC2 for the case of insulated casting drops less rapidly compared to natural cooling configuration.

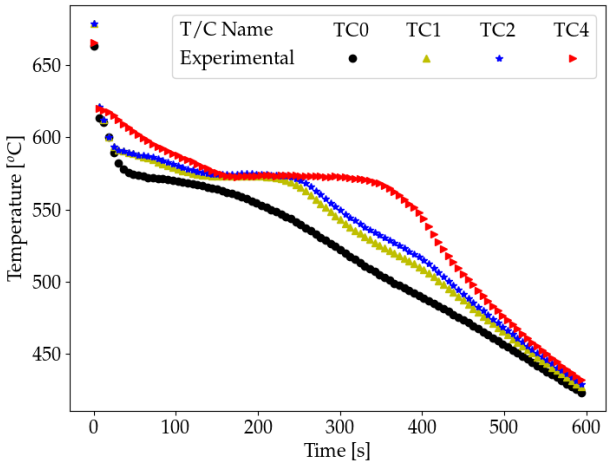

Figure 4.12: Temperature data recorded for the dumbbell-shaped casting with insulated joint.

The microstructure of the insulated casting is shown in Figure 4.13. The high

resolution montage has been segmented into three sections similar to the previous case (i.e. pores, Si and α-Al). Shrinkage porosity, visible in the top section and at the bottom of the joint section of the casting marked, has been circled in red. The shrinkage porosity at the bottom of the joint section indicates that liquid metal was encapsulated suggesting that solidification was not directional. The depth of the shrinkage porosity in the top section also indicates encapsulation. The difference in the appearance between two shrinkage porosity regions may be due to differing extents of solidification in the areas at the time of encapsulation.

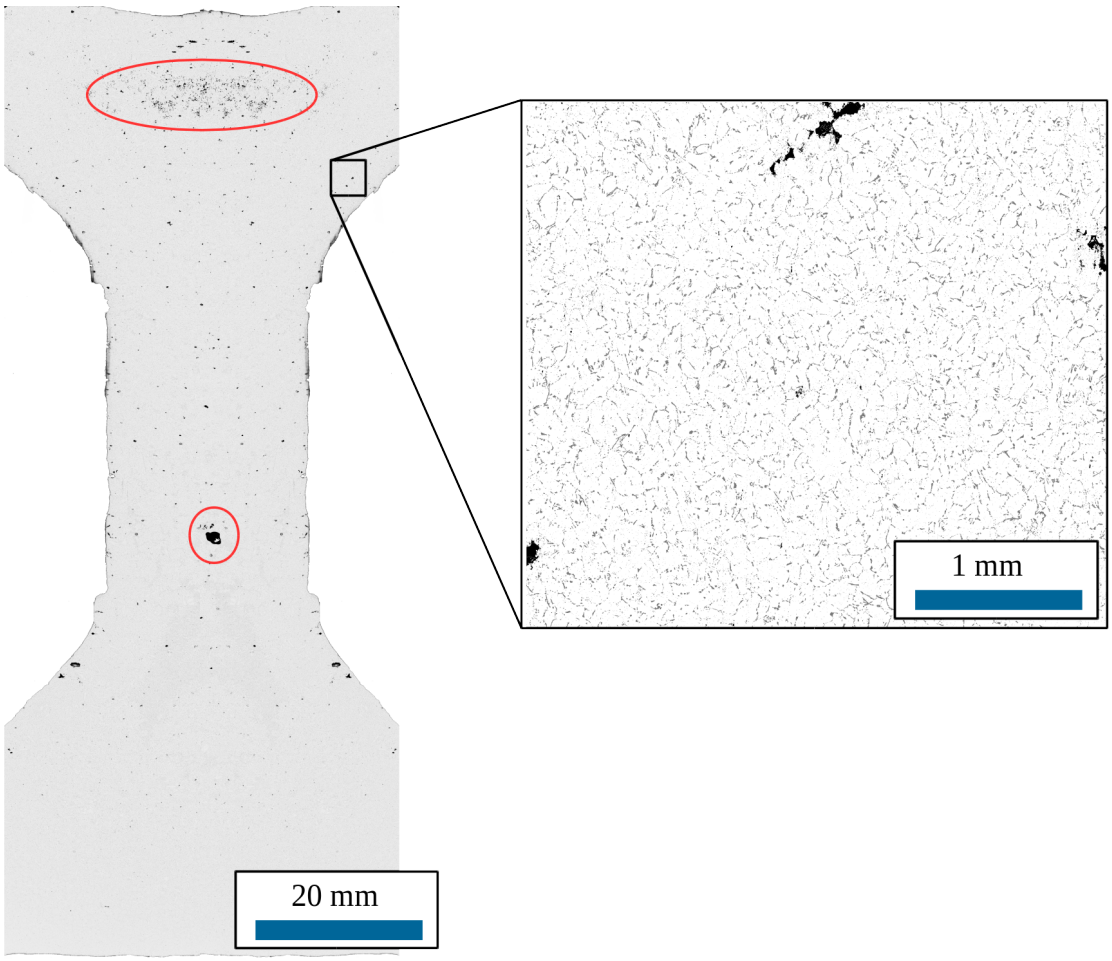

Figure 4.13: High resolution montage for the dumbbell-shaped casting with insulated joint. Red circles indicate shrinkage porosity.

Figure 4.14 shows the results of the segmentation procedure for the casting with insulated joint. As can be seen, similar to the previous case, the eutectic is segmented into primary and silicon phase.

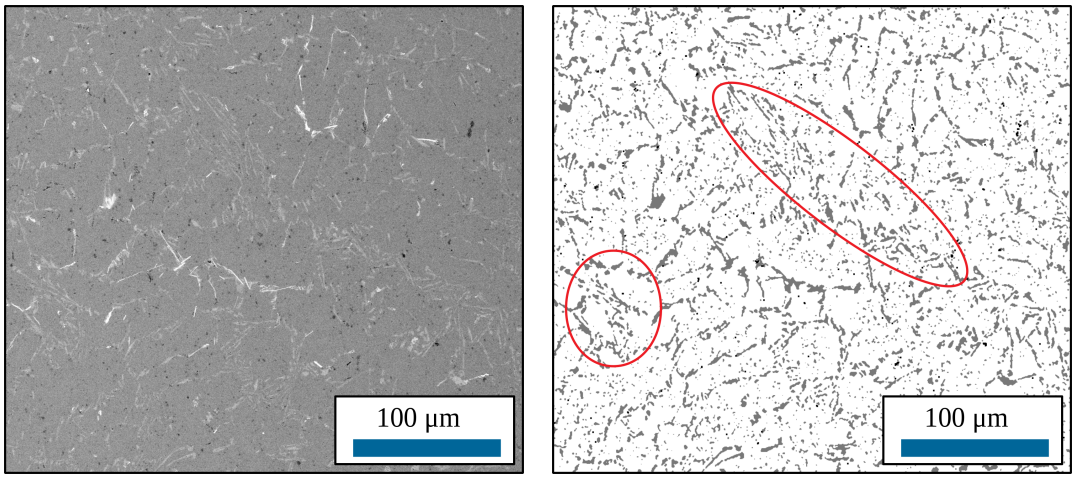

Figure 4.14: Image segmentation for microstructure images from the casting with insulated joint. (a) original image and (b) segmented image. Red circles indicate the eutectic phase.

Figure 4.15 shows the AMD curve for the image montage from this casting. The minimum lies at 1400 pixels ($\sim$ 4mm).

Figure 4.16 shows the generated macrosegregation contour plot and the plot of Si composition along the centerline of the casting. The contour plot shows an enriched region in the top part of bottom volume and a deplete region in the bottom part of the top volume. Note that unlike the case with natural cooling, there is very little radial gradient in composition in this case. Considering the plot of Si composition along the centerline, Si increases from 6wt% at the bottom to a maximum of 9.7wt% in the transition to the joint. The Si composition then decreases until the top of the joint section, where a slight increase occurs through the transition to the top volume. Similar to the previous case, there is a deplete region at the top of the casting.

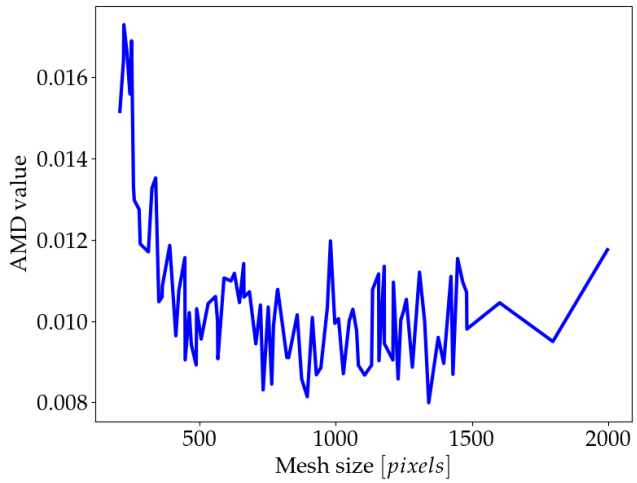

Figure 4.15: AMD curve for the dumbbell-shaped casting with insulated joint.

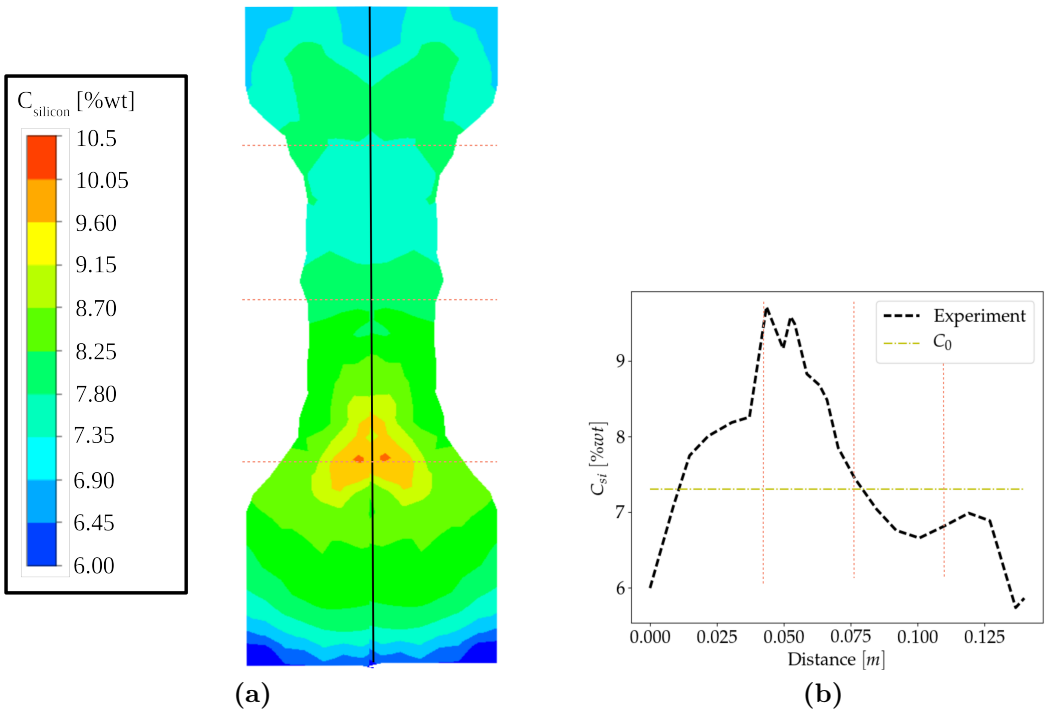

Figure 4.16: Measured macrosegregation in the dumbbell-shaped casting with insulated neck.

4.2.3 Casting with forced cooling on the joint

Figure 4.17 shows the temperatures measured in the dumbbell-shaped casting with forced cooling on the joint. The addition of cooling on the joint results in rapid cooling in this section and has lead to reduced solidification time throughout the casting (i.e. joint as well as top and bottom sections).

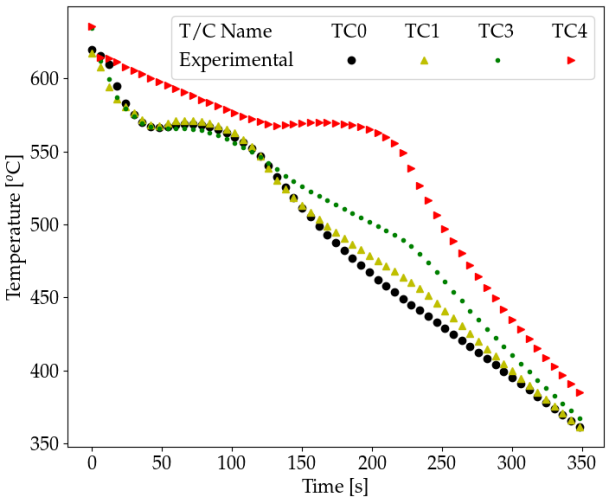

Figure 4.17: Temperatures data recorded from the dumbbell-shaped casting with forced cooling on the joint.

The high resolution montage, segmented into three sections, of the casting is shown in Figure 4.18. Significant shrinkage porosity (circled in red) is visible in the top section and in the transition from the joint to the bottom of section of the casting. Similar to the previous cases, the shrinkage porosity in the transition from the joint to the bottom section results from liquid encapsulation at that region. This confirms that solidification was not directional and is expected in this case since the joint was actively cooled. Fast cooling in the joint section would result in early encapsulation of the liquid and consequently, is the reason for the larger shrinkage porosity compared to the insulated case.

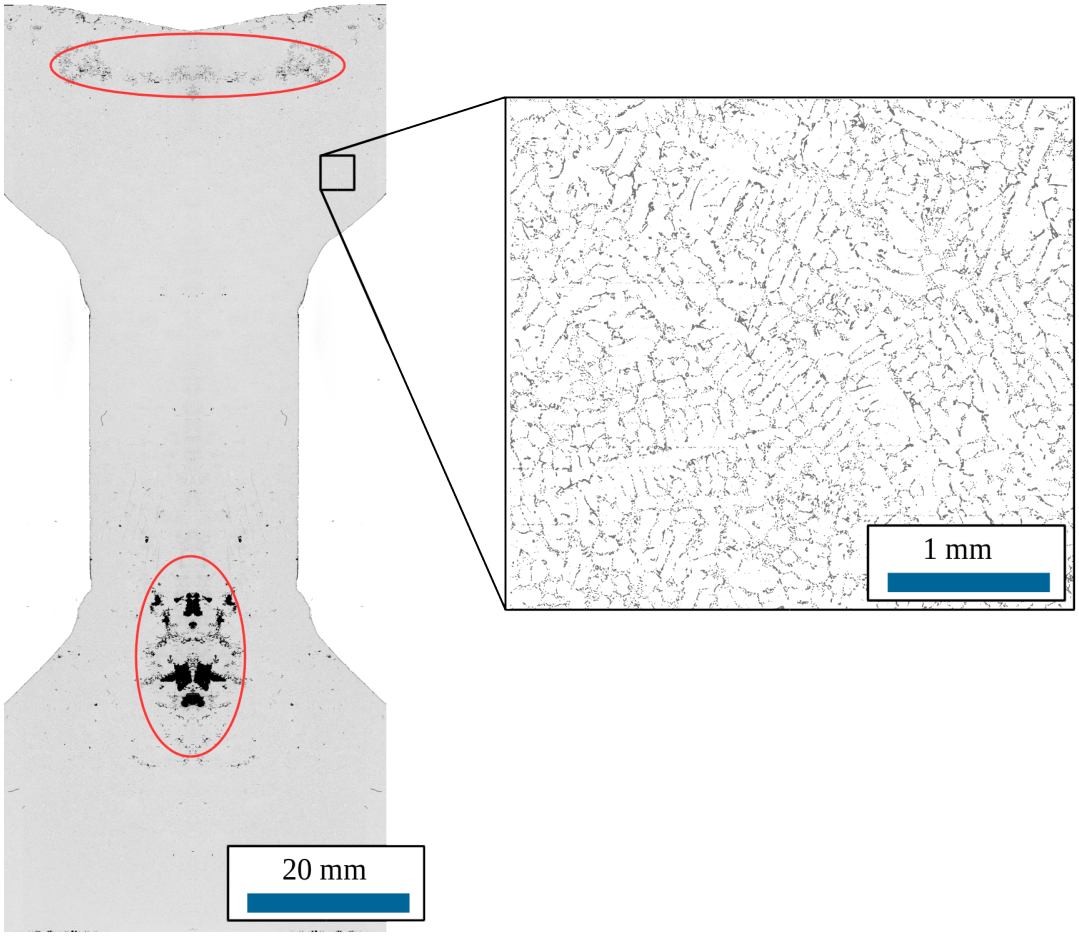

Figure 4.18: High resolution montage for the dumbbell-shaped casting with forced cooling on the joint. Red circles indicate the shrinkage porosity.

Figure 4.19 shows the result of the segmentation process taken from the section of this casting. Similar to the previous cases, the eutectic, circled in red, are segmented into primary and silicon phase, due to the resolution of the image.

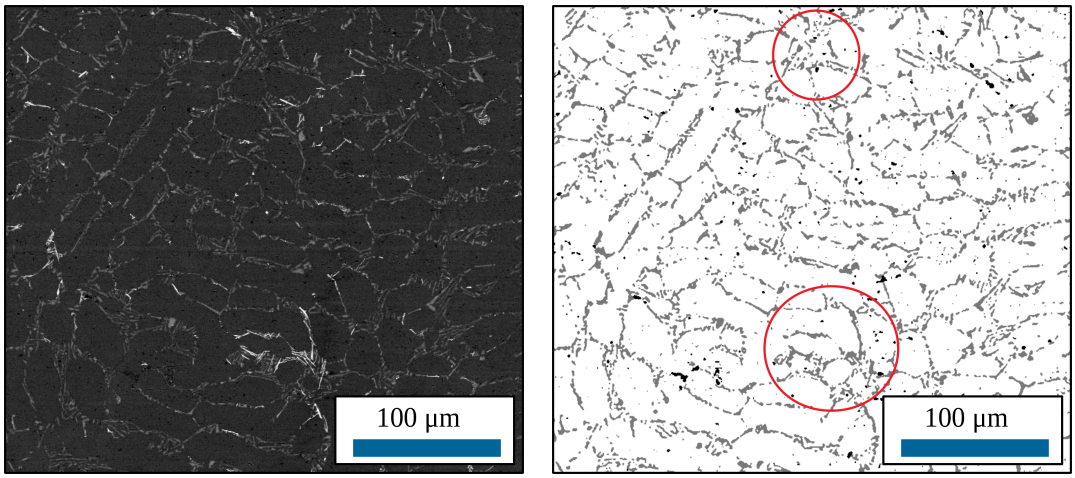

(a) **(b)**

Figure 4.19: Image segmentation for microstructure images from the casting with forced cooling on the joint. (a) original image and (b) segmented image. Red circles indicate the eutectic phase.

Figure 4.20 shows the results of the AMD analysis applied to the casting with forced cooling on the joint. It can be seen that minimum point in this case lies at 1310 pixels (∼3.5 mm).

Figure 4.21 shows the generated macrosegregation contour plot and the plot of Si composition along the centerline of the casting with forced cooling on the joint. The contour plot shows a high degree of depletion in the top part of the joint and, bottom part of the top section. Moreover, a highly enriched region is visible in the top part of the bottom volume. Looking at the centerline, from the bottom of the casting the composition increases to a maximum of 14wt%. Since this value is not realistic, the maximum value was cutoff to 12.6wt%, which is the eutectic composition. The composition then starts decreasing until the top of the joint section, where a slight increase can be seen. Similar to the previous cases above the enriched region, a deplete region can be seen.

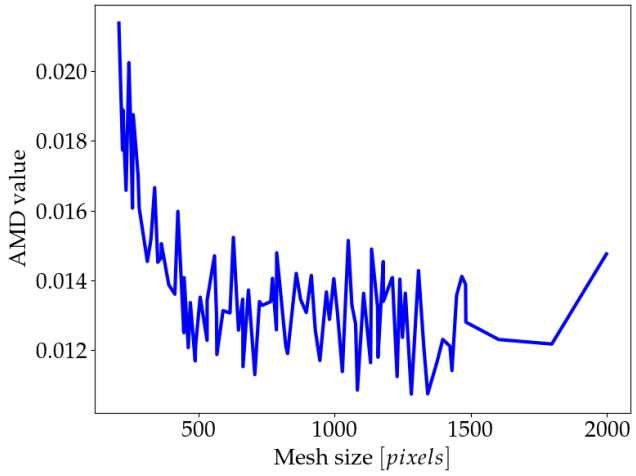

Figure 4.20: AMD curve for the dumbbell-shaped casting with forced cooling on the joint.

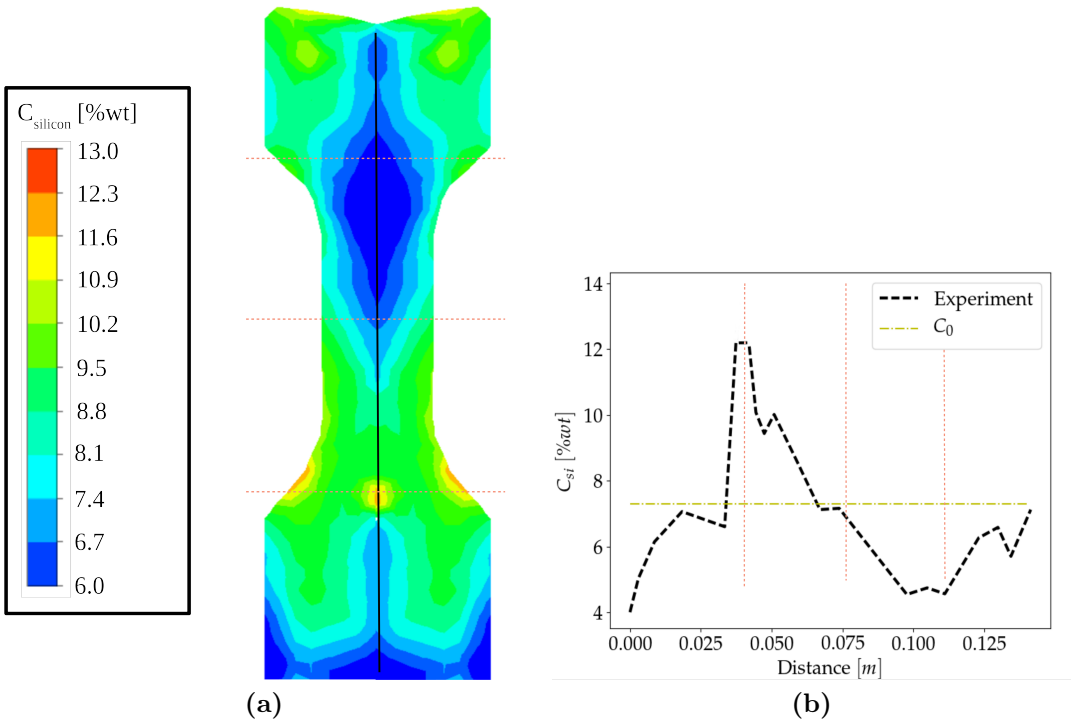

(a) **(b)**

Figure 4.21: a) Contour image of Si composition on cross-section and b) plot of Si composition along the centreline of the dumbbell-shaped casting with forced cooling on the joint.

4.2.4 Large casting

Figure 4.22 shows the temperature from the thermocouples of the large dumbbell-shaped casting. It can been seen that the solidification time has significantly increased due to the size of the casting. The temperature history suggests that the solidification conditions were directional and that there was little to no liquid encapsulation in the casting.

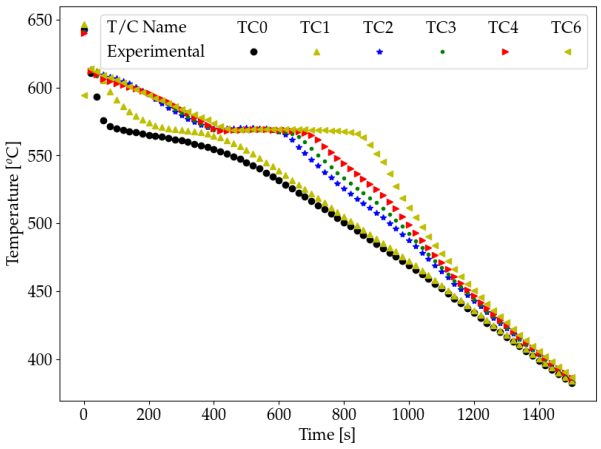

Figure 4.22: Thermocouple data from the large dumbbell-shaped casting.

Figure 4.23 shows the high-resolution montage of the section of the large dumbbell-shaped casting. Due to the large size of this section, it had to be cut into three separate sections to be polished and imaged. The acquired images were then used to create this montage. It can be seen that, unlike the previous cases, there is no shrinkage porosity visible in the cross-section of casting. However, there seems to be a higher amount of hydrogen porosity throughout the casting.

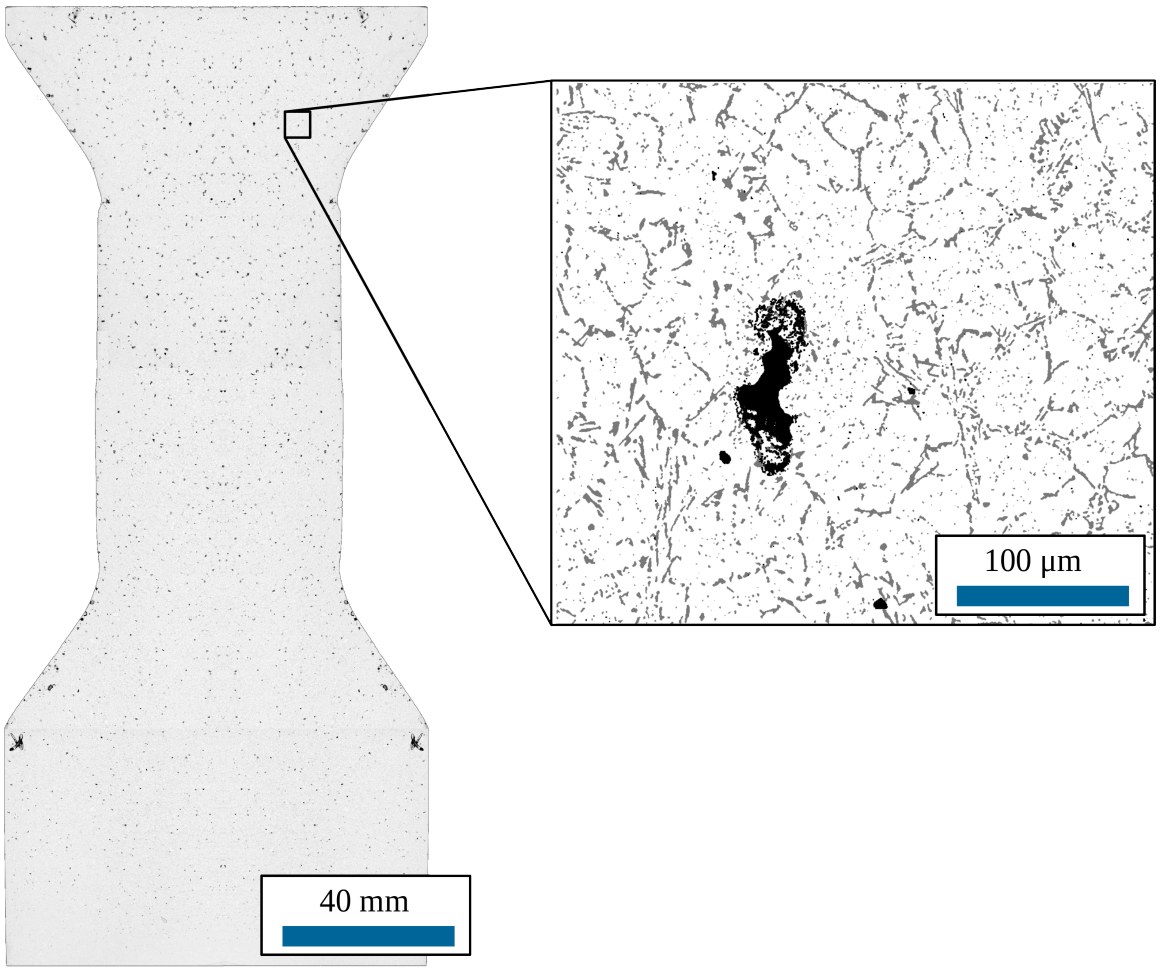

Figure 4.23: High resolution montage for the large dumbbell-shaped casting.

Figure 4.24 shows additional higher resolution imaging of the segmentation process from the section of this casting. Similar to the previous cases, the eutectic has been segmented into primary and silicon phase.

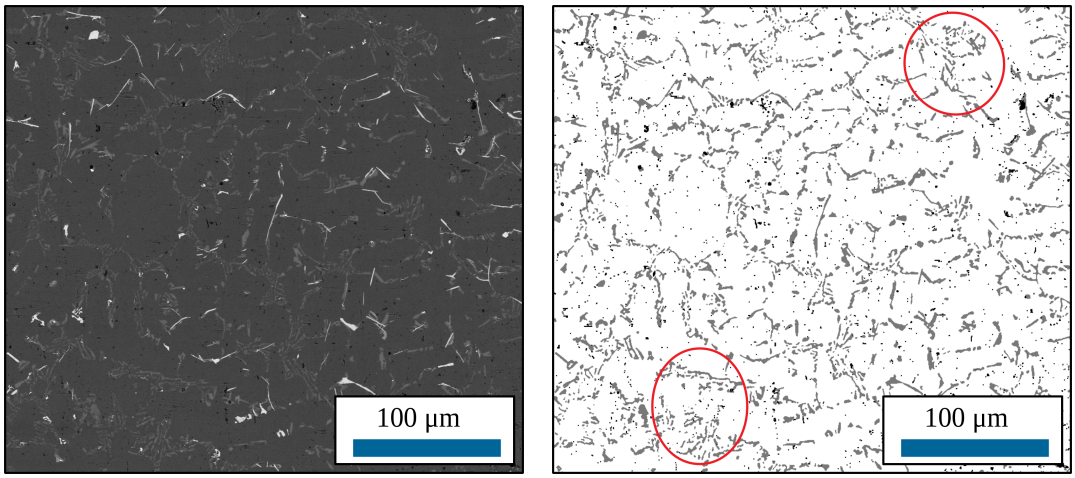

(a) **(b)**

Figure 4.24: Image segmentation for microstructure images from the large casting. (a) original image and (b) segmented image. Red circles indicate the eutectic phase.

Figure 4.25 shows the AMD results for the large casting. It can be seen that a minimum point for this case occurs at 2520 pixels (∼7.5 mm).

Figure 4.26a illustrates the macrosegregation contour plot from the image analysis. Figure 4.26b shows the plot of Si composition along the centerline of this casting. The contour plot shows a degree of enrichment in the top section of the bottom volume. Moreover, a deplete region is visible extending from the middle part of the joint to the bottom part of the top volume. Looking at the centerline, from the bottom of the casting the composition increases to a maximum of 7.9wt% Si. It then starts decreasing until the middle part of the top volume, where a slight increase can be seen.

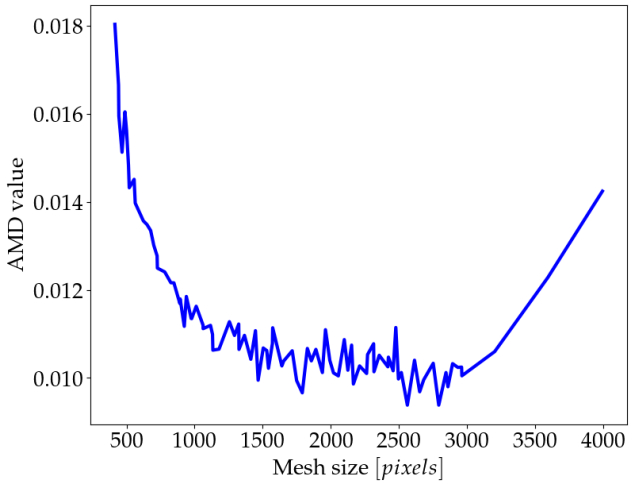

Figure 4.25: AMD curve for the large dumbbell-shaped casting.

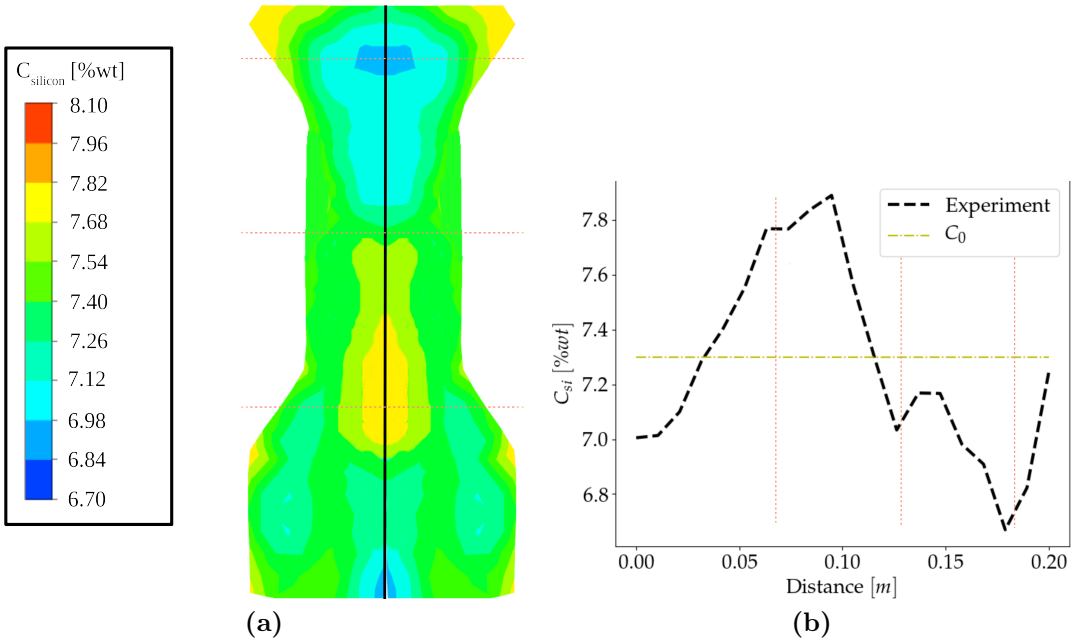

Figure 4.26: a) Contour image of Si composition on cross-section and b) plot of Si composition along the centreline of the large dumbbell-shaped casting.

4.3 Discussion

A metric is defined to measure macrosegregation in each casting based on composition variation. Macrosegregation value (the defined metric) facilitates the comparison of different cases where macrosegregation is present. The macrosegregation values were calculated by subtracting the minimum composition from maximum composition on the centreline of each casting and dividing by the nominal composition.

Table 4.1: Macrosegregation value for each casting.

Casting Condition	Macrosegregation value
Casting with natural cooling	0.29
Casting with insulated joint	0.62
Casting with the forced cooling on the joint	1.17
Large casting	0.16

Overall, comparing the composition variation along the centerline, the segregation is the lowest in the large casting followed by the casting with natural cooling and casting with insulated joint. The amount of segregation is the highest on the casting with forced cooling on the joint. In order to better understand this one should look into the the solidification behaviour of these castings.

For the case of the casting with natural cooling, there is similar cooling on the walls of each section. Therefore, some degree of encapsulation is expected in the vicinity of the section with smaller volume (i.e. the joint section). This depends on the cooling rate from the bottom plate, the lower the cooling rate the higher the chance of encapsulation. In this case, the high resolution image (Figure 4.8), shows no encapsulation in the joint section. However, the contour image shown in Figure 4.12, illustrates a non-uniform segregation along the centerline. This indicates a slight degree of encapsulation, which did not turn into shrinkage porosity. Further analyzing Figure 4.8, there can be seen a shrinkage porosity in the top section of the top volume. This porosity is in fact present in all the other castings, since the top

surface of the casting, which is open to air, solidifies first and encapsulates the liquid below.

The goal in the casting with insulated joint section was to delay the solidification in the joint section. In this case the cooling rate on the sides of the bottom and the top volumes are higher than the cooling rate on the joint section. Depending on the cooling rate from the bottom plate, this might result in solidification of the top and bottom volumes prior to the solidification of the joint section hence an encapsulation in the middle part of the joint section. Figure 4.13 shows a shrinkage porosity in the middle of the joint section, which confirms this solidification rationale. From Figure 4.16, it can be seen that the silicon variation follows the cooling procedure explained previously. There is enrichment in the region at the bottom of the joint section and a deplete region at the top of the joint section.

In the casting with forced cooling on the joint, the cooling rate on the joint section has been increased significantly. This results in solidification of the joint section prior to the solidification of the bottom volume. This then results in a large region of encapsulation, ranging from the mid point of the bottom volume to the transition to the joint section, which is prominent in Figure 4.18. Figure 4.21 shows that there is a high degree of enrichment in this area. In order to compensate for shrinkage, the casting pulled the liquid from the top part of the joint section, which resulted in a deplete region in this section.

The cooling conditions for the large casting are similar to the casting with natural cooling. Therefore, as in the smaller casting with natural cooling, there is no visible shrinkage porosity in the high resolution image (Figure 4.23). Nonetheless, the expected silicon distribution is different due to the size of the casting. The enrichment is higher in the bottom of the joint section compared to the casting with natural cooling.

Comparing the AMD curves shows that as the measured silicon distribution be-

comes more complex, the resulting AMD curves become more noisy and, the minimum AMD value increases. For instance comparing the centerline compositions of the large casting with the casting with forced cooling on the joint, the silicon mass fraction varies from 6.7%wt to 7.9%wt for the large casting. Whereas, this variation is between 4%wt and 12.6%wt for the case of forced cooling. This results in a much noisier AMD curve. Furthermore, the minimum AMD for large casting is 0.009 where the minimum AMD for the casting with forced cooling is 0.011.

4.4 Summary

A series of dumbbell-shaped castings with different sizes and cooling conditions were developed to study the effects of macrosegregation. These castings were then sectioned, polished and analyzed for silicon macrosegregation using the method discussed in chapter 3. The following is a short summary of the results:

- The casting with natural cooling resulted in no shrinkage porosity. However, analyzing the segregation map, it was concluded that there was some degree of encapsulation present in the bottom part of the joint section.

- The casting with an insulated joint section resulted in a shrinkage pore in the middle of the joint section. The segregation map for this casting showed a high degree of enrichment in the vicinity of this pore.

- The casting with forced cooling on the joint resulted in a shrinkage porosity in the bottom of the joint section which was accompanied by a high degree of enrichment.

- The large casting similar to the casting with natural cooling resulted in no shrinkage porosity. However, the segregation was more exaggerated compared to the casting with natural cooling.

- It was observed that the segregation was the highest on the casting with forced cooling rate on the joint and the lowest on the casting with natural cooling.

Chapter 5

Modeling of Macrosegregation in Shape Castings[1]

A mathematical model has been developed to better understand the various physical phenomena leading to macrosegregation in castings. The numerical simulation gives additional insight into how macrosegregation occurs by enriched compensatory flows and has been applied to the experimental casting produced for this study.

5.1 Model description

In this section, a mathematical model based on mass, energy, momentum and species conservation equations is introduced. After introducing the governing equations, the geometry and the meshing technique are discussed. This is followed by the boundary condition formulation and material properties. Finally, the solution technique is introduced.

5.1.1 Governing equations

The model uses an enthalpy-porosity method which considers the casting to be a single fluid phase (i.e. continuum assumption) where the material properties of the

[1]Portions of this chapter have been published in:

- *Khadivinassab H.*, Fan P., Reilly C., Yao L., Maijer D. M., Cockcroft S. L., Phillion A. B.,"Study of the macro-scale solute redistribution due to liquid metal feeding during the solidification of A356", Light Metals Production, Processing and Applications Symposium, The 53rd Annual Conference of Metallurgists, (2014)

fluid are a function of temperature. The governing equations for this formulation are summarized in this section.

5.1.1.1 Mass balance

The continuity equation in single-phase form is:

$$\frac{\partial \rho}{\partial t} + \nabla \cdot (\rho \mathbf{u}) = 0 \tag{5.1}$$

where ρ is the temperature dependent density and $\mathbf{u}$ is the superficial velocity given by the velocity in the liquid multiplied by the fraction liquid, this assumes that the velocity of the solid is zero. It should be noted that the mushy zone in this case is considered to be a porous media where the liquid metal flows through the pores defined by the solid microstructure. The microstructure is not tracked explicitly, instead the liquid fraction is used as an indicator of porosity level in the solidifying material.

5.1.1.2 Energy balance

The enthalpy balance is solved to predict the heat flow in the domain. The energy equation in enthalpy form is:

$$\frac{\partial \rho h}{\partial t} + \nabla \cdot (\rho \mathbf{u} h) = \nabla \cdot (k \nabla T) + S_e \tag{5.2}$$

where h is the sensible enthalpy in the system, k is the thermal conductivity and S_e is a source term added to the energy equation. The equation considers heat flow by advection, $\nabla \cdot (\rho \mathbf{u} h)$, and heat flow by diffusion,$\nabla \cdot (k \nabla T)$. The release of latent heat during solidification is included through the source term S_e which has 2 terms linked to the evolution of the fraction liquid.

$$S_e = -\frac{\partial(\rho \Delta H)}{\partial t} - \nabla \cdot (\rho \mathbf{u} \Delta H) \tag{5.3}$$

where ΔH is the incremental latent heat which is defined by overall heat released multiplied by fraction liquid. The final form of the enthalpy equation is:

$$\frac{\partial \rho H}{\partial t} + \nabla \cdot (\rho \mathbf{u} H) = \nabla \cdot (k \nabla T) \tag{5.4}$$

where H is the total enthalpy defined in equation 5.5.

$$H = h_{ref} + \int_{T_{ref}}^{T} C_p dT + \beta L_f \tag{5.5}$$

where h_{ref} is a reference enthalpy, T_{ref} is a reference temperature, L_f is the latent heat of fusion and C_p is the specific heat.

5.1.1.3 Momentum balance

To predict fluid flow during solidification, the transient momentum equations must be solved. This equation incorporates the effects of advection, buoyancy and microstructure evolution, which are explained in more detail in further paragraphs. Equation 5.6 gives the general form of the momentum equations.

$$\frac{\partial \rho \mathbf{u}}{\partial t} + (\mathbf{u} \cdot \nabla)\rho \mathbf{u} = -\nabla P + \nabla(\mu \nabla \cdot \mathbf{u}) - \nabla \times (\mu \nabla \times \mathbf{u}) + \rho \mathbf{g} + \mathbf{F} \tag{5.6}$$

where μ is the viscosity, g is the gravitational acceleration vector, P is the liquid pressure and F is a source term. The term $(\mathbf{u} \cdot \nabla)\rho \mathbf{u}$ represents the convective effects, and the terms $\nabla(\mu \nabla \cdot \mathbf{u}) - \nabla \times (\mu \nabla \times \mathbf{u})$ collectively represent the diffusive effects where viscosity acts to diffuse momentum. The term $\rho \mathbf{g}$ incorporates the effect of gravity on fluid motion.

The source term is used to incorporate the resistance of the evolving microstruc-

ture that acts to dampen flow in the mushy region. The mushy zone is assumed to be a porous media where liquid flows through the solid, porous microstructure. As noted earlier, the geometry of the solid microstructure is not predicted. The source term is added to the momentum equation based on Darcy's law (Equation 5.7).

$$\mathbf{F} = \mu \mathbf{K}^{-1} \mathbf{u} \tag{5.7}$$

where $\mathbf{K}$ is the permeability tensor. If the structure of the mushy region is assumed to be isotropic, the permeability tensor reduces to $K\mathbf{I}$ where K is a scalar function of the fraction liquid and of the morphology of the mush. K can be then approximated based on the Carman-Kozeny relation [11].

$$K = \frac{\text{DAS}^2}{180} \frac{\beta^3}{(1-\beta)^2} \tag{5.8}$$

where β is the fraction liquid. It should be noted that, in the original formulation of the Carman-Kozeny equation, the structure of mushy zone was assumed to consist of packed solid spheres with fluid flowing between them. It is a common procedure in solidification models to relate the average diameter of the solid spheres to the DAS [11]. Combining equations 5.6 to 5.8, the final form of the momentum equation can be written as:

$$\frac{\partial \rho \mathbf{u}}{\partial t} + (\mathbf{u} \cdot \nabla)\rho \mathbf{u} = -\nabla P + \nabla(\mu \nabla \cdot \mathbf{u}) - \nabla \times (\mu \nabla \times \mathbf{u}) + \rho \mathbf{g} + \frac{180\mu}{\text{DAS}^2} \frac{(1-\beta)^2}{\beta^3} \mathbf{u} \tag{5.9}$$

5.1.1.4 Solute balance

Similar to the other transport phenomena, species transport can be described by performing a species balance considering advective and diffusive contributions. In order to develop the single-phase species transport equation, one should first look at

the two-phase species transport equation (Equation 5.10):

$$\frac{\partial(\beta\rho_l C_l + (1-\beta)\rho_s C_s)}{\partial t} + \nabla\cdot(\beta\rho_l C_l \mathbf{u}_l + (1-\beta)\rho_s C_s \mathbf{u}_s) = \nabla\cdot(\beta\rho_l D_l \nabla C_l + (1-\beta)\rho_s D_s \nabla C_s) \tag{5.10}$$

where C is the concentration of solute and D is the diffusion coefficient. Subscripts s and l represent the solid and liquid phases, respectively. In order to convert this two-phase model into a one-phase model a relationship must be constructed to link the composition of liquid to the composition of solid. This can be done using the Scheil equation. To allow the Scheil approximation to be used, the solidification behaviour was based on the Al-Si binary alloy. It should be noted that by applying the Scheil approximation, this assumes no diffusion in the solid and infinite diffusion in the liquid. Therefore, the concentration of solute in the solid phase will not change with time. By considering equilibrium at the solid-liquid interface, the difference in composition in the liquid and solid at the interface is described by the partition coefficient, κ. Substituting C_s with κC_l, and, adding $\frac{\partial(\rho C_l)}{\partial t}$ to both sides of the equation, the final form of the solute transport equation is arrived at:

$$\frac{\partial(\rho C_l)}{\partial t} + \nabla\cdot(\rho C_l \mathbf{u}) = \nabla\cdot(D^+ \nabla C_l) - \frac{\partial((1-\beta)\rho C_l)}{\partial t} - \kappa C_l \frac{\partial((1-\beta)\rho)}{\partial t} \tag{5.11}$$

where D^+ is given by $\rho\beta D_l$. It should be noted that in this equation velocity of solid phase was considered zero as there is no solid phase movement.

5.1.1.5 Fraction liquid

Older solidification simulation methods use fixed temperature/solute dependent liquid fraction formulation, where the user should manually input the liquid fraction. In this

simulation an automated technique is used to update the liquid fraction as a function of the interface temperature.

The simplest method to calculate the fraction liquid is to use a temperature ratio. From the phase diagram of a binary alloy, when the temperature T is greater than the solidus temperature and smaller than the liquidus temperature, one can write:

$$\beta = \frac{T - T_{sol}}{T_{liq} - T_{sol}} \tag{5.12}$$

Employing this formulation results in instability in the numerical solution procedure [78]. Moreover, this formulation does not represent the liquid fraction accurately, as it is only taking into consideration the temperatures. Voller *et al.* suggested a method to calculate fraction liquid based on the Scheil equation which proved to be stable [78]. The other advantage of this method is that it can be applied to a fixed grid. This formulation is based on an iterative method which used the following equations:

$$\beta^{n+1} = \beta^n - \lambda \frac{a_p(T - T^*)\Delta t}{\rho V L - a_p \Delta t L_f \frac{\partial T^*}{\partial \beta}} \tag{5.13}$$

where λ is a relaxation factor, a_p is coefficient in discretization equation, Δt is time-step, V is the cell volume and T^* is the interface temperature given by Scheil equation as follows:

$$T^* = T_{melt} - (T_{melt} - T_{liq})\beta^{(\frac{T_{sol} - T_{liq}}{T_{melt} - T_{sol}})} \tag{5.14}$$

where T_{melt} is the melting point of the pure substance. It should be noted that T_{sol} and T_{liq} are dependent upon the changes in local composition, and can be accessed using equations 5.15 and 5.16.

$$T_{sol} = T_{melt} + MC_{Si}/\kappa_{Si} \tag{5.15}$$

$$T_{liq} = T_{melt} + MC_{Si} \tag{5.16}$$

where M is the slope of the liquidus surface.

5.1.2 Geometry

To reduce the computational requirements for the model, the dumbbell casting was assumed to be symmetric about the centerline, allowing a 2D axisymmetric domain to be adopted. The geometry, mesh and boundary conditions used in the model are shown in Figure 5.1. The mesh is generated using quadrilateral elements of length 3.5mm for the regular mould and 7.5mm for the large casting. It should be noted that using a very small mesh size resulted in increased computation time and increased chance of divergence. increasing the mesh size on the other hand, resulted in divergence and increased levels of inaccuracies. Both the geometry and the mesh were generated using Ansys Workbench.

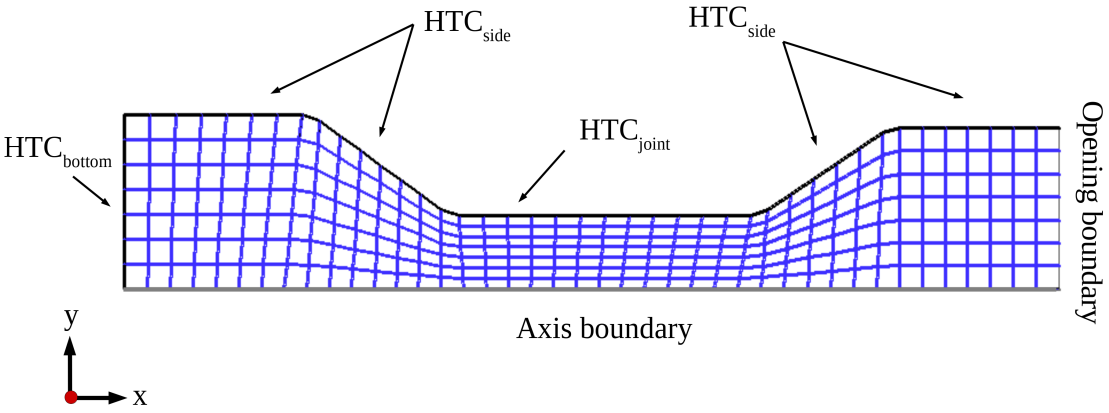

Figure 5.1: Geometry, mesh and boundary conditions of model.

5.1.3 Boundary conditions

As can be seen from Figure 5.1 there are three types of boundary conditions in this simulation: Wall type, Opening type and Axis type boundary conditions. The Wall type boundaries include bottom Heat Transfer Coefficient (HTC), side HTC and joint HTC. The following is the description of each of the boundary conditions.

5.1.3.1 Wall boundary conditions

Wall type boundary condition assume a no-slip condition where velocity of the fluid at the wall is zero. Heat transfer through the wall is specified based on HTCs.

In order for the model to accurately reflect the heat transfer present in the dumb-bell castings for the three different cooling conditions, the HTCs applied to the side wall of the casting were adjusted so that the predicted temperatures matched the measured temperature from the experiment. This was a complex task because each HTC was customizable for each section (i.e. bottom side, joint side, and top side) and for the different cooling conditions (i.e. natural convection, forced convection, and insulation). To begin with, the HTCs of the side wall sections of the mould were first approximated by a heat transfer resistance approximation. As the model does not include geometry/mesh representing the copper mould and the region surrounding the casting, an estimate of the overall HTC between the casting outer surface and the ambient environment was needed. Despite this calculation, the values do not represent the initial heat transfer between the mould and the melt. This was accounted for by adding a large HTC value for the first few seconds of the solidification.

As shown in Figure 5.2a, an interface exists between the casting surface and the inner surface of the mould. An Interfacial Heat Transfer Coefficient (IHTC) is defined between these two sections. It is assumed that when the metal is liquid, there is perfect contact (i.e. a high IHTC) between the casting and the mould. However, as the metal solidifies, the contact degrades as small local gaps form along the interface

(depicted in Figure 5.2a). Therefore, the value of the IHTC changes as a function of temperature. There have been various studies published on IHTC evaluation during casting. Trovant *et al.* recommend an IHTC of 500 W/m^2K for the temperatures colder than solidus temperature and 2300 W/m^2K for the temperatures hotter than solidus for solidification of A356 in a copper mould [79].

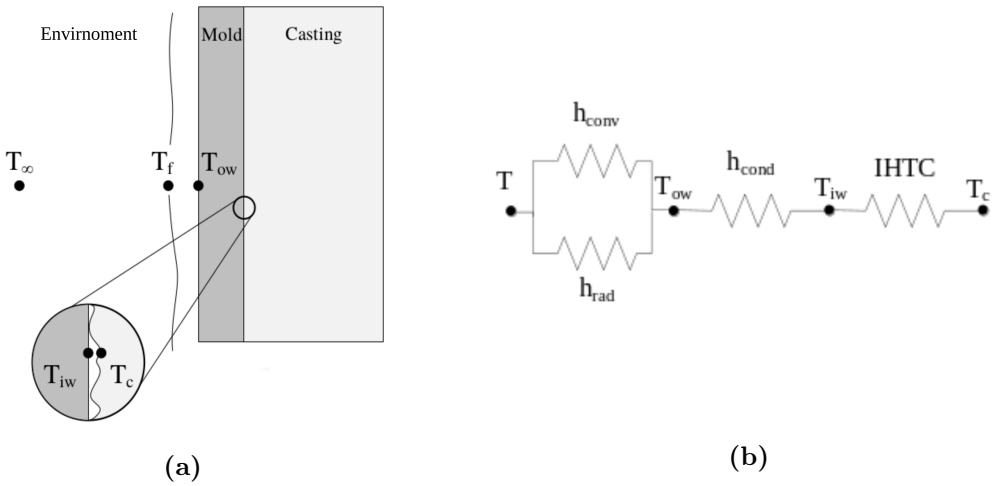

Figure 5.2: (a) Depiction of a part of the casting system with relevant temperature points, (b) Respective resistance model for heat transfer calculation.

Heat transfer can be modeled after electrical circuits, where heat flux acts as current, temperature acts as voltage and heat transfer coefficient acts as resistive impedance (reciprocal of resistance). Similar to an electric circuit, one can find the equivalent HTC by adding the individual HTCs. For the HTCs connected in parallel, the equivalent HTC is calculated by adding the individual heat transfer coefficients. However, for the components connected in series, the equivalent HTC is calculated by taking the reciprocal of the summation of the reciprocals of the individual HTCs.

The calculation of an equivalent resistance for heat conduction in the copper mould is straight forward and can be determined by dividing the width of the section by the conductivity of copper. Estimating the HTC between the outer surface of the

mould and the ambient environment, however, is a difficult task, thus a number of assumptions have been made. First, it is assumed that heat flows out of the mould by two parallel mechanisms: convection (natural or forced) and radiation. In Figure 5.2b, these mechanisms are illustrated using two parallel resistors.

The HTC for natural convection (laminar flow) can be calculated using the Churchill-Chu correlation given in Equation 5.17 [80].

$$h_{conv} = \frac{k}{L}\left(0.825 + \frac{0.387Ra^{1/6}}{(1+(0.492/Pr)^{9/16})^{8/27}}\right)^2 \tag{5.17}$$

where L is the characteristic length, Pr is the Prandtl number and Ra is the Rayleigh number associated with the characteristic length. It should be noted that this equation is valid for Rayleigh numbers above 10^9.

The HTC for forced convection conditions may be calculated using Churchill-Bernstein correlation given in Equation 5.18 [80].

$$h_{conv} = \frac{k}{L}\left(0.3 + \frac{0.62Re^{1/2}Pr^{1/3}}{(1+(0.4/Pr)^{2/3})^{1/4}}\left(1+(Re/282000)^{5/8}\right)^{4/5}\right) \tag{5.18}$$

where Re is the Reynolds number. It should be noted that this equation is valid when $PrRe > 0.2$.

In order to calculate accurate HTCs using these equations, the temperature dependent material properties for air must be used. As illustrated in Figure 5.2a, a boundary layer is expected to develop on the mould wall and the material properties of air are assumed to be dependent upon the temperature in the boundary layer. This temperature is calculated by averaging the ambient temperature and the temperature of the outer surface of the mould.

To estimate the radiative heat transfer contributions to cooling on the side wall, a radiative HTC was calculated. It was assumed that the hot mould is radiating energy to its cooler surroundings (ambient environment in our case). The following equation can be used to calculate the radiative heat transfer coefficient:

$$h_{rad} = \varepsilon\sigma(T_{side} + T_{\infty})(T_{side}^2 + T_{\infty}^2) \tag{5.19}$$

where ε is the emissivity and σ is the Stefan-Boltzmann constant.

Combining the resistances defined, the effective heat transfer coefficient was determined and illustrated in Figure 5.3 for both natural and forced convection. The effective HTCs are only dependent upon the temperature of the casting surface and therefore can be used directly in the simulations.

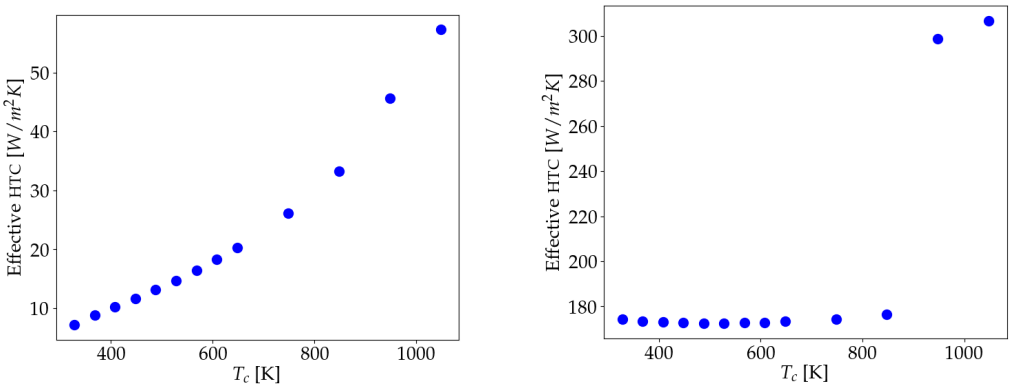

Figure 5.3: Effective heat transfer coefficient due to (a) natural and (b) forced convection in a copper mould.

As mentioned previously, these HTCs do not take into account the initial heat transfer between the mould and the melt. In the simulation, the copper mould assumed to initially absorb a large amount of heat, with HTC of 1200 W/m^2K. The HTC then gradually reduces to the steady state value over a duration of 5 seconds.

The side HTC in the castings for all three cases were based on the effective HTC

values for natural cooling. The joint HTC was consistent with the different conditions. For the case of natural and forced cooling, the joint HTC was considered to be the calculated effective HTC, respectively. For the insulated case, the effective HTC was held constant at 15 W/m^2K. It should be noted that this value was determined through trial and error.

The bottom HTC was assumed to have a behaviour similar to the side HTC. However, since it has a thicker cross-section and is in contact with a support, the effective HTC was initially assigned to be 2000 W/m^2K and it gradually decreases over 10 seconds to the nominal value of 20 W/m^2K. It should be noted that these values were chosen by trial and error during a fitting exercise.

5.1.3.2 Opening Boundary Condition

Due to changes in density in the casting (shrinkage due to the phase change and overall thermal contraction), a boundary condition was needed so that mass stays conserved. It should be noted that if the configuration does not include an Opening Boundary Condition, continuity equation will diverge due to changes in density. An opening boundary condition was applied at the top of the casting domain to give the model the ability to draw material in to the domain to compensate for the shrinkage. Although this seems far from what happens in the real-life case, the parameters of the opening boundary condition can be adjusted to achieve better accuracy, while conserving mass.

The Opening Boundary Condition, applied to the top of the casting domain, enables material to be drawn into the domain with predefined temperature and composition. In this study, the temperature and composition of the material entering the domain at each time step was set to be equal to the temperature and composition of the metal at the boundary elements. This results in a zero gradient in temperature and composition at the boundary. It should be noted that a more accurate

representation of temperature would be to draw in a different material, such as air, with a temperature equal to the surrounding air temperature during the experiment and with appropriate properties so that the heat flux between the casting and the air would better represent the experiment. This implementation was explored during model development but it was eventually discarded as it resulted in divergence.

It is expected that zero temperature gradient would result in underestimation of HTC at the top section, hence a higher temperature is expected at the top section.

5.1.3.3 Axis boundary condition

The axis boundary condition is used to implement the axisymmetric formulation. This means that at a particular radius from the axis and a particular height, each flow variable has the same value on different angles.

5.1.4 Material properties

The thermo-physical properties for A356 used in the model are summarized in Table 5.1 and Figure 5.4.

Table 5.1: Thermo-physical properties used in the mathematical model.

Properties	Value	References
k	Figure 5.4a	[81]
C_p	Figure 5.4b	[81]
L_f	395000 J/kg	[82]
ρ	Figure 5.4c	[81]
μ	Figure 5.4d	[81]
κ_{Si}	0.13	[83]

The values for thermal conductivity linearly decrease in solid zone from 163 to 144 $W/m.K$. The value of thermal conductivity for liquid zone, is an enhanced value of 400 $W/m.K$ in order to account for the convection in liquid zone. The values in the mushy zone are interpolated linearly based on temperature. Specific heat

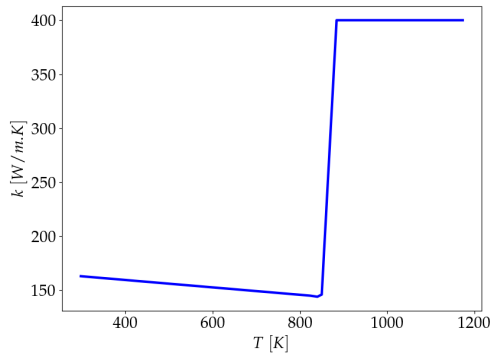

(a) Temperature dependant thermal conductivity.

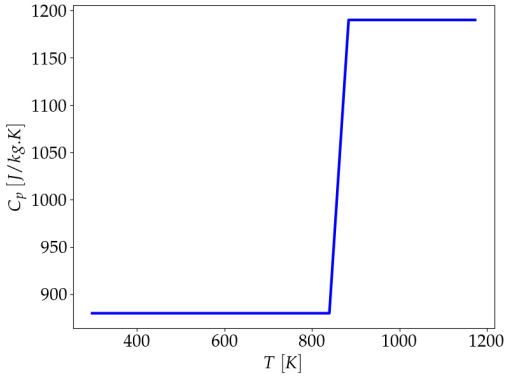

(b) Temperature dependant specific heat.

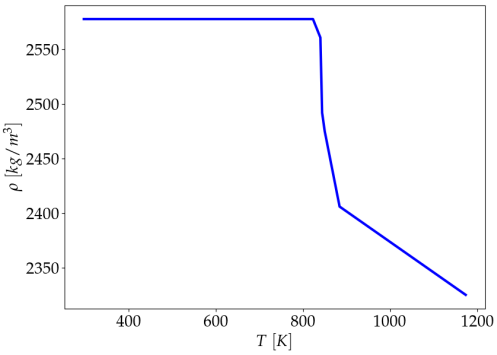

(c) Temperature dependant density.

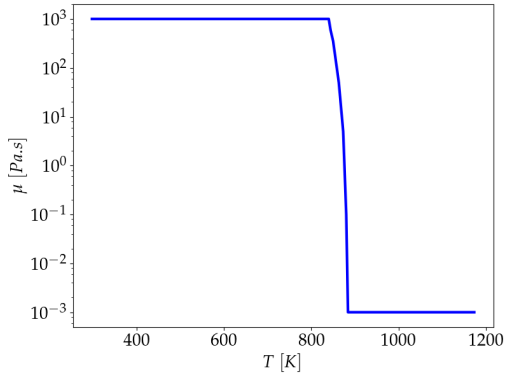

(d) Temperature dependant viscosity.

Figure 5.4: Temperature dependant material properties.

exhibits values of 880 and 1190 $J/kg.K$ for the solid and liquid phases. The values in the mushy zone are interpolated linearly as function of temperature. Density was assumed to have a constant value of 2578 kg/m^3 in the solid region. In the liquid zone it linearly decreases from 2406 to 2325 kg/m^3. Density in the mushy zone was approximated using three points as shown in Figure 5.4c. Viscosity in the liquid zone was set to 0.001 $Pa.s$. In the solid region it was set to a very large value (1000 $Pa.s$) to constrict the flow. The values in the mushy zone were interpolated as shown in Figure 5.4d.

5.1.5 Solution procedure

A coupled thermal - fluid flow - composition model, based on the equations, boundary conditions, and material properties described in the previous sections, was developed using the commercial Computational Fluid Dynamics (CFD) software package FLUENT to predict solute (silicon) segregation during solidification of the dumbbell castings. The model incorporates the relevant solidification phenomena including mushy zone resistance (Darcy flow damping), latent heat evolution, buoyancy, and silicon partitioning during the phase transformation. An incremental approach was taken to develop the coupled thermal - fluid flow - composition model, where the complexity of the model was increased in stages.

Four cases were simulated based on the four experiments explained in the previous chapter: natural cooling, insulated, forced cooling and natural cooling of a large casting. Testing and validation of the model was performed in two stages in this study. Initially, the temperature data from the simulation was compared against the thermocouple data from the experiment and the heat transfer coefficients were adjusted until the predicted temperature history matched the measured temperatures. In the second stage, the macrosegregation results from the simulation were compared and validated against the results from the image processing technique.

5.2 Results

5.2.1 Casting with natural cooling

Figure 5.5 shows the comparison of thermocouple data from experiment and simulation for the dumbbell-shaped casting with natural cooling conditions. Results show a good fit in thermocouple data between the experiment and simulation. To achieve this fit, the heat transfer coefficient were manipulated as explained in section 5.1.3.1. The only inconsistency seems to be the top thermocouple (TC4). This is the result

of complications arising from the top opening boundary condition description. In FLUENT, it is not possible to define an HTC for the opening boundary condition. As discussed in section 5.1.3.2, this results in overestimation of temperature.

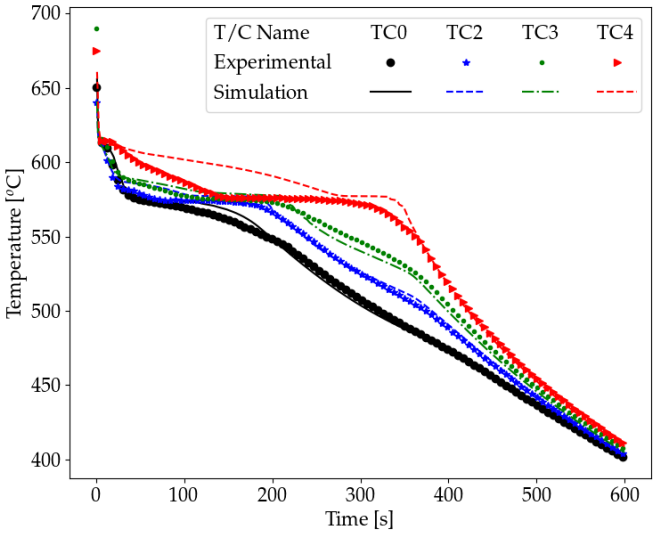

Figure 5.5: Thermocouple data from experiment and simulation for the dumbbell-shaped casting with natural cooling conditions.

Temperature contours from the dumbbell-shaped casting with natural cooling conditions are shown in Figure 5.6. It should be noted that solidification progress was calculated based on the solidification time. As can be seen, the solidification at first is not directional (temperature exhibits an increasing-decreasing-increasing profile) but it becomes directional as the HTCs decrease (temperature is increasing uniformly from bottom to top).

Figure 5.7 shows the liquid encapsulation plots from the simulation. These plots were generated based on the liquid fraction of 0.5. Since the liquid metal flow beyond this liquid fraction is negligible, the liquid metal feeding to encapsulated areas is cut. It is suggested from the results that the two areas shown are prone to shrinkage porosity since liquid is encapsulated and there is no feeding.

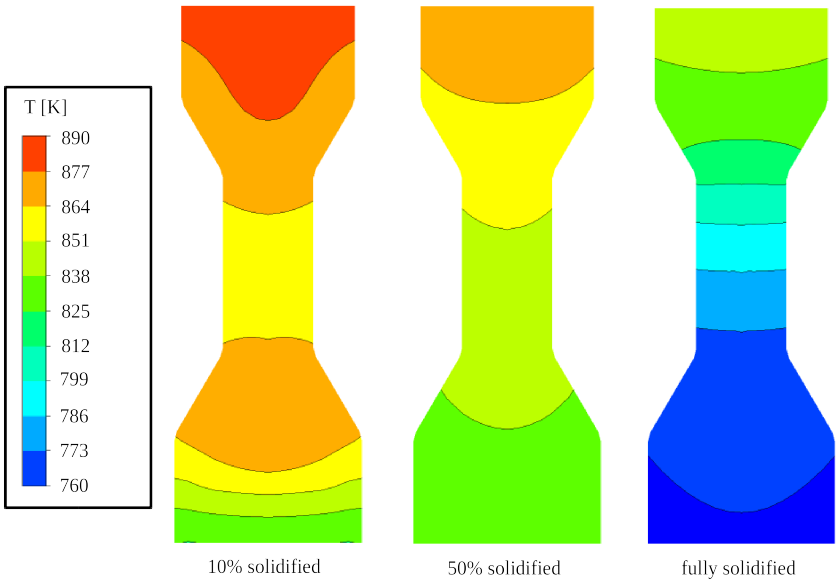

Figure 5.6: Temperature contours from the dumbbell-shaped casting with natural cooling conditions.

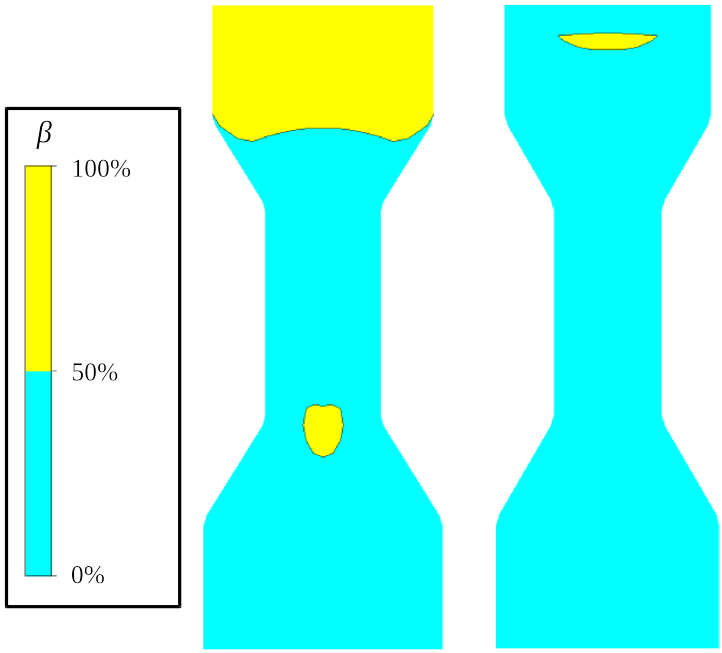

Figure 5.7: Liquid encapsulation results from simulation for the dumbbell-shaped casting with natural cooling conditions.

Figure 5.8 shows the silicon segregation in the dumbbell-shaped casting with natural cooling conditions. A silicon-enriched region occurs in the vicinity of the encapsulated region shown in Figure 5.7. A silicon-deplete region can be seen at the bottom of the top volume, where it is attached to the neck.

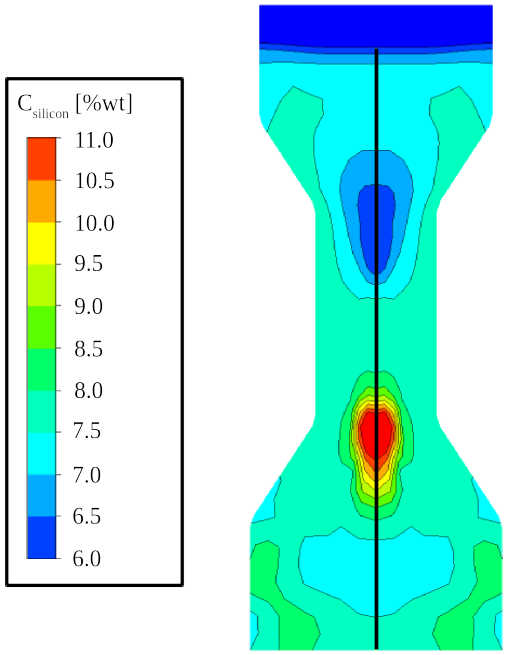

Figure 5.8: Simulated silicon segregation in the dumbbell-shaped casting with natural cooling conditions.

Figure 5.9 shows comparison of measured and predicted silicon mass fraction along the centerline of the dumbbell-shaped casting cooled by natural convection (refer to Figure 5.8). Moving up the centerline from the bottom of the casting, the predicted Si content increases rapidly until a maximum is reached in the bottom volume. Continuing along the centerline, the silicon concentration then decreases until the top volume is reached. In the top volume, a slight increase is observed. Finally, at the top of the casting, a deplete region is predicted. The measured Si composition exhibits similar trends to the predicted in terms of where the composition increases and decreases, however, the magnitude of the maximum composition predicted in the

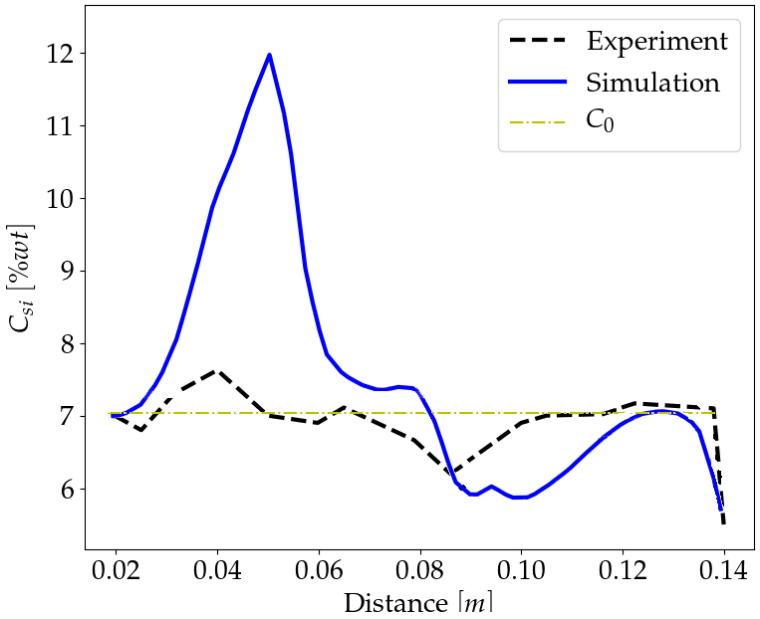

Figure 5.9: Silicon mass fraction along the centerline from the experiment and the simulation for the dumbbell-shaped casting with natural cooling conditions.

bottom volume is much higher than measured.

5.2.2 Casting with insulated joint

Figure 5.10 shows a comparison of the measured and predicted temperatures for the insulated dumbbell-shaped casting. Similar to the previous case there is some inaccuracy in predicting the top thermocouple, but overall the predicted temperatures match the measured temperatures at most of the locations in the casting. Figure 5.11 shows the temperature contours for the insulated case. The temperature contours show an encapsulated area at 10% solidified configuration. However, after this point the solidification exhibit a directional nature.

Figure 5.12 shows the liquid encapsulation plots from the simulation. Results show that two areas are prone to shrinkage porosity since liquid is encapsulated and there is no feeding.

Figure 5.13 shows the silicon segregation in the insulated dumbbell-shaped casting.

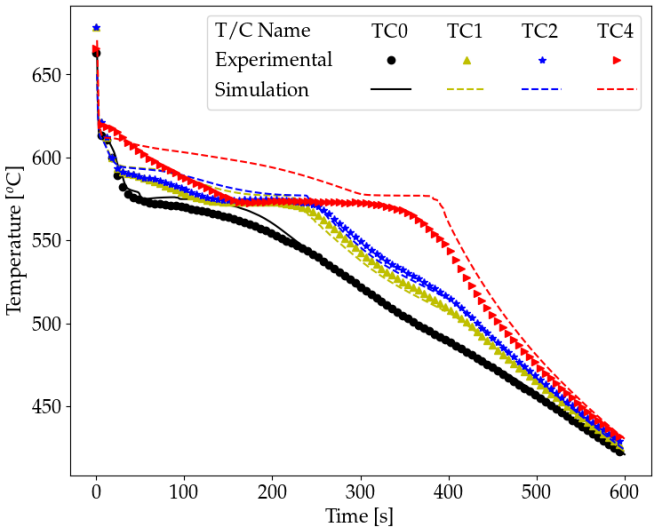

Figure 5.10: Thermocouple data from experiment and simulation for the insulated dumbbell-shaped casting.

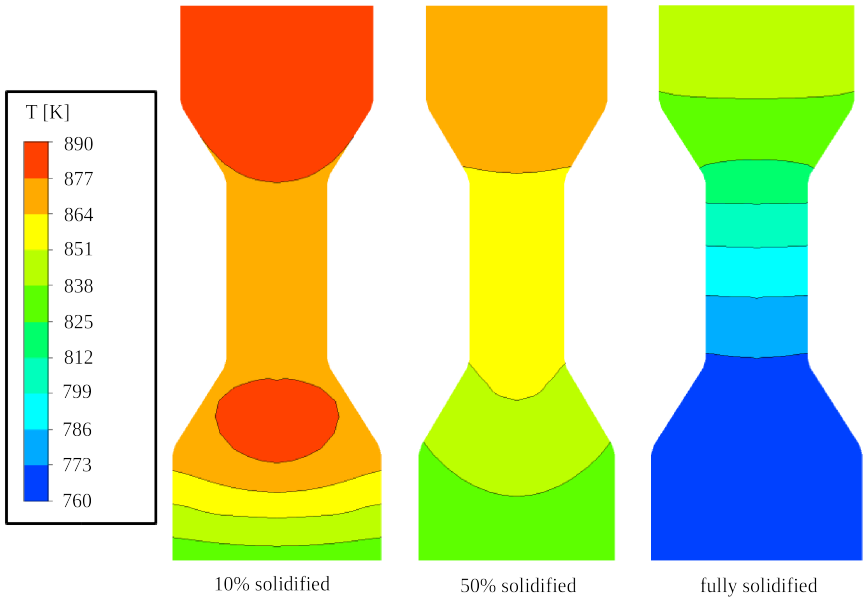

Figure 5.11: Temperature contours from the insulated dumbbell-shaped casting.

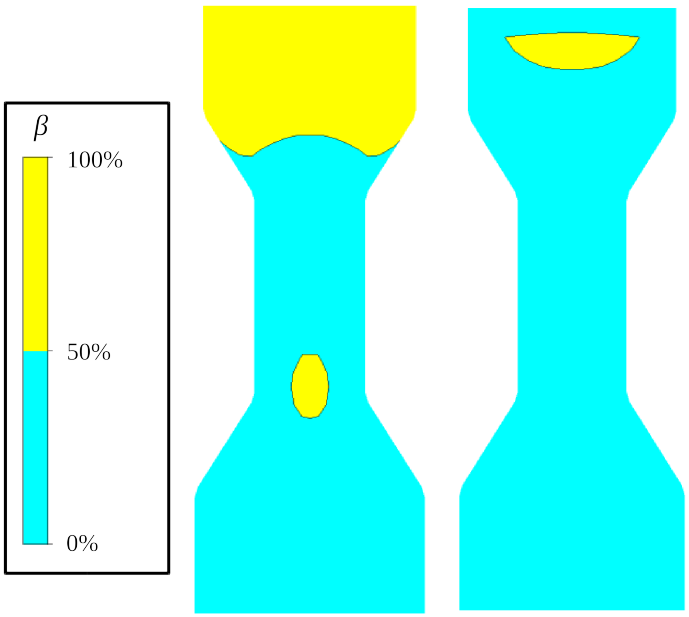

Figure 5.12: Liquid encapsulation results from simulation for the insulated dumbbell-shaped casting.

A silicon-enriched region is observable in the vicinity of the encapsulated region shown in Figure 5.12. A silicon-deplete region can be seen at the bottom of the top volume, where it is attached to the neck. These results are similar to the observations from the casting with natural cooling conditions. Nevertheless, the variation of silicon in the latter case is higher.

Figure 5.14 shows comparison of silicon mass fraction from the experiment and the simulation along the centerline shown in Figure 5.13. The results show good agreement. However, the simulated scenario shows higher silicon concentration in the enriched region comparing to the experimental results.

5.2.3 Casting with forced cooling on the joint

Figure 5.15 shows the comparison of the measured and predicted temperature history for the dumbbell-shaped casting with forced cooling. Similar to the previous cases there is some inaccuracy in the predictions for the top thermocouple, but the comparison is good at the other thermocouple locations in the casting. Figure 5.16

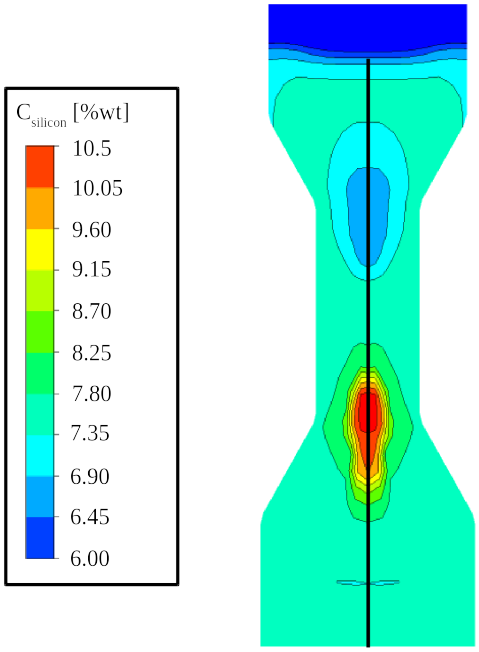

Figure 5.13: Simulated silicon segregation in the insulated dumbbell-shaped casting.

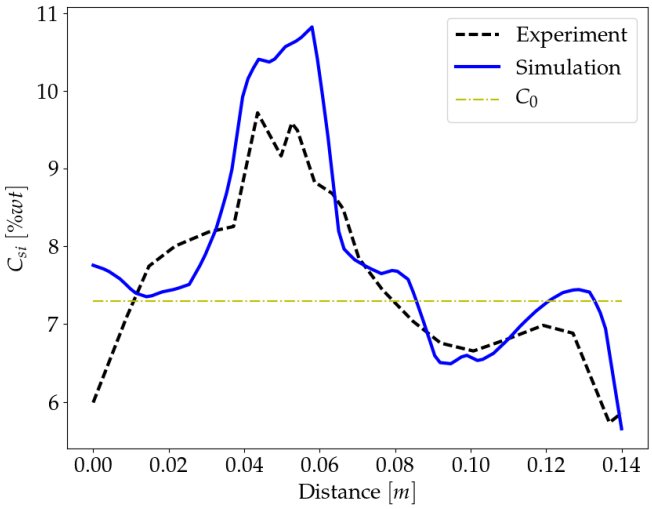

Figure 5.14: Silicon mass fraction along the centerline from the experiment and the simulation for the insulated dumbbell-shaped casting.

shows the temperature contours for the case with forced cooling. As expected, The temperature gradients developed in this case are much larger than of previous two cases.

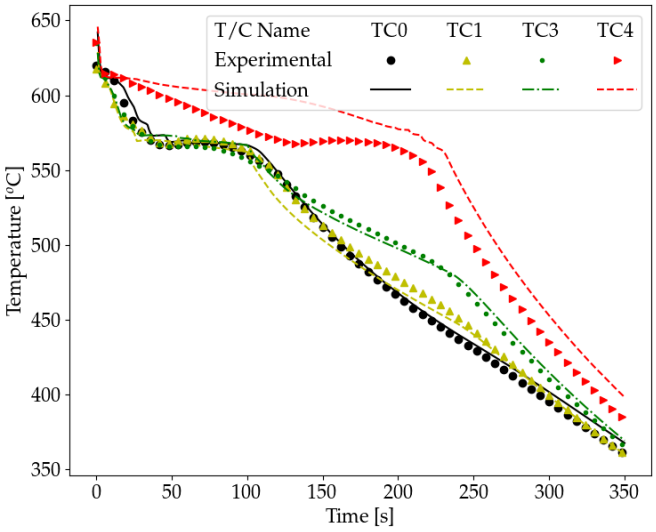

Figure 5.15: Thermocouple data from experiment and simulation for the dumbbell-shaped casting with forced cooling.

Figure 5.17 shows the liquid encapsulation plots from the simulation. Similar to the previous cases there are two areas prone to shrinkage porosity. It should be noted that the location of the encapsulated region in the bottom of the joint section is lower one on the previous two cases.

Figure 5.18 shows the silicon segregation in the dumbbell-shaped casting with forced cooling. A silicon-enriched region is observable in the vicinity of the encapsulated region shown in Figure 5.17. This region is much larger than the previous cases. Similar to the previous cases, a silicon-deplete region can be seen at the bottom of the top volume, where it is attached to the neck. The variation of silicon throughout the casting is higher than the previous cases.

Figure 5.19 shows comparison of the measured and predicted silicon mass fraction

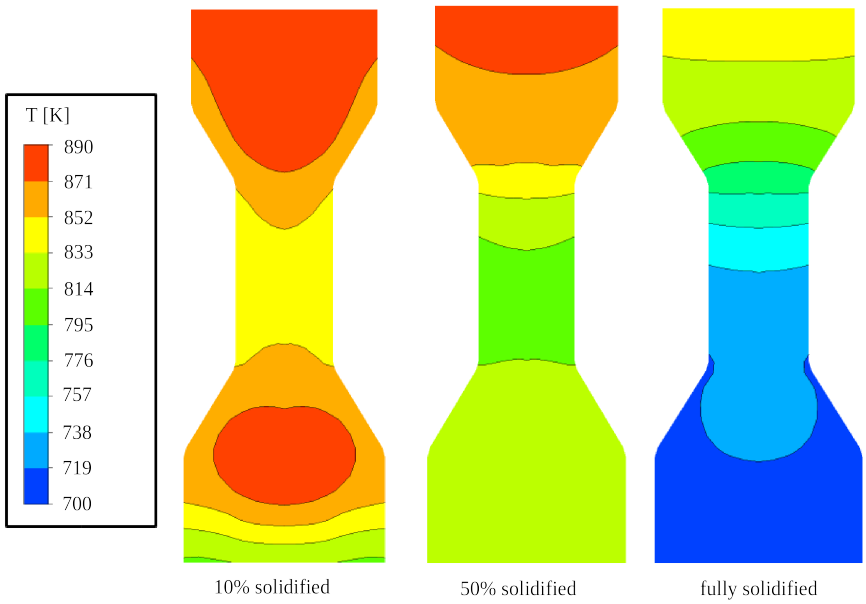

Figure 5.16: Temperature contours from the dumbbell-shaped casting with forced cooling.

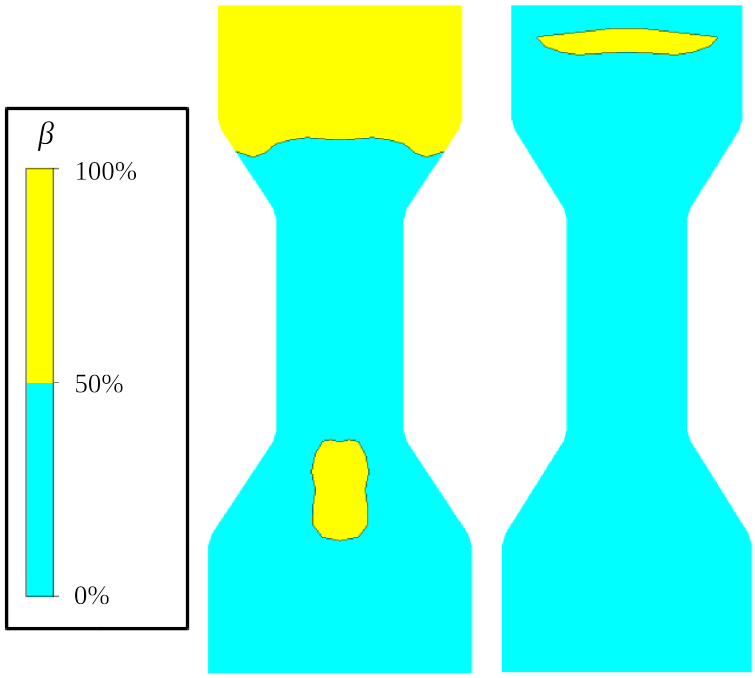

Figure 5.17: Liquid encapsulation results from simulation for the dumbbell-shaped casting with forced cooling.

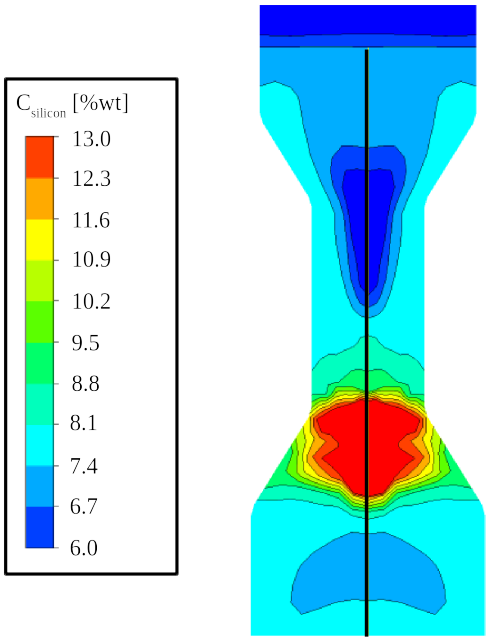

Figure 5.18: Simulated silicon segregation in the dumbbell-shaped casting with forced cooling.

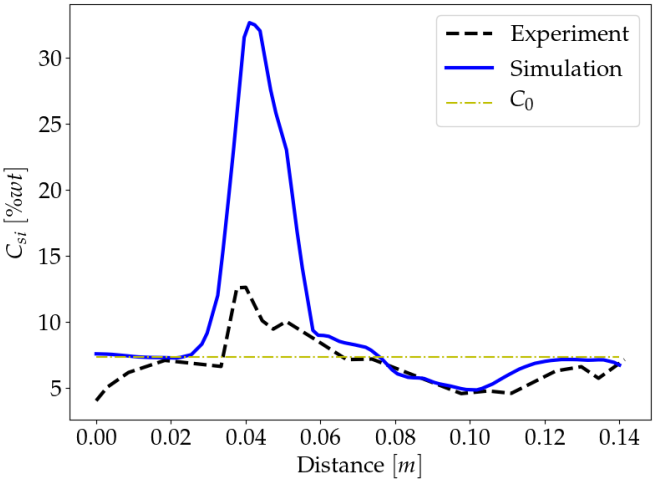

Figure 5.19: Silicon mass fraction along the centerline from the experiment and the simulation for the dumbbell-shaped casting with forced cooling.

along the centerline of the dumbbell-shaped casting with forced cooling (refer to Figure 5.18). The predictions show higher silicon concentration in the enriched region compared to the experimental results. The area of discrepancy, similar to the previous cases, lies in the vicinity of the encapsulated region at the bottom of the joint section.

5.2.4 Large casting

Figure 5.20 shows a comparison of the measured and predicted temperature history for the large dumbbell-shaped casting. Similar to the previous cases there is some inaccuracy in predicting the top thermocouple, but the temperature predictions at the remaining thermocouple locations are accurate. Figure 5.21 shows the temperature contours for the large casting. At 10% solidified, the figure shows the onset of liquid encapsulation . However, similar to the previous cases the solidification exhibits a directional nature.

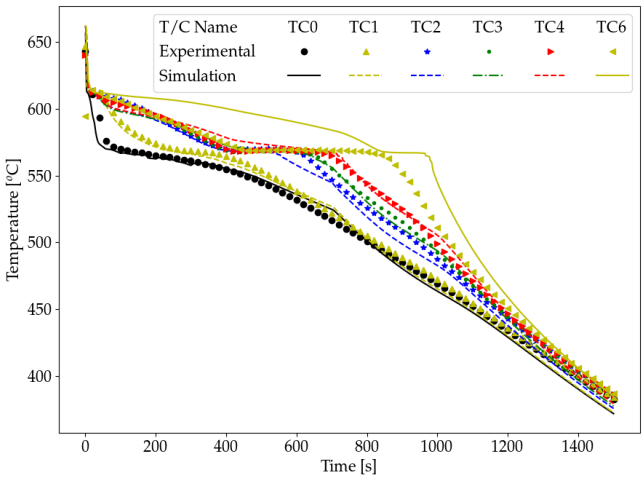

Figure 5.20: Thermocouple data from experiment and simulation for the large dumbbell-shaped casting.

Figure 5.22 shows the liquid encapsulation plots from the simulation. Similar to the previous cases there are two areas prone to shrinkage porosity. The encapsulated regions are similar in position compared to the previous cases.

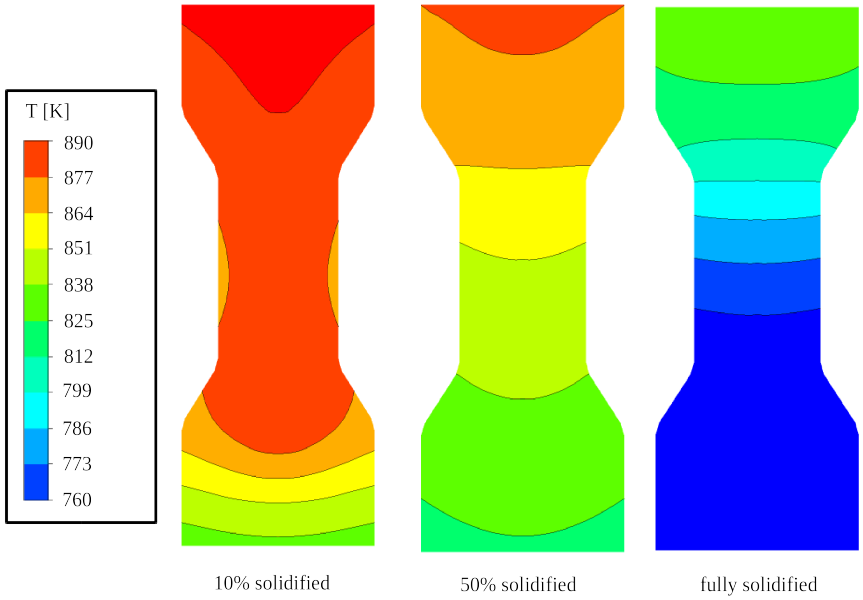

Figure 5.21: Temperature contours from the large dumbbell-shaped casting.

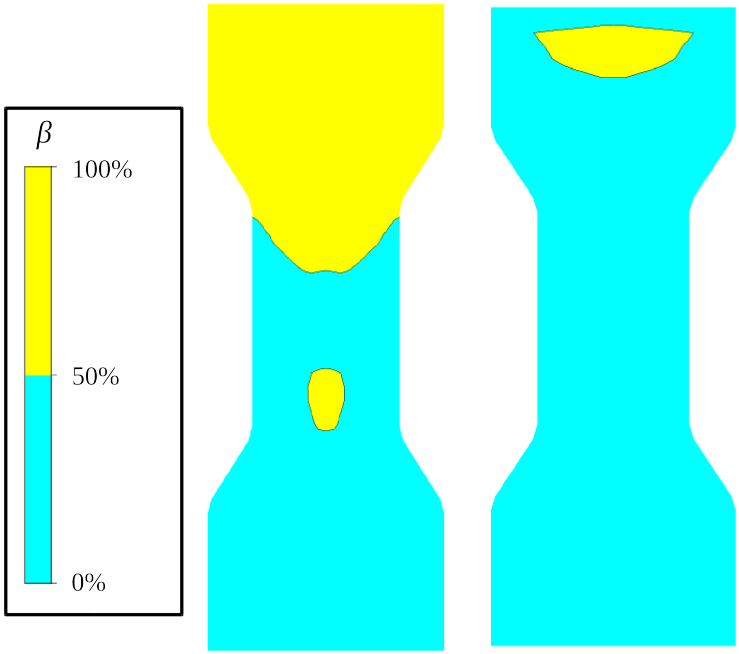

Figure 5.22: Liquid encapsulation results from simulation for the large dumbbell-shaped casting.

Figure 5.23 shows the silicon segregation in the dumbbell-shaped casting with forced cooling. A silicon-enriched region is observed in the vicinity of the encapsulated region shown in Figure 5.22. The silicon content variation is smaller compared to other cases presented previously.

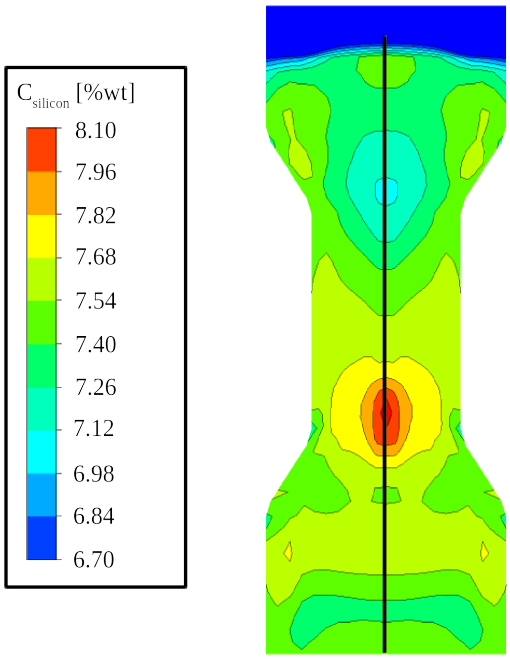

Figure 5.23: Simulated silicon segregation in the large dumbbell-shaped casting.

Figure 5.24 shows a comparison of measured and predicted silicon mass fraction along the centerline of the large dumbbell-shaped casting (refer to Figure 5.18). As can be seen, both measured and predicted Si composition values start from a low value of silicon mass fraction and move to a maximum at around 10cm from the bottom of the casting. Afterwards a gradual decrease is evident from the graph for both cases. The composition then starts increasing starting from the bottom of the top volume until the middle of this volume at around 21cm from the bottom.

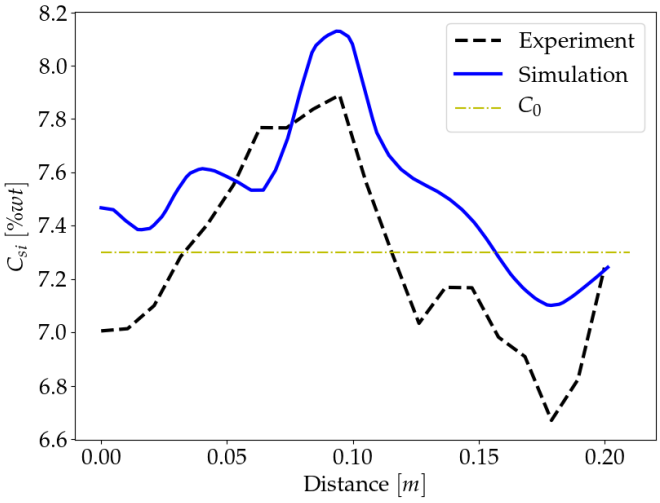

Figure 5.24: Silicon mass fraction along the centerline from the experiment and the simulation for the large dumbbell-shaped casting.

5.3 Discrepancy in the enriched region

Based on the results presented in the previous section, the prediction of liquid encapsulation in / near the joint section seems to correspond to over-prediction of the silicon composition in this area. This is especially evident in the forced cooling case, where the model over-predicts the composition in the transition from the bottom volume to the joint section by approximately 40%. The predicted value at this region also raises questions because it increases well above the eutectic composition. It seems that this over-prediction is also related to the cooling rate as well. For cases with low cooling rates, i.e. the casting with insulated joint and large casting, the over-prediction is minimal and the results match the experimental cases. Nonetheless, for the castings produced with natural cooling and forced cooling conditions, where the cooling rates are higher, the simulation and experimental results exhibit substantial discrepancies.

To further analyze this discrepancy, predicted liquid encapsulation and composition results for the casting with forced cooling on the joint, where the observed discrepancy is the highest, were plotted side by side at different instances during so-

lidification. The time instances were based on the onset of encapsulation ($t = 12s$), the end of solidification ($t = 150s$) and several intermediate values shown in Figure 5.25.

It can be seen from Figure 5.25 that liquid encapsulation in the bottom of the joint region occurs at time $t = 12s$. It is expected that since the liquid metal feeding to this region is restricted at this time, there should be no increase in the silicon concentration. However, the enriched region keeps growing in the next instances. Figure 5.26 shows the Si mass fraction along the centerline for these instances.

The results from Figure 5.26 show that the composition keeps increasing in the encapsulated region even after the eutectic composition is reached which is physically unrealistic. This suggests that the simulation is encountering a numerical instability in this region. This may be influenced by the high heat transfer rates in the castings with natural cooling and forced cooling on the joint. However, since the HTCs are set to match the heat transfer rates of the experiments, any changes in HTCs would result in deviation of the thermal history.

It is a common practice in CFD to utilize relaxation factors to overcome instability and divergence problems [84]. Relaxation factors control the stability and convergence rate of the iterative process. Under relaxation increases the stability while over relaxation increases the rate of convergence [84]. Equation 5.20 shows the implementation of this concept.

$$x^{k+1} = \alpha x^{calc} + (1 - \alpha)x^{k} \tag{5.20}$$

where x is a variable that is being solved for by a differential equation, superscripts $k+1$ and k are the iteration steps, and x^{calc} is the current solution of the variable for the differential equation. α is considered to be an under-relaxation factor if $0 < \alpha < 1$ and an over-relaxation factor if $1 < \alpha < 2$.

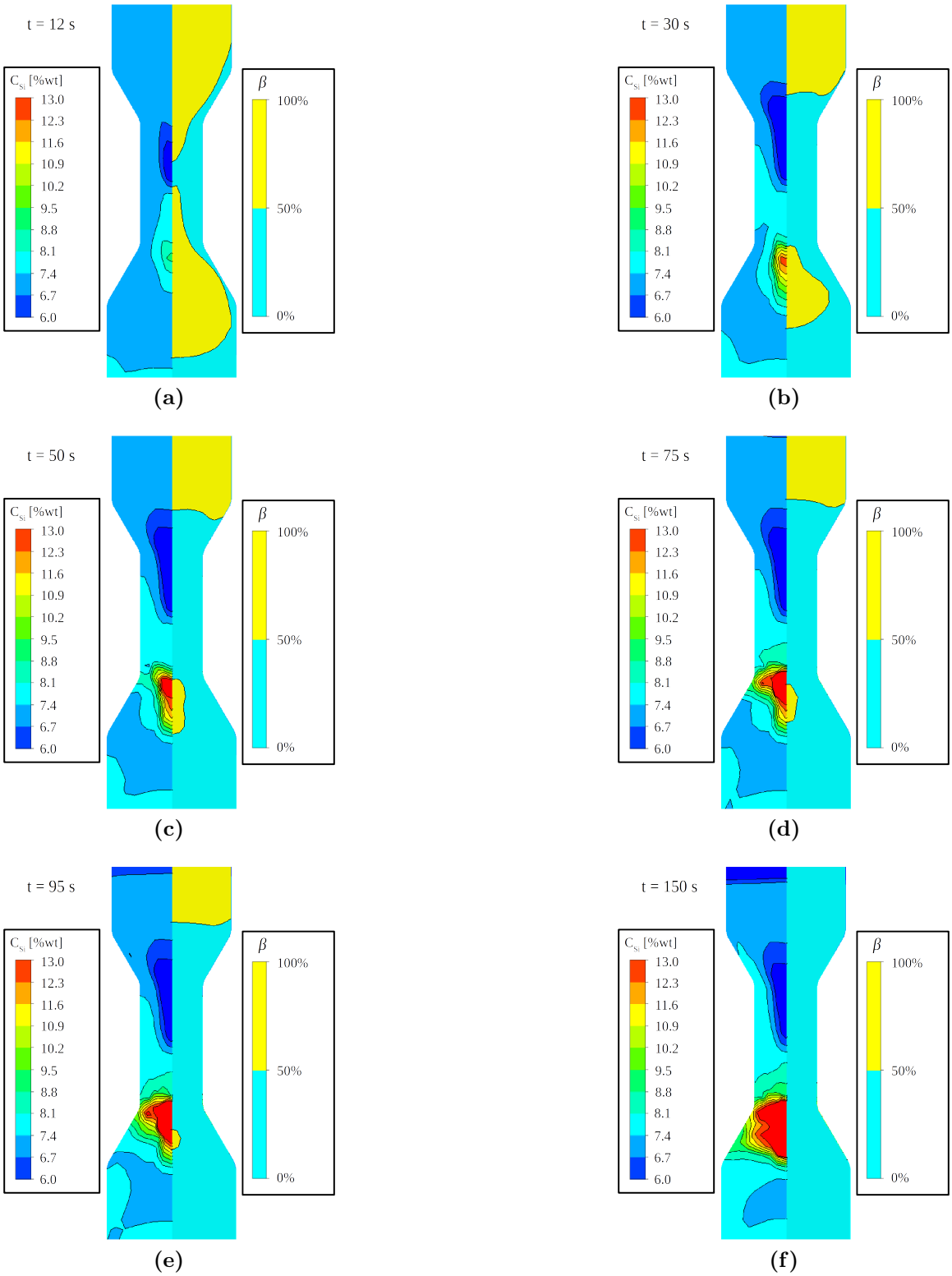

Figure 5.25: Development of over-prediction of enrichment in the bottom of the joint region for the casting with forced on the joint.

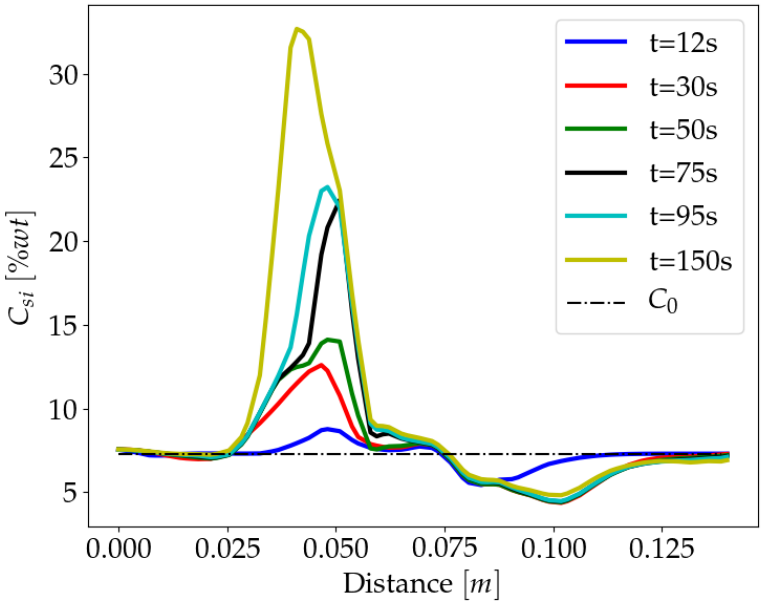

Figure 5.26: Silicon mass fraction along the centerline for instances presented in Figure 5.25.

In order to resolve the prediction instability leading to over-prediction of the silicon mass fraction, the relaxation factor for the species transport equation in Fluent was progressively decreased. A relaxation factor of 0.2 was found to eliminate the instability and the over-prediction of concentration in the vicinity of the encapsulated region. Figure 5.27 shows the silicon mass fraction on the centerline of the casting in aforementioned time instances.

Figure 5.28 shows the predicted silicon mass fraction variation for the casting with forced cooling on the joint using an relaxation factor of 0.2. It can be seen that not only is the maximum composition value now below the eutectic composition, but also the size of the enriched region has decreased.

Figure 5.29 shows the composition comparison of the simulated case using a relaxation factor and the experiment for the casting with forced cooling on the joint. It can be seen that the under-relaxation helped the model to better match the experimental result.

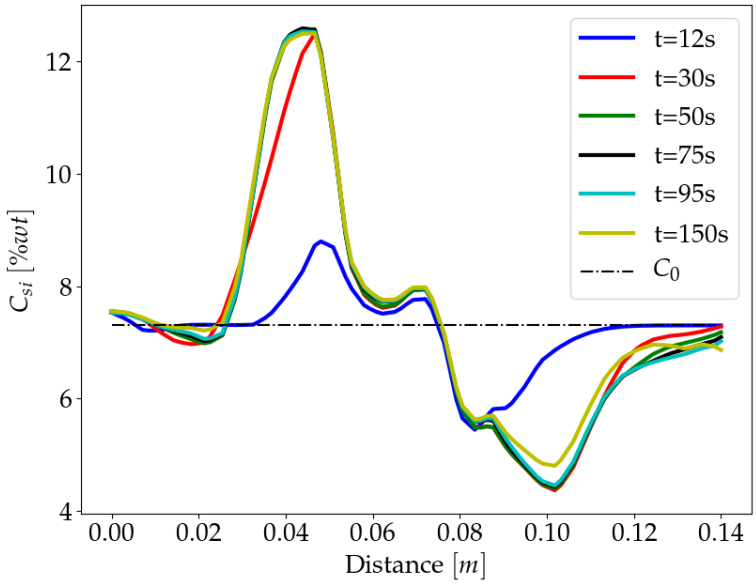

Figure 5.27: Si mass fraction along the centerline for under-relaxed model in several instances.

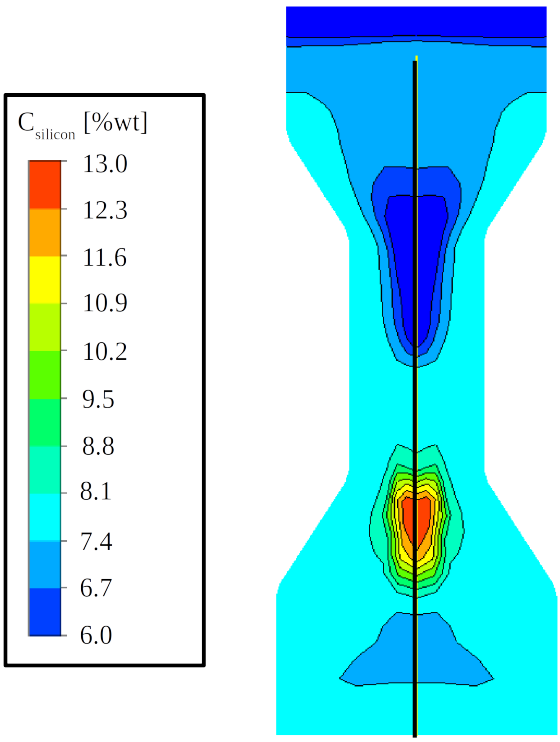

Figure 5.28: Simulated silicon segregation in the dumbbell-shaped casting with forced cooling on the joint with an under-relaxation factor.

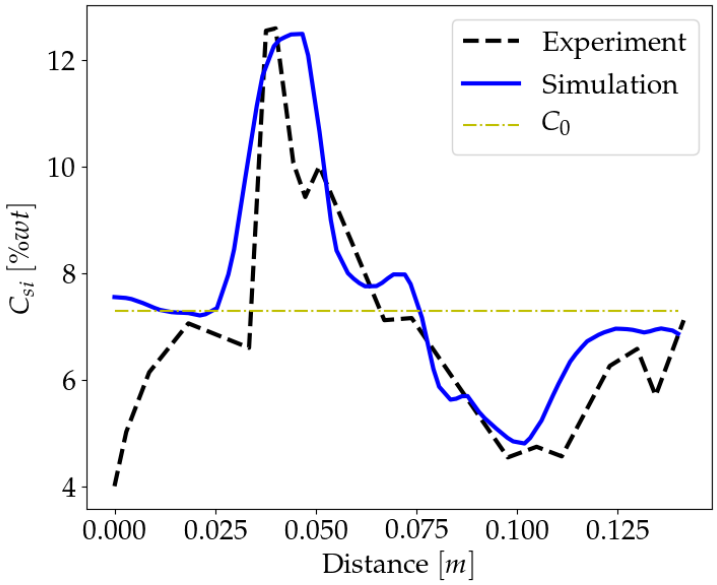

Figure 5.29: Measured and predicted silicon mass fraction along the centerline of the casting with forced cooling on the joint with an under-relaxation factor.

The same under-relaxation factor was applied to the casting with natural cooling condition. Figure 5.30 shows the silicon composition variation from the casting with natural cooling simulated using an under-relaxation factor for species equation. It can be seen that the highly enriched region visible in Figure 5.8 at the bottom of the joint section is less enriched.

Figure 5.31 shows the composition comparison of the simulated case with relaxation factor and the experiment for the casting with natural cooling. It can be seen that, similar to the previous case, the under-relaxation helped the model to better match the experimental result.

5.4 Yield strength prediction

To complete the analysis of the casting, the expression developed for flow stress in Chapter 2 has been applied to predict the yield strength variation in the each of the castings. In order for accomplishing this task, DAS predictions, as well as the Si

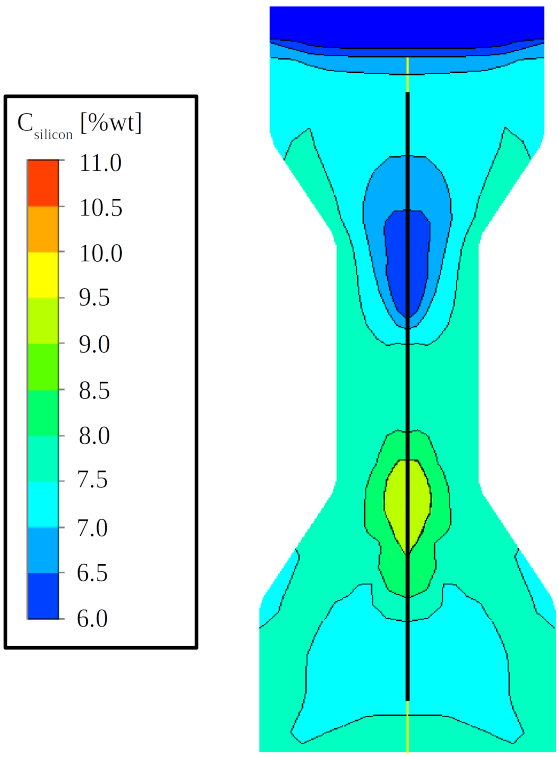

Figure 5.30: Simulated silicon segregation in the dumbbell-shaped casting with natural cooling with an under-relaxation factor.

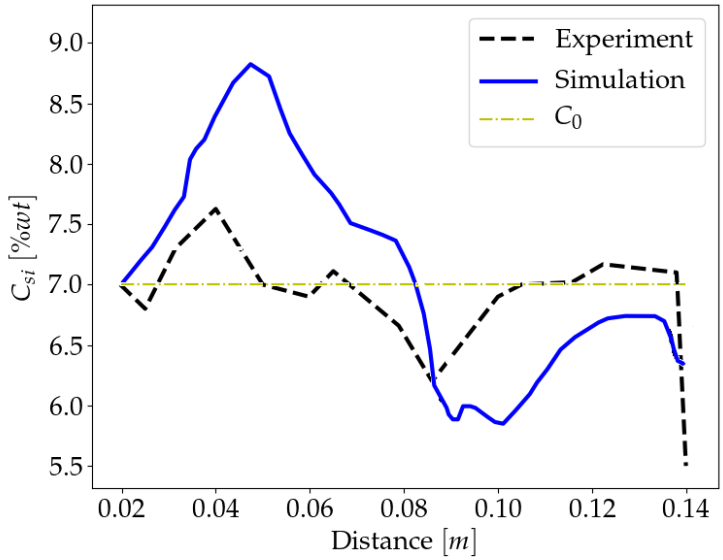

Figure 5.31: Measured and predicted silicon mass fraction along the centerline of the casting with natural cooling with an under-relaxation factor.

composition, were needed. Shabani and Mazahery studied the effects of cooling rate on microstructure of A356 [49]. Figure 5.32, borrowed from this study, shows the cooling rate vs. DAS for A356.

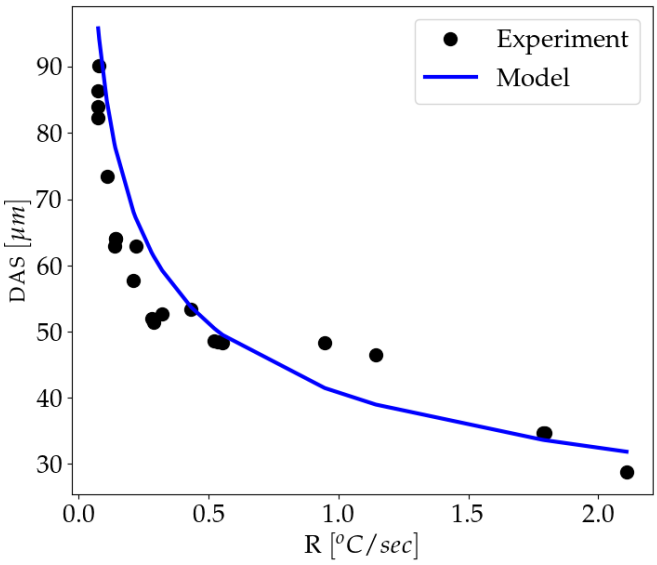

Figure 5.32: DAS vs. cooling rate for A356 [49].

Equation 5.21 shows the power law type model that was fit to this data.

$$\text{DAS} = 40.71 \times R^{-0.33} \tag{5.21}$$

The cooling rate, R, at each location in the casting is defined as the liquidus temperature, T_{liq}, minus the solidus temperature, T_{sol}, divided by the solidification time, $t_{solidification}$, (Equation 5.22).

$$R = \frac{T_{liq} - T_{sol}}{t_{solidification}} \tag{5.22}$$

Combining these equations with the modified Ludwig-Holloman expression with parameters n, K and ϵ_0 as a function of DAS, Si content and T6 state, yield strength was predicted through a post-processing operation. The results are shown in Figure

5.33. It can also be seen from the results that variation of yield strength is the highest for the case of the casting with forced cooling on the joint and the lowest for the large casting.

Figure 5.34 shows the yield strength variation in these casting if T6 heat treatment was applied. The results show a similar trend as the AC condition. However, the variation of yield strength in the T6 condition is increased by a factor of 4. This shows that in an already segregated sample, T6 heat treatment results in a much larger variation in mechanical properties.

5.5 Discussion

Macrosegregation values for the simulated cases are summarized in Table 5.2. These values were calculated based on the formula introduced in section 4.3. As can be seen, the large casting has the lowest segregation followed by the casting with natural cooling and casting with insulated joint. The casting with forced cooling on the joint has the largest degree of segregation. This trend is shown in both the measured and predicted results. It can be seen that the relative error in the values for the large casting, the casting with insulated joint and the casting with forced cooling on the joint are within 10%. However, the error for the casting with natural cooling is 40%. This difference is also evident from the Figure 5.31, where there is a visible difference in the enriched region at the bottom of the joint section.

Table 5.2: Comparison of predicted and measured macrosegregation values for each casting condition.

Casting Condition	Predicted	Measured
Casting with natural cooling	0.41	0.29
Casting with insulated joint	0.65	0.62
Casting with the forced cooling on the joint	1.04	1.17
Large casting	0.15	0.16

Comparing the encapsulation results from Figures 5.7, 5.12, 5.17 and 5.22 with

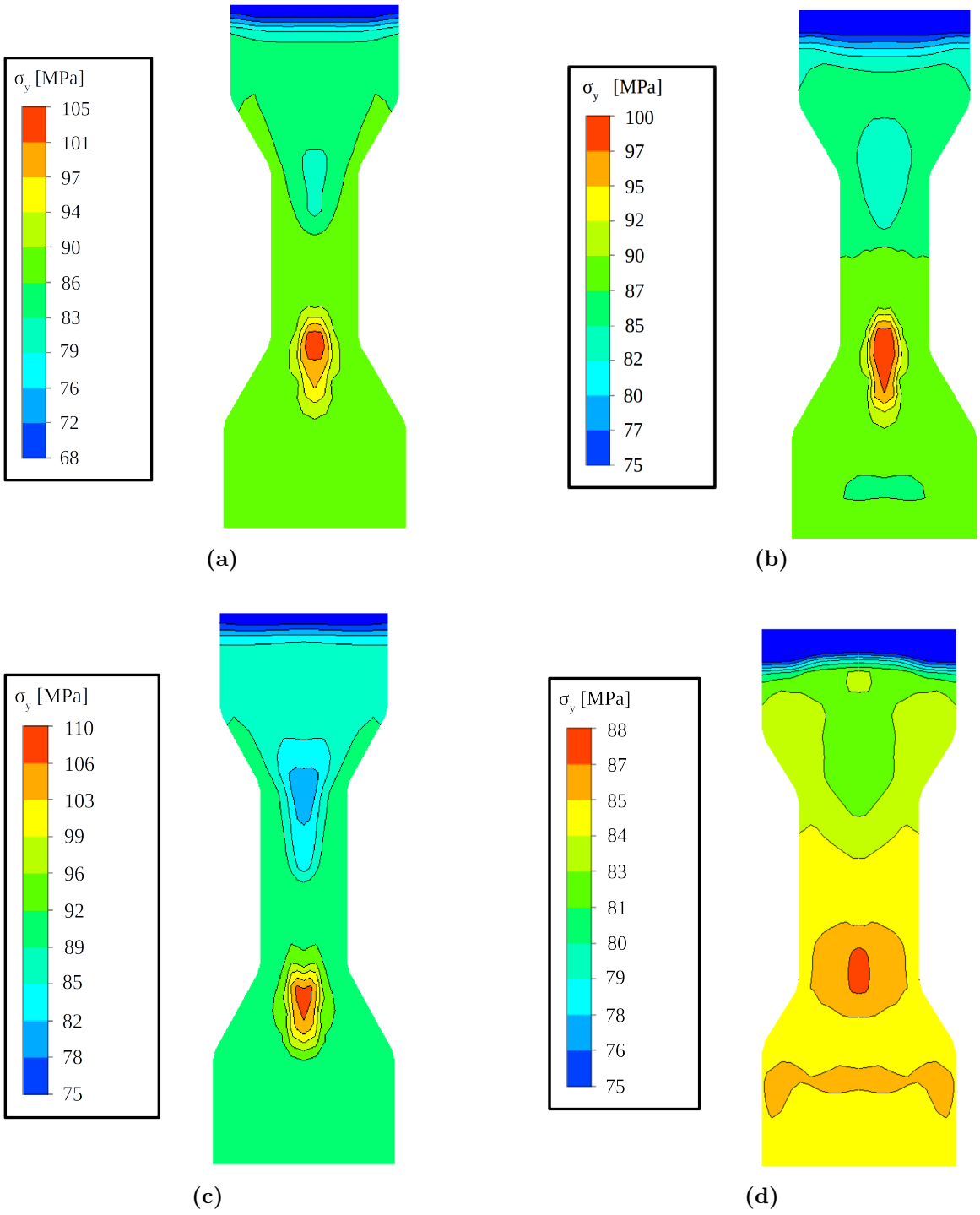

Figure 5.33: Predicted yield strength for the simulated castings AC condition. (a) for the casting with natural cooling, (b) for the casting with insulated joint, (c) for the casting with forced cooling on the joint and (d) for the large casting.

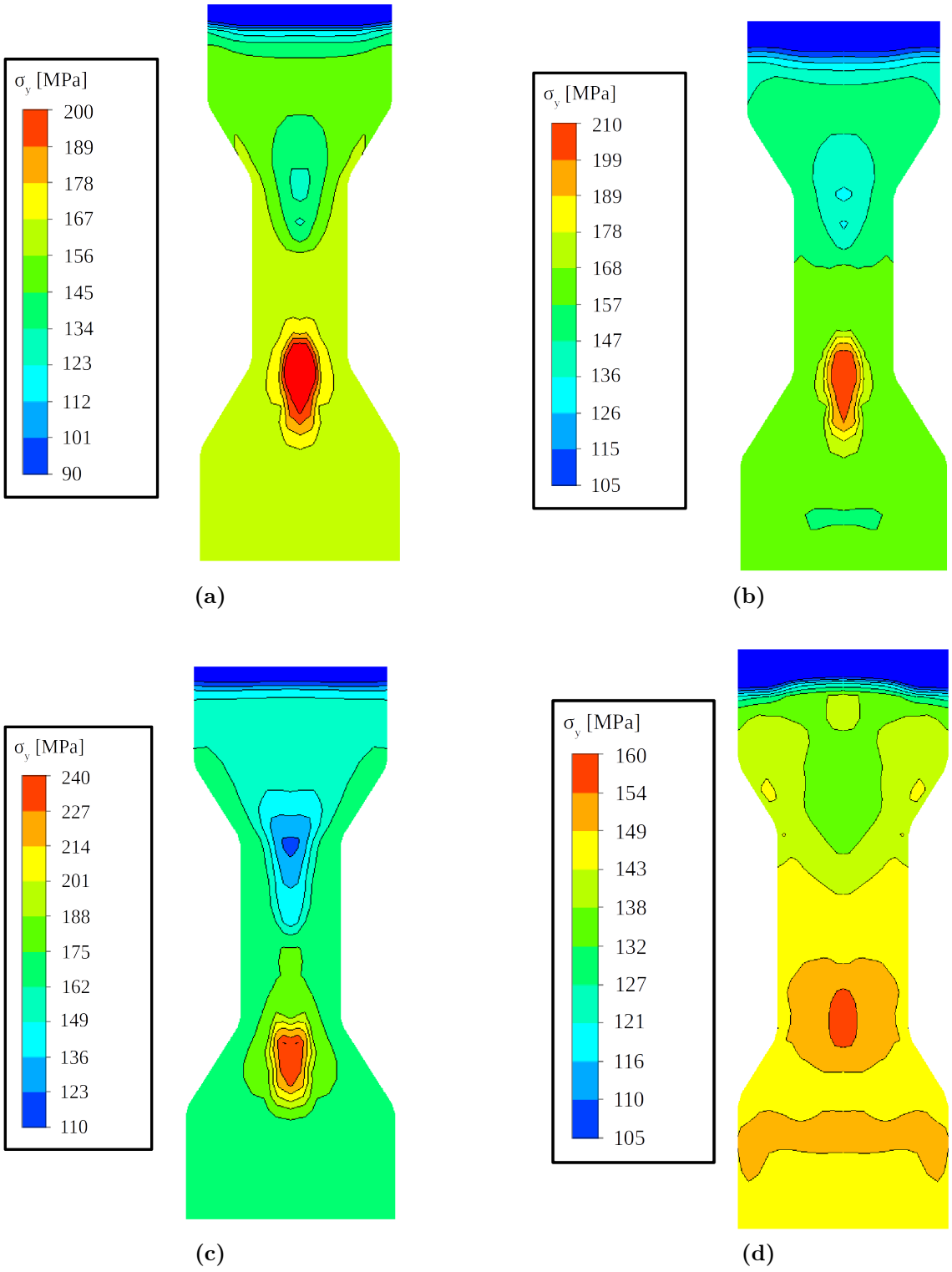

Figure 5.34: Predicted yield strength for the simulated castings T6 condition. (a) for the casting with natural cooling, (b) for the casting with insulated joint, (c) for the casting with forced cooling on the joint and (d) for the large casting.

high resolution images from Figures 4.8, 4.13, 4.18 and 4.23, respectively, shows that in all four cases the model was able to predict the shrinkage porosity at the top section of the casting. The model also correctly predicted the location of the shrinkage porosity in the joint section of the casting with forced cooling and insulation at the joint. For the case of the casting with natural cooling and the large casting, despite the model predicted encapsulation at the joint section, there is no shrinkage porosity visible in the experimental results.

The results from Figure 5.33 show that yield strength is highly dependent on the silicon composition, more so than DAS. Overall, the yield strength results suggest that macrosegregation is a defect that needs to be controlled in shape casting designs, especially where strength uniformity is important.

5.6 Summary

A complex mathematical model was developed to simulate macrosegregation in dumbbell-shaped castings. Four models were developed based on the cooling condition and size, which are discussed in detail in the previous chapter. Results can be summarized as follows:

- Temperature curves from the thermocouple location show good agreement with the experimental results. However, the top thermocouple in the simulation over-predicted temperature. This was due the opening boundary condition assigned to the top boundary in the model.

- The simulated model was able to correctly predict all the shrinkage porosities through encapsulated liquid analysis, expect for the cases of the casting with natural cooling and the large casting where it incorrectly predicted encapsulation in the bottom of the joint section.

- The model initially over-predicted the values of composition up to 40% near

the encapsulated areas (i.e. bottom of the joint section). This issue was found to be a stability related problem, which was then resolved implementing an under-relaxation factor for the species model in the simulation.

- The predicted yield strength results show that yield strength variation is more significantly influenced by the variation of silicon composition rather than DAS

Chapter 6

Summary and Conclusions

This work has studied the macrosegregation of silicon in shape cast, aluminum alloy A356. First, the effects of silicon composition, DAS and the heat treatment state on the flow stress of Al-Si-Mg alloys were investigated. In order to do this, a series of plate castings were produced from Al-Si-Mg alloys where the Si content was varied and the constitutive behaviour was characterized. The results were then used to establish an empirical expression correlating DAS, silicon content and the heat-treated state with flow stress based on a modified Hollomon equation.

In the second portion of the project, an image processing method was developed to characterize the macrosegregation occurring on cross-sections of shape castings. The method utilizes a combination of image segmentation, pixel-to-pixel analysis and tessellation techniques to construct a quantitative map of the solute distribution on large samples. The accuracy and validity of the method were assessed through a series of artificially designed micrographs.

In the third portion, a series of dumbbell-shaped castings were produced to promote and/or limit the effects macrosegregation. This was done by controlling the cooling on the joint section of a dumbbell-shaped casting mould. Four castings were produced using this technique, three small castings with natural cooling, force air cooling and insulation on the joint section and one large casting with natural cooling. The temperature history of the casting during solidification was recorded using K-type thermocouples. To determine the segregation, the castings were sectioned, polished and analyzed using the developed image processing technique.

In the final portion of the project, a numerical model was developed to simulate the macrosegregation in the aforementioned castings. Silicon species segregation during solidification was calculated assuming the Scheil approximation, and was coupled with macro-scale transport incorporating the resistance of the mushy zone and feeding flow. The model has been implemented within the commercial CFD software, FLUENT, which simultaneously solves the thermal, fluid flow fields and species segregation on the macro-scale. Finally, the constitutive behaviour expression developed in the first phase of the project was applied to predict the yield strength variation in the dumbbell-shaped castings based on the simulation data.

6.1 Conclusions

The findings of this PhD research project can be summarized as below:

- An equation was developed to characterize the constitutive behaviour of hypoeutectic Al-Si-Mg alloys. Analyzing this equation it was concluded that, apart from DAS, silicon composition variation plays a crucial role in the flow stress behaviour of the material. Furthermore, sensitivity analysis results show that the maximum yield strength occurs when DAS is low and silicon composition is high.

- A technique was developed to accurately characterize the spatial variation of macrosegregation in eutectic alloys. This method utilizes a tessellation technique to mesh the image, then calculates the area fraction of the desired phase in each element. The current method uses a continuous map of micrographs to calculate a segregation map which results in more accurate results, where previous methods used a discrete number of samples in order to do so.

- Analyzing the dumbbell-shaped castings it has been found that the segregation is the lowest in the large casting and the highest where forced cooling was

applied to the joint section.

- Analyzing the simulation results, it was observed that the numerical model over-predicted the segregation in the transition to / bottom of the joint section, where liquid encapsulation was predicted to occur. This result is caused by instability in the species model, and was resolved by applying an under-relaxation factor. Similar to the experimental results, it was predicted that segregation in the large casting is the lowest.

6.2 Future work

The current study considers a wide range of issues related to macrosegregation in A356 aluminum alloy shape castings. The following items have been identified to extend the current work:

- In describing constitutive behaviour, the effects of temperature and strain rate should be included. This is necessary for developing a comprehensive constitutive equation and to allow the deformation of a casting that has experienced macrosegregation during solidification to be predicted.

- The most challenging section for the image analysis technique was developing a segmentation method to segment the micrographs into desired phases. An improvement for this would be to include a more sophisticated segmentation technique. This can be done by training an object detection algorithm to classify the phases. This will allow the technique to be used for wider range of alloys to help improve the performance of the alloy.

- In order to characterize macrosegregation more accurately, castings with a wide variety of sizes and cooling rates should be used. This will help to build a more comprehensive database of different solidification conditions and corresponding

macrosegregation patterns, which in turn allows to improve the accuracy of the method.

- In the current simulation, the top opening boundary condition does not accurately represent the conditions present in the castings. In order to improve this a user-defined boundary condition should be developed in Fluent that allows the implementation of HTCs onto the opening boundary condition.

- A series of macro-hardness tests could be implemented to verify the yield strength variation results from the simulation. This would further verify both the flow stress model and the developed numerical model.

Bibliography

[1] B. Zhang, D. M. Maijer, and S. L. Cockcroft. Development of a 3-D thermal model of the low-pressure die-cast (LPDC) process of A356 aluminum alloy wheels. *Materials Science and Engineering A*, 464(1-2):295–305, 2007. *(Cited on pages 1 and 18.)*

[2] S.S.M. Nazirudeen and B. Chokkalingam. Analysis of Casting Defect Through Defect Diagnosis Study Approach. *Journal of Engineering Annals of Faculty of Engineering Hunedoara*, 2:209–212, 2009. *(Cited on page 1.)*

[3] E. Gariboldi, F. Bonollo, and M. Rosso. Proposal of a classification of defects of high-pressure diecast products. *Metallurgia Italiana*, 99(6):39–46, 2007. *(Cited on page 1.)*

[4] B. Zhang, S. Cockcroft, D. Maijer, J. Zhu, and A. Phillion. Casting defects in low-pressure die-cast aluminum alloy wheels. *JOM*, 57(11):36–43, nov 2005. *(Cited on pages 1 and 2.)*

[5] R Monroe. Porosity in castings. *AFS Trans*, 5(04):10, 2005. *(Cited on page 2.)*

[6] D. M. Stefanescu. Computer simulation of shrinkage related defects in metal castings âĂŞ a review. *International Journal of Cast Metals Research*, 18(3):129–143, 2005. *(Cited on page 2.)*

[7] A. Reis, Y. Houbaert, Z. Xu, R. Van Tol, A. Santos, J. Duarte, and A. Magalhaes. Modeling of shrinkage defects during solidification of long and short freezing materials. *J. Mater. Process. Technol*, 202:428–434, 2008. *(Cited on page 2.)*

[8] N. Barman and P. Dutta. Studies on macrosegregation and double diffusive convection during directional solidification of binary mixture. *Materials Science and Technology*, 24(10):1230–1237, 2008. *(Cited on page 2.)*

[9] S. Chakraborty and P. Dutta. Three-dimensional double-diffusive convection and macrosegregation during non-equilibrium solidification of binary mixtures. *International Journal of Heat and Mass Transfer*, 46(12):2115–2134, 2003. *(Cited on pages 2 and 10.)*

[10] W. Kurz and D. Fisher. *Fundamentals of Solidifcation*. Uetikon-Zuerich: Trans Tech Publications, 4th revise edition, 1998. *(Cited on pages 2, 17, and 18.)*

[11] J. Dantzig and M. Rappaz. *Solidification*. CRC Press, 1st edition, 2009. *(Cited on pages 2, 4, 5, 17, 18, 47, and 98.)*

[12] C. Beckermann. Macrosegregation. In *Encyclopedia of Materials: Science and Technology*, pages 4733–4738. 2001. *(Cited on page 3.)*

[13] V. Coangelo and F. Heiser. *Analysis of Mettalurgical Failures*. John Wiley and Sons, 1987. *(Cited on page 4.)*

[14] R. Mehrabian. *Macrosegregation*. Massachusetts Institude of Technology, 1969. *(Cited on page 5.)*

[15] R. Mehrabian, M. Keane, and M. C. Flemings. Interdendritic fluid flow and macrosegregation; influence of gravity. *Metallurgical and Materials Transactions*, 1(5):1209–1220, 1970. *(Cited on pages 6 and 9.)*

[16] R. Mehrabian and M. C. Flemings. Macrosegregation in ternary alloys. *Metallurgical and Materials Transactions B*, 1(2):455–464, 1970. *(Cited on page 6.)*

[17] N. Streat and F. Weinberg. Macrosegregation during solidification resulting from density differences in the liquid. *Metallurgical Transactions*, 5(December):2539–2548, 1974. *(Cited on page 6.)*

[18] W. J. Boettinger, F. S. Biancaniello, and S. R. Coriell. Solutal convection induced macrosegregation and the dendrite to composite transition in off-eutectic alloys. *Metallurgical Transactions A*, 12(2):321–327, 1981. *(Cited on page 6.)*

[19] L. Wang, V. Laxmanan, and J.F. Wallace. Unidirectionally Solidified Lead-Tin Alloy. *Metallurgical Transactions A*, 19(November), 1988. *(Cited on page 6.)*

[20] P.J. Prescott. *Convective transport phenomena during solidification of binary metal alloys and the effects of magnetic fields*. PhD thesis, Purdue University, 1992. *(Cited on page 7.)*

[21] M.J.M. Krane. *Transport Phenomena During The Solidification of Binary and Ternary Metal Alloys*. PhD thesis, Purdue University, 1996. *(Cited on page 7.)*

[22] J. Leon-Torres, P. Curreri, D. M. Stefanescu, and S. Sen. Gravitational Acceleration Effects on Macrosegregation: Experiment and Computational Modeling. In *TMS Annual Meeting*, 1999. *(Cited on page 7.)*

[23] I. L. Ferreira, A. Garcia, and B. Nestler. On macrosegregation in ternary Al-Cu-Si alloys: Numerical and experimental analysis. *Scripta Materialia*, 50(4):407–411, 2004. *(Cited on page 8.)*

[24] S.N. Ojha and S.N. Tewari. Mushy Zone Characteristics and Macrosegregation During Directional Solidification. *Trans. Indian Inst. Met.*, 57(5):475–483, 2004. *(Cited on page 8.)*

[25] M. Flemings and G. Nereo. Mecrosegregation: Part 1. *Trans. Metall. Soc. AIME*, 239:1449–1461, 1967. *(Cited on page 9.)*

[26] S. D. Ridder, S. Kou, and R. Mehrabian. Effect of fluid flow on macrosegregation in axi-symmetric ingots. *Metallurgical Transactions B*, 12(3):435–447, 1981. *(Cited on pages 9 and 10.)*

[27] W. Bennon and F.P. Incropera. A continuum model for momentum, heat and species transport binary solid-liquid phase chenge systems\rI. Model formulation. *International Journal of Heat and Mass Transfer*, 30(10):2161–2170, 1987. *(Cited on page 9.)*

[28] W. Bennon and F.P. Incropera. A continuum model for momentum, heat and species transport binary solid-liquid phase chenge systems\rI. Model formulation. *International Journal of Heat and Mass Transfer*, 30(10):2161–2170, 1987. *(Cited on page 9.)*

[29] V.R. Voller, A.D. Brent, and C. Prakash. The Modeling of Heat, Mass and Solute Transport in Solidification systems. *International Journal of Heat and Mass Transfer*, 32(9):1719–1731, 1989. *(Cited on pages 10 and 11.)*

[30] J. Ni and C. Beckermann. A volume-averaged two-phase model for transport phenomena during solidification. *Metallurgical Transactions B*, 22(3):349–361, 1991. *(Cited on page 11.)*

[31] J. Ni and F.P. Incropera. Extension of the continuum model for transport phenomena occurring during metal alloy solidification-I. The conservation equations. *International Journal of Heat and Mass Transfer*, 38(7):1271–1284, 1995. *(Cited on page 11.)*

[32] J. Ni and F.P. Incropera. Extension of the continuum model for transport phelnomena occurring during metal alloy Microscopic considerations. *International Journal of Heat and Mass Transfer*, 38(7):1285–1296, 1995. *(Cited on page 11.)*

[33] C.J. Vreeman, M.J.M. Krane, and F.P. Incropera. The Effect of Free-Floating Dendrites and Convection on Macrosegregation in Direct Chill Cast Aluminum Alloys Part II: Predictions for Al-Cu and Al-Mg Alloys. *International Journal of Heat and Mass Transfer*, 43:687–704, 2000. *(Cited on page 11.)*

[34] C.J. Vreeman, M.J.M. Krane, and F.P. Incropera. The effect of free-floating dendrites and convection on macrosegragation in direct chill cast aluminum alloys Part I: Model development. *International Journal of Heat and Mass Transfer*, 43(5):677–686, 2000. *(Cited on pages 11 and 13.)*

[35] M.J.M. Krane and F.P. Incropera. Solidification of ternary metal alloysâĂŤII. Predictions of convective phenomena and solidification behavior in Pb-Sb-Sn alloys. *International Journal of Heat and Mass Transfer*, 40(16):3837–3847, 1997. *(Cited on page 12.)*

[36] M.J.M. Krane, F.P. Incropera, and D.R. Gaskell. Solidification of ternary metal alloysâĂŤI. Model development. *International Journal of Heat and Mass Transfer*, 40(16):3827–3835, 1997. *(Cited on page 12.)*

[37] M. Rappaz and C. A. Gandin. Probabilistic modelling of microstructure formation in solidification processes. *Acta Metallurgica Et Materialia*, 41(2):345–360, 1993. *(Cited on page 12.)*

[38] C. A. Gandin and M. Rappaz. A coupled finite element-cellular automaton model for the prediction of dendritic grain structures in solidification processes. *Acta Metallurgica Et Materialia*, 42(7):2233–2246, 1994. *(Cited on pages 12 and 14.)*

[39] P. D. Lee, A. Chirazi, R. C. Atwood, and W. Wang. Multiscale modelling of solidification microstructures, including microsegregation and microporosity, in an Al-Si-Cu alloy. *Materials Science and Engineering A*, 365(1-2):57–65, 2004. *(Cited on page 12.)*

[40] G. Guillemot, C. Gandin, and H. Combeau. Modeling of Macrosegregation and Solidification Grain Structures with a Coupled Cellular Automaton-Finite Element Model. *ISIJ International*, 46(6):880–895, 2006. *(Cited on page 12.)*

[41] H. Zhang, K. Nakajima, E. Wang, and J. He. Modeling of macrosegregation and solidification microstructure for Al-Si alloy under unidirectional solidification by a coupled cellular automaton âĂŞ finite volume model. *IOP Conference Series: Materials Science and Engineering*, 33:012093, 2012. *(Cited on pages 12 and 14.)*

[42] E. J. Pickering. Macrosegregation in Steel Ingots : The Applicability of Modelling and Characterisation Techniques. *ISIJ International*, 53(6):935–949, 2013. *(Cited on page 15.)*

[43] A. Tewari, M. Dighe, and A.M. Gokhale. Quantitative Characterization of Spatial Arrangement of Micropores in Cast Microstructures. *Materials Characterization*, 40(2):119–132, 1998. *(Cited on page 15.)*

[44] D.G.L. Prakash and D. Regener. Quantitative characterization of Mg17Al12 phase and grain size in HPDC AZ91 magnesium alloy. *Journal of Alloys and Compounds*, 461(1-2):139–146, 2008. *(Cited on page 15.)*

[45] D. G. L. Prakash, B. Prasanna, and D. Regener. Computational microstructure analyzing technique for quantitative characterization of shrinkage and gas pores in pressure die cast AZ91 magnesium alloys. *Computational Materials Science*, 32(3-4):480–488, 2005. *(Cited on pages 15 and 45.)*

[46] G. Straffelini and A. Molinari. Image Analysis Study of Macrosegregation in a High-Carbon Continuously Cast Steel. *Materials Characterization*, 38(97):203–210, 1997. *(Cited on page 15.)*

[47] M. J. Roy. *Rotary Forming of Cast Aluminum*. PhD thesis, University of British Columbia, 2013. *(Cited on pages 15, 16, 17, 19, 20, and 45.)*

[48] J. P. Macht, D. M. Maijer, and A. B. Phillion. A Combined NumericalâĂŞExperimental Approach to Quantify the Thermal Contraction of A356 During Solidification. *Metallurgical and Materials Transactions A*, 48(7):1–7, 2017. *(Cited on page 18.)*

[49] M. Shabani and A. Mazahery. Prediction of mechanical properties of cast A356 alloy as a function of microstructure and cooling rate. *Archives of Metallurgy and Materials*, 56(3):671–675, 2011. *(Cited on pages 20 and 130.)*

[50] G. Ran, J. Zhou, and Q. Wang. The effect of hot isostatic pressing on the microstructure and tensile properties of an unmodified A356-T6 cast aluminum alloy. *Journal of Alloys and Compounds*, 421(1-2):80–86, 2006. *(Cited on page 20.)*

[51] Q. Wang. Microstructural Effects on the Tensile and Fracture Behavior of Aluminum Casting Alloys A356 / 357. *Metallurgical and Materials Transactions A*, 34(December):2887–2899, 2003. *(Cited on page 20.)*

[52] J. Boileau, W. Zindel, and J. Allison. The effect of solidification time on the mechanical properties in a cast A356-T6 aluminum alloy. *Society of Automotive Engineers, Inc.,*, pages 61–72, feb 1997. *(Cited on page 20.)*

[53] L. Ceschini, A. Morri, A. Morri, A. Gamberini, and S. Messieri. Correlation between ultimate tensile strength and solidification microstructure for the sand cast A357 aluminium alloy. *Materials and Design*, 30(10):4525–4531, 2009. *(Cited on page 20.)*

[54] E. Hall. *Yield Point Phenomena in Metals and Alloys*. Springer, 1970. *(Cited on pages 20 and 35.)*

[55] J. Campbell. Properties of castings. In *Complete Casting Handbook*, pages 499–597. Elsevier Ltd, 2011. *(Cited on page 21.)*

[56] W. Osorio, P. Goulart, G. Santos, C. Neto, and A. Garcia. Effect of dendritic arm spacing on mechanical properties and corrosion resistance of Al 9 wt pct Si and Zn 27 wt pct Al alloys. *Metallurgical and Materials Transactions A: Physical Metallurgy and Materials Science*, 37(8):2525–2538, 2006. *(Cited on page 21.)*

[57] P. Goulart, J. Spinelli, W. Osório, and A. Garcia. Mechanical properties as a function of microstructure and solidification thermal variables of Al-Si castings. *Materials Science and Engineering A*, 421:245–253, 2006. *(Cited on page 21.)*

[58] K. Cruz, E. Meza, F. Fernandes, J. Quaresma, L. Casteletti, and A. Garcia. Dendritic arm spacing affecting mechanical properties and wear behavior of

Al-Sn and Al-Si alloys directionally solidified under unsteady-state conditions. *Metallurgical and Materials Transactions A: Physical Metallurgy and Materials Science*, 41(4):972–984, 2010. *(Cited on page 21.)*

[59] H. Elzanaty. Effect of different Si content on the mechanical properties in Al-based alloy. *International Journal of Research in Engineering & Technology*, 2(7):2321–8843, 2014. *(Cited on page 21.)*

[60] M. Kalhapure and P. Dighe. Impact of Silicon Content on Mechanical Properties of Aluminum Alloys. *International Journal of Science and Research (IJSR)*, 14(6):2319–7064, 2013. *(Cited on page 21.)*

[61] J. Barresi, M. Kerr, H. Wang, and J. Couper. Effect of Magnesium , Iron and Cooling Rate on Mechanical Properties of Al-7Si-Mg Foundry Alloys. *AFS Transactions*, pages 563–570, 2000. *(Cited on page 22.)*

[62] H. Moller, G. Govender, and W . Stumpf. Investigation of the T4 and T6 Heat Treatment Cycles of Semi-Solid Processed Aluminium Alloy A356. *The Open Materials Science Journal*, 2(1):11–18, 2010. *(Cited on page 22.)*

[63] M. Roy, D. Maijer, and L. Dancoine. Constitutive behavior of as-cast A356. *Materials Science and Engineering A*, 548:195–205, 2012. *(Cited on page 22.)*

[64] K G Samuel. Limitations of Hollomon and Ludwigson stressâĂŞstrain relations in assessing the strain hardening parameters. *J. Phys. D: Appl. Phys. J. Phys. D: Appl. Phys*, 39(39):203–203, 2006. *(Cited on page 22.)*

[65] N. Haghdadi, A. Zarei-Hanzaki, A. R. Khalesian, and H. R. Abedi. Artificial neural network modeling to predict the hot deformation behavior of an A356 aluminum alloy. *Materials and Design*, 49:386–391, 2013. *(Cited on page 22.)*

[66] G. E. Dieter. *Mechanical Metallurgy.* mcGraw-Hill, 1988. *(Cited on pages 29 and 40.)*

[67] C. A. Schneider, W. S. Rasband, and K. W. Eliceiri. NIH Image to ImageJ: 25 years of image analysistle. *Nature methods*, 9(7):671–675, 2012. *(Cited on page 31.)*

[68] C. C. Wigant and R. I. Stephens. Low Cycle Fatigue of A356-T6 Cast Aluminum Alloy. *SAE Technical Paper*, 1987. *(Cited on page 32.)*

[69] C. Lee. Effects of microporosity on tensile properties of A356 aluminum alloy. *Materials Science and Engineering A*, (464):249–254, 2007. *(Cited on page 34.)*

[70] T Altan. *Metal Forming: Fundamentals and Applications.* American Society for Metals, Metals Park, Ohio, 1985. *(Cited on page 39.)*

[71] P.G. Ho. *Image Segmentation.* InTech, apr 2011. *(Cited on page 44.)*

[72] N. Otsu. A threshold selection method from gray-level histograms. *IEEE Transactions*, 9(1):62–66, 1979. *(Cited on page 45.)*

[73] P.O. Persson. *Mesh Generation for Implicit Geometries*. PhD thesis, MIT, 2005. *(Cited on pages 46 and 56.)*

[74] David Brandon and Wayne D Kaplan. *Microstructural Characterization of Materials - 2nd Edition*. John Wiley and Sons, 2nd edition, 2008. *(Cited on pages 47 and 151.)*

[75] J.B. MacQueen. Some Methods for classification and Analysis of Multivariate Observations. In *Proceedings of 5-th Berkeley Symposium on Mathematical Statistics and Probability*, pages 281–297, 1967. *(Cited on page 52.)*

[76] B.G. Lindsay. Mixture Models: Theory, Geometry, and Applications. In *NSF-CBMS Regional Conference Series in Probability and Statistics*, 1995. *(Cited on page 52.)*

[77] Ehsan Khajeh. *Permeability of Hypoeutectic Aluminum Alloys*. PhD thesis, University of British Columbia, 2011. *(Cited on pages 52 and 53.)*

[78] V. R. Voller and C. Swaminathan. General Source-Based Method For Solidification Phase Change. *Numerical Heat Transfer*, 19:175–189, 1991. *(Cited on page 100.)*

[79] M. Trovant and S. Argylopoulos. Finding boundary conditions: a coupling strategy goes the modeling of metal casting process: part I. Experimental study and correlation development. *Metallurgical and Materials Transactions B*, 31(February):75, 2000. *(Cited on page 103.)*

[80] S.W. Churchill and H.H.S. Chu. Correlating equations for laminar and turbulent free convection from a vertical plate. *International Journal of Heat and Mass Transfer*, 18(11):1323–1329, 1975. *(Cited on page 104.)*

[81] K. C. Mills. *Recommended values of thermophysical properties for selected commercial alloys*. Woodhead Publishing Limited, 2002. *(Cited on page 107.)*

[82] S. Thompson, S. L. Cockcroft, and M. Wells. Advanced light metals casting development: solidification of aluminium alloy A356. *Materials Science and Technology*, 20(February):194–200, 2004. *(Cited on page 107.)*

[83] M. P. De Cicco, L.S. Turng, X. Li, and J. H. Perepezko. Nucleation catalysis in aluminum alloy A356 using nanoscale inoculants. *Metallurgical and Materials Transactions A: Physical Metallurgy and Materials Science*, 42(8):2323–2330, 2011. *(Cited on page 107.)*

[84] J Ferziger and M Petric. *Computarional Methods for Fluid Dynamics*. Springer, 3rd edition, 2002. *(Cited on page 124.)*

[85] E. Schmidt and K. Wenner. *Heat transfer over the circumference of the heated cylinder in transverse flow.* Tech. Rep. NACA-TM-1050. National Advisory Committee for Aeronautics. *(Cited on pages 69 and 70.)*

Appendices

Appendix A: Term Sensitivity of the Flow Stress Model

A sensitivity analysis has been conducted to assess the relative significance of each term in equation 2.1 for n, K and ϵ_0. Relative significance in this case is defined as the percentage of contribution of each term in the equation and is calculated by dividing the magnitude of each term by the sum of magnitudes of all the terms. The five terms which were studied are; a, $b \times \mathbf{T6}$, $(\mathbf{T6}+1) \times c \times C_{Si}$, $(\mathbf{T6}+1) \times d \times \text{DAS}^{-1/2}$ and $(\mathbf{T6}+1) \times e \times C_{Si} \times \text{DAS}^{-1/2}$. These terms are referred to with roman numerals I to V, respectively. The analysis was conducted over a combination of cases with low and high DAS values (i.e. 20 and 50μm) and low and high Si contents (i.e. 4 and 10 wt%) in T6 and AC conditions. The results are shown in Tables 6.1 to 6.3.

Table 6.1: Relative significance of terms I to V on parameter n in various conditions. Note that the values are in percentages.

n (AC)	low DAS					high DAS				
	I	II	III	IV	V	I	II	III	IV	V
low C_{Si}	53.8	0.0	7.6	29.7	9.0	68.4	0.0	9.6	16.9	5.1
high C_{Si}	29.5	0.0	24.8	16.2	29.5	39.4	0.0	33.2	9.7	17.6

n (T6)	low DAS					high DAS				
	I	II	III	IV	V	I	II	III	IV	V
low C_{Si}	25.4	31.0	7.1	28.0	8.5	31.8	38.8	8.9	15.7	4.7
high C_{Si}	14.3	17.4	24.1	15.7	28.5	18.9	23.1	31.8	9.3	16.9

Table 6.2: Relative significance of terms I to V on parameter K in various conditions. Note that the values are in percentages.

K (AC)	low DAS					high DAS				
	I	II	III	IV	V	I	II	III	IV	V
low C_{Si}	10.4	0.0	13.3	63.6	12.7	18.0	0.0	23.0	49.2	9.8
high C_{Si}	4.5	0.0	34.7	27.7	33.2	6.8	0.0	52.2	18.6	22.4

K (T6)	low DAS					high DAS				
	I	II	III	IV	V	I	II	III	IV	V
low C_{Si}	4.0	26.9	10.2	49.0	9.8	5.9	39.9	15.2	32.5	6.5
high C_{Si}	2.0	13.4	30.7	24.5	29.4	2.8	19.1	43.7	15.6	18.7

Table 6.3: Relative significance of terms I to V on parameter ϵ_0 in various conditions. Note that the values are in percentages.

ϵ_0 (AC)	low DAS					high DAS				
	I	II	III	IV	V	I	II	III	IV	V
low C_{Si}	53.4	0.0	9.1	31.8	5.7	67.3	0.0	11.5	18.0	3.2
high C_{Si}	30.7	0.0	31.5	18.3	19.5	38.8	0.0	39.8	10.3	11.0

ϵ_0 (T6)	low DAS					high DAS				
	I	II	III	IV	V	I	II	III	IV	V
low C_{Si}	35.9	1.4	12.3	42.8	7.6	49.8	1.9	17.0	26.5	4.7
high C_{Si}	18.0	0.7	36.9	21.5	22.9	23.9	0.9	48.9	12.7	13.6

It can be seen from the sensitivity results that the parameters are more sensitive to changes in Si content rather than DAS. This suggests a similar behaviour for the flow stress. Furthermore, applying the T6 heat treatment to the alloy seems to have a small effect on the contributions of terms III and V – the terms dependent on Si content. This is expected since applying a T6 heat treatment does not change the silicon content and its contribution to the flow stress. Furthermore, applying a T6 heat treatment activates term II, which is inactive in the as-cast condition. This results in a contribution from term II and consequently a decrease in relative significance of the other terms. Overall, the contribution of all the parameters are significant in the equation.

Appendix B: Area Fraction to Volume Fraction Conversion

From stereological point of view there are only a few bulk microstructural parameters that can be accessed from analyzing a 2D surface, where volume fraction is one of them [74]. According to Kaplan [74], volume fraction is equal to area fraction if the cross-sectional plane is randomly positioned.

In order to test this method, a series of synthetic microstructures were generated using Blender[1]. All the synthetic microstructures were confined to cube with a similar volume, and the microstructure itself was modelled using randomly placed ellipsoids with random sizes and aspect ratios. Figure 6.1 shows a sample synthetic microstructure generated using this method.

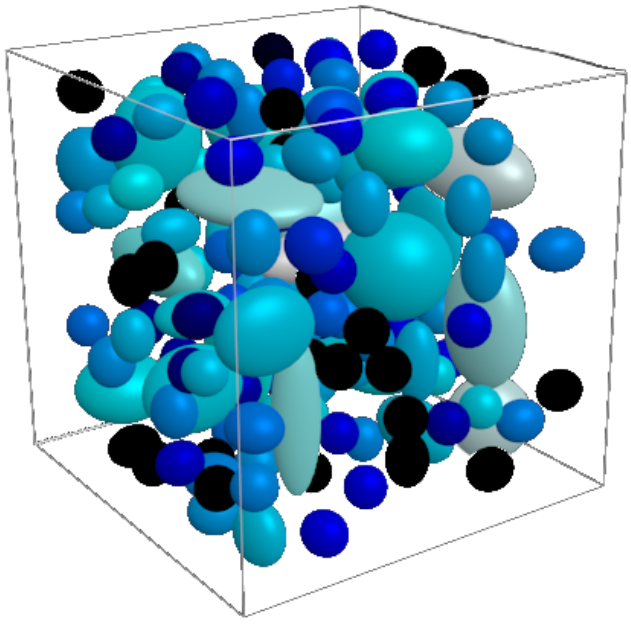

Figure 6.1: Sample synthetic microstructure generated using Blender.

[1]Blender 2.69 - a 3D modelling and rendering package

A randomly positioned plane was then used to cut the sample and acquire the resulting cross-sectional projection. Figure 6.2 shows a sample cross-sectional image acquired from a synthetic microstructure.

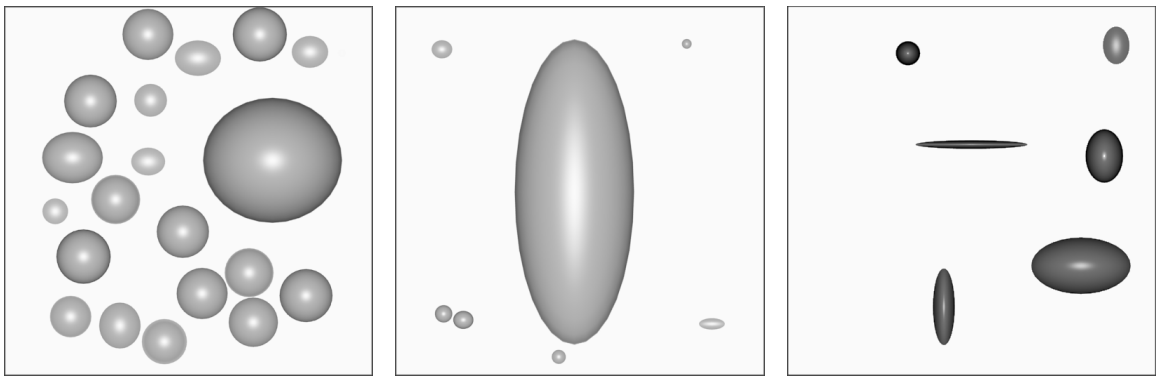

(a) (b) (c)

Figure 6.2: Sample cross-sectional images acquired from synthetic microstructures.

Volume fraction data, calculated within Blender, and the cross-section images were then written into files. This was carried out for five hundred iterations. A Python code was then used to calculate the area fraction of the ellipsoid cross-sections and compare it to the volume fraction calculated from Blender.

Figure 6.3 shows the error distribution plot for the area fraction to volume fraction conversion, attained from the ellipsoid analysis. The initial observation suggests that the data is normally distributed. Therefore, a Gaussian distribution was fitted onto the error data.

The fitted Gaussian distribution has a mean of 0.00 and a standard deviation of 0.11, which suggests that the majority of the data lies within 10% error. In other words, area fraction value, calculated using a random cross-sectional plane, is more likely to be within 10% error. This suggests that area fraction and volume fraction can be used interchangeably with a reasonable error margin. This concept combined with the volume fraction to mass fraction conversion is used in various sections to convert area fraction to mass fraction.

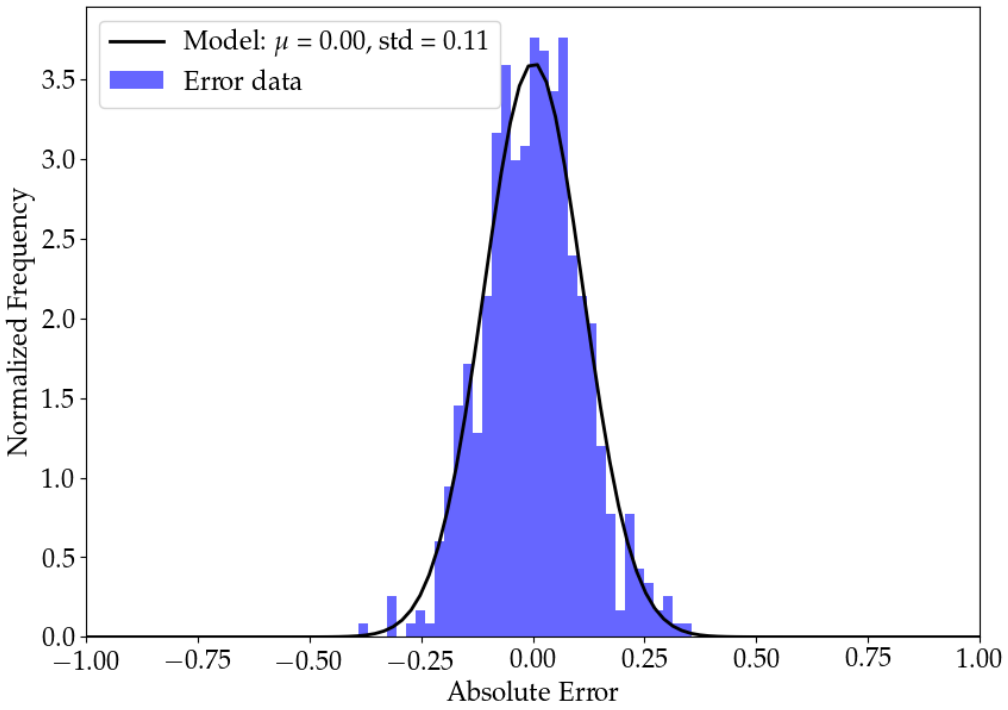

Figure 6.3: Error distribution plot for area fraction to volume fraction conversion analysis.